Tomographic Retrievals of Stratospheric Ozone with the Ozone Mapping and Profiler Suite Limb Profiler

A Thesis Submitted to the
College of Graduate and Postdoctoral Studies
in Partial Fulfillment of the Requirements
for the degree of Doctor of Philosophy
in the Department of Physics and Engineering Physics
University of Saskatchewan
Saskatoon

By
Daniel Zawada

Permission to Use

In presenting this thesis in partial fulfilment of the requirements for a Postgraduate degree from the University of Saskatchewan, I agree that the Libraries of this University may make it freely available for inspection. I further agree that permission for copying of this thesis in any manner, in whole or in part, for scholarly purposes may be granted by the professor or professors who supervised my thesis work or, in their absence, by the Head of the Department or the Dean of the College in which my thesis work was done. It is understood that any copying or publication or use of this thesis or parts thereof for financial gain shall not be allowed without my written permission. It is also understood that due recognition shall be given to me and to the University of Saskatchewan in any scholarly use which may be made of any material in my thesis.

Requests for permission to copy or to make other use of material in this thesis in whole or part should be addressed to:

Head of the Department of Physics and Engineering Physics
116 Science Place
University of Saskatchewan
Saskatoon, Saskatchewan
Canada
S7N 5E2

Or,

Dean
College of Graduate and Postdoctoral Studies
University of Saskatchewan
116 Thorvaldson Building, 110 Science Place
Saskatoon, Saskatchewan S7N 5C9
Canada

Abstract

Measurements of limb scattered sunlight have been successfully used to obtain vertically resolved profiles of trace species in the stratosphere and upper troposphere for decades. A common simplifying assumption made in inverting limb scatter measurements is that the atmosphere is horizontally homogenous, which may not be valid in regions of large horizontal gradients such as on the edge of the polar vortex. Here we introduce a new radiative transfer model, SASKTRAN-HR, which can solve the radiative transfer equation in two- and three-dimensional atmospheres. A newly developed technique to approximate the Jacobian matrix for two-dimensional atmospheres is also presented.

SASKTRAN-HR is then used to perform the first tomographic retrieval of ozone from limb scattered sunlight using measurements from the Ozone Mapping and Profiler Suite (OMPS-LP). The tomographic retrieval is shown to remove biases which are present in traditional one-dimensional retrievals that assume horizontal homogeneity. The two-dimensional retrieval agrees favorably with measurements from the Microwave Limb Sounder to within approximately 5%. The retrieval was applied to the full six years of measurements from OMPS-LP to create a publicly available dataset. The dataset has been included in several merged stratospheric ozone composites which are used in the World Meteorogical Association's 2018 ozone assessment.

Acknowledgements

This work was financially supported by the Canadian Space Agency, the National Sciences and Engineering Research Council, the University of Saskatchewan and the Institude of Space and Atmospheric Studies, and the National Aeronautics and Space Administration.

I would like to thank my advisors, Dr. Doug Degenstein and Dr. Adam Bourassa who allowed me freedom in exploring my own ideas but were also always available for guidance. Everyone in Room 312 has contributed to this project in one way another, whether technically or simply making my time here more enjoyable. In particular my thanks go to Dr. Nick Lloyd for guidance on everything SASKTRAN; Seth Dueck for help in validating the HR model; Landon Rieger for aid in working with OMPS-LP data; and Chris Roth for help in processing the retrieval.

Lastly, I would like to thank my family, in particular Stephanie, who supported me through this process.

Contents

List of Tables

List of Figures

List of Abbreviations

ACE	Atmospheric Chemistry Experiment
AL	Analytic
BRDF	Bidirectional Reflectance Distribution Function
CFC	Chlorofluorocarbon
ESA	European Space Agency
GOMOS	Global Ozone Monitoring by Occultation of Stars
GSLS	Gauss-Seidel Limb Scattering
HALOE	Halogen Occultation Experiment
HIRDLS	High Resolution Dynamics Limb Sounder
HR	High Resolution
ISS	International Space Station
MC	Monte Carlo
MCMC	Markov Chain Monte Carlo
ML	Maximal Likelihood
MLS	Microwave Limb Sounder
MSE	Mean Squared Error
NASA	National Aeronautics and Space Administration
NIR	Near InfraRed
LOTUS	Long-term Ozone Trends and Uncertainties in the Stratosphere
MAP	Maximum a Posteriori
MIPAS	Michelson Interferometer for Passive Atmospheric Sounding
OMI	Ozone Monitoring Instrument
OMPS-LP	Ozone Mapping and Profiler Suite Limb Profiler
OSIRIS	Optical Spectrograph and InfraRed Imaging System
RTM	Radiative Transfer Model
SBUV	Solar Backscatter UltraViolet
SAGE	Stratospheric Aerosol and Gas Experiment
SCIAMACHY	SCanning Imaging Absorption SpectroMeter for Atmospheric CHartographY
SHOW	Special Heterodyne Observations of Water
SPARC	Stratosphere-troposphere Processes And their Role in Climate
SMR	Sub Millimeter Radiometer
STE	Stratosphere-Troposhere Exchange
UTLS	Upper Troposphere and Lower Stratosphere
WMO	World Meteorogical Association
UV	UltraViolet
UV-VIS-NIR	UltraViolet-Visible-Near InfraRed

Chapter 1

Introduction

Ozone is one of the most important trace species present in the Earth's atmosphere. In the troposphere, ozone acts as a pollutant and is commonly measured for input to air quality indexes. Stratospheric ozone shields the surface from harmful Ultraviolet (UV) radiation and also acts as a greenhouse gas. Chlorofluorocarbons (CFCs) in the stratosphere as a result of anthropogenic activities are the source of significant ozone depletion. Measurements of ozone are critical to monitor both ozone depletion and the effects of climate change on the global distribution of ozone.

Satellite measurements of limb scattered sunlight provide a remote sensing technique that is capable of obtaining globally resolved ozone measurements from space. Here, the instrument looks through the side, or the limb, of the atmosphere measuring sunlight that has been scattered. Measurements are primarily performed in the ultraviolet, visible, or near infrared spectral regions where scattering is dominant over atmospheric thermal emissions. The instrument either scans or images the vertical (altitude) dimension to obtain high vertical resolutions on the order of $\sim$1 km. Due to absorption and scattering effects the signature of trace species in the atmosphere is encoded into the observed spectrum. These measurements must then be inverted to obtain profiles of trace species in the atmosphere.

Inverting limb scatter measurements requires both a forward model and an inverse method. The forward model is a combination of the instrument's characteristics and a radiative transfer model. The radiative transfer model models radiative processes within the atmosphere and must account for both the sphericity of the Earth and multiple scattering. Measurement inversions, or retrievals, are performed by comparing the measurements to the model and iteratively updating the atmospheric state until convergence has been achieved. An overview of the limb technique, radiative transfer, and inverse theory is presented in Chapter 2.

A common assumption made in limb scatter retrievals is horizontal homogeneity, i.e., that the atmosphere only varies in the vertical direction. The assumption greatly simplifies both the retrieval method and the forward model required, allowing each vertical scan or image of the atmosphere to be processed independently. However, horizontal homogeneity breaks down in regions of the atmosphere with large horizontal gradients such as the polar vortex.

Several limb emission instruments have performed two-dimensional, or tomographic, retrievals which do not employ horizontal homogeneity (e.g. Degenstein et al., 2004; Degenstein et al., 2003; Livesey and Read, 2000). A tomographic retrieval takes advantage of the fact that successive limb measurements in the orbital track dimension overlap, measuring the same volume of the atmosphere multiple times from different angles. Using this information it is possible to directly retrieve structure in the along orbit dimension. Applying the technique requires an instrument that is sampling fast enough to have overlapping measurements, and a radiative transfer model that is capable of handling atmospheres that are not horizontally homogenous. The forward model required for limb scatter retrievals is considerably more complicated than that required for limb emission retrievals due to the presence of multiple scattering in the atmosphere.

The most recently launched limb scatter instrument is the Ozone Mapping and Profile Suite Limb Profiler (OMPS-LP) on-board the Suomi-NPP satellite. OMPS-LP images the vertical of the atmosphere in the range 0–80 km instead of vertically scanning, obtaining along track sampling that is suitable for tomography. There have been several proof of concept studies performed which apply tomographic techniques to limb scatter retrievals, however they all have either made simplifying assumptions or are too computational expensive to apply to operational retrievals (Puķıte et al., 2008; Rault and Loughman, 2013b).

This thesis describes the development of a tomographic retrieval for stratospheric ozone from measurements from the OMPS-LP instrument. Chapter 3 outlines the newly created SASKTRAN-HR radiative transfer model which breaks the assumption of horizontal homogeneity. In Chapter 4 a technique to approximate the Jacobian matrix in the case of two-dimensional atmospheres is presented, which is critical to creating a computationally efficient tomographic retrieval. Lastly, Chapter 5 puts everything together, applying a tomographic retrieval to the full six years of measurements currently available from OMPS-LP.

Chapter 2

Background

2.1 Ozone in the Atmosphere

Ozone makes up a relatively small fraction of the Earth's atmosphere, with maximum concentrations on the order of ∼10 ppmv. Figure 2.1 shows an example vertical profile of ozone in the atmosphere. The majority of ozone is present in the stratosphere, forming a peak in concentration known as the stratospheric ozone layer.

The primary source of ozone in the atmosphere was originally described by Chapman (1930), which begins with the photolysis of molecular oxygen by UV radiation,

$$O_2 + h\nu \rightarrow O + O. \tag{2.1}$$

The free oxygen atoms then combine with molecular oxygen with the help of a third molecule, M, to form ozone,

$$O + O_2 + M \rightarrow O_3 + M. \tag{2.2}$$

Ozone itself can be photolyzed back to molecular oxygen through the series of reactions,

$$O_3 + h\nu \rightarrow O + O_2, \tag{2.3}$$

$$O + O_3 \rightarrow O_2 + O_2, \tag{2.4}$$

$$O + O + M \rightarrow O_2 + M. \tag{2.5}$$

Models based solely upon the Chapman mechanism correctly predict the stratospheric ozone layer, but overestimate the amount of ozone present in the atmosphere.

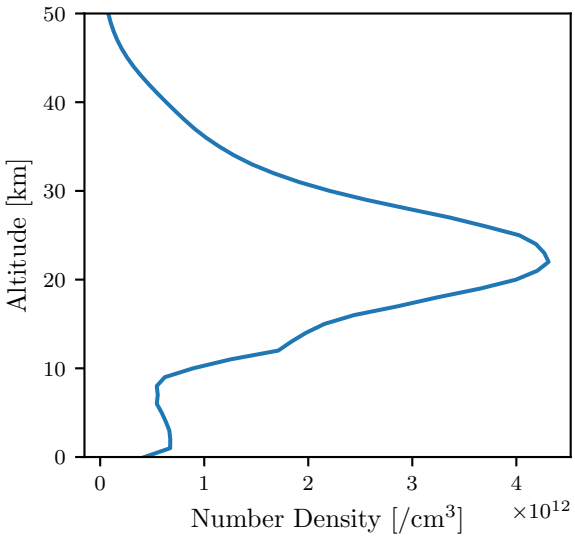

Figure 2.1: Vertical profile of ozone above Saskatoon, Canada as predicted by the McPeters et al. (1997) climatology for June 1st, 2017, 12:00 UTC.

The amount of ozone in the atmosphere is lower than expected by the Chapman model due to catalytic destruction cycles with chlorine, nitrogen, and hydrogen. The most well known source of ozone depletion is due to chlorine, which is responsible for the ozone hole. One simple idealized chlorine destruction cycle is,

$$\mathrm{Cl} + \mathrm{O_3} \rightarrow \mathrm{ClO} + \mathrm{O_2}, \tag{2.6}$$

$$\mathrm{ClO} + \mathrm{O_3} \rightarrow \mathrm{Cl} + 2\ \mathrm{O_2}. \tag{2.7}$$

Here, a single free chlorine is able to deplete ozone until it is either removed through transport or other chemical reactions.

The majority of chlorine in the stratosphere is due to anthropogenic production of CFCs. The catalytic destruction of ozone due to chlorine was known since the 1970s (Molina and Rowland, 1974); however it was believed that CFCs were chemically stable and unable to produce ozone catalyzing compounds. The subsequent observation of the antarctic ozone hole (Farman et al., 1985) eventually led to the discovery that heterogeneous reactions with CFCs on the surfaces of polar stratospheric clouds produce the catalyzing compounds causing ozone depletion (Solomon, 1999). It is generally thought that the enactment of the Montreal protocol in 1987 halted the decrease of stratospheric ozone and that stratospheric ozone has

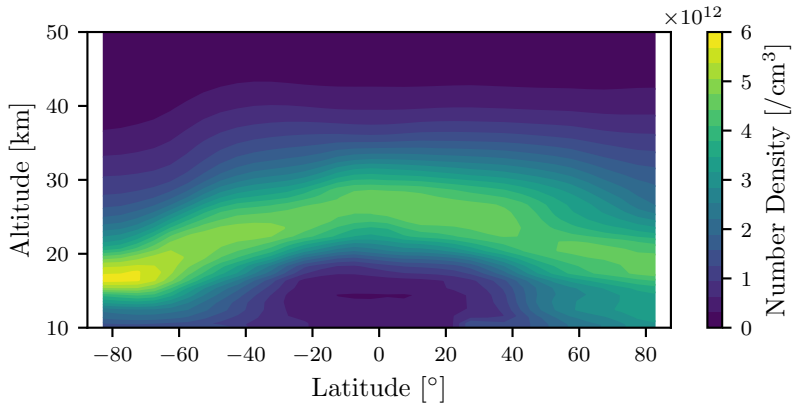

Figure 2.2: Zonal distribution of ozone in the atmosphere as a function of altitude and latitude as measured by MLS for June, 2017.

begun to recover (WMO (World Meteorological Organization), 2014). However the expected rate of recovery is small, on the order of $1-5\%$ per decade, and there are large uncertainties on the rate of recovery (Harris et al., 2015).

Atmospheric chemistry correctly predicts the vertical distribution of ozone in the atmosphere, however there is also a latitudinal distribution due to circulation patterns. Figure 2.2 shows the zonal distribution of ozone measured by the Microwave Limb Sounder (MLS, Waters et al., 2006) instrument for June 2017. Generally, more ozone is observed in the polar latitudes (in particular, the winter hemisphere) than the tropical regions, even though the majority of ozone production should occur in the tropics due to the larger radiation amounts. The large scale transport of tropical air first upwards, then towards the poles, and then downwards, is known as the Brewer-Dobson circulation (Brewer, 1949; Dobson, 1956).

The Brewer-Dobson circulation is a meridional, residual flow of the primarily zonal circulation patterns and is driven by atmospheric waves. The circulation is not specific to ozone and drives the meridional structure of many trace species in the atmosphere. The transport of tropical air to the poles is typically on the order of a few years. The Brewer-Dobson circulation is expected to accelerate in the coming years due to the effects of climate change, having a noticeable effect on the global distribution of ozone (Butchart, 2014). Acceleration of circulation patterns can cause long term changes in stratospheric ozone which can cause difficulties in detecting and attributing recovery due to the Montreal protocol (Wargan et al., 2018).

The largest effect ozone has on the Earth's atmosphere is its effect on the radiation budget. Ozone absorbs UV radiation, shielding the surface from its harmful effects. Ozone emits radiation at longer wavelengths, acting as one of the most important greenhouse gases. Study of these effects, and in particular, how changes in ozone are expected to influence the Earth due to climate change are of increasing importance.

Tropospheric ozone acts as a pollutant, and is a common measure that is used in many air quality indexes. While there are some natural sources for ozone in the troposphere, the majority of ozone originates through pollution. Vehicle exhaust, industrial emissions, etc., release ozone precursors such as NO_x and CO, which undergo chemical reactions to produce ozone. Tropospheric ozone is of particular importance as a greenhouse gas both due to its location in the atmosphere and its anthropogenic nature.

2.2 Atmospheric Limb Measurements

One of the first instruments capable of measuring the quantity of ozone in the atmosphere is the Dobson spectrophotometer (Dobson, 1931). The instrument, located on the surface looking up, measures the intensity of light at two wavelengths in the UV, one that is sensitive to ozone absorption and one that is not. The ratio of these two measurements provides information on the total column of ozone above the instrument in the atmosphere. Similar instruments are still in operation today and a large network of ground based ozone observations are available; however, these are still point measurements of the atmosphere. Fully global measurements of the atmosphere's distribution of ozone were not available until the satellite era.

Perhaps the most well known satellite based ozone monitoring instrument are the Solar Backscatter UltraViolet (SBUV) series of instruments. SBUV measures back-scattered sunlight using the nadir viewing geometry, which is shown conceptually in Fig. 2.3. The back-scattered sunlight is attenuated based on the amount of ozone present, and these measurements in principle can be inverted to obtain a total column amount of ozone. Variations of the SBUV instrument have been launched semi-continuously over the previous decades and merged 40+ year data records are available (Frith et al., 2014).

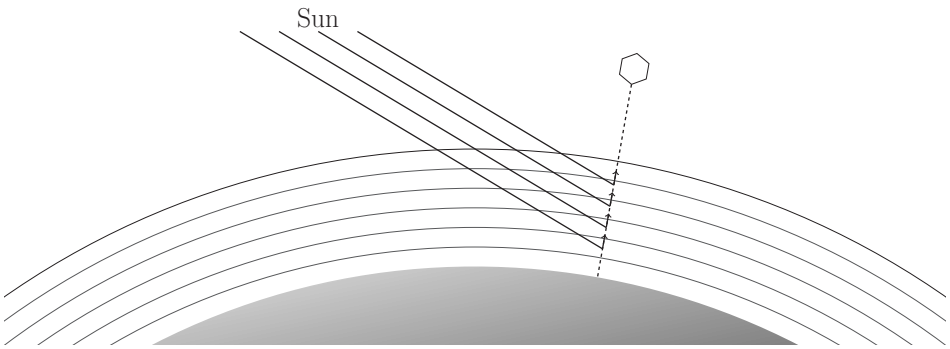

Figure 2.3: Conceptual drawing of the nadir viewing geometry.

Nadir measurements are able to obtain excellent near-global coverage, however information in the vertical dimension is limited as only a single line of sight is used. For a strongly absorbing species such as ozone, different wavelengths will probe different vertical depths of the atmosphere. SBUV uses this information to obtain vertical resolutions of approximately 6–15 km (Bhartia et al., 2013). Nevertheless, nadir instruments are unable to obtain vertical resolutions on the order of ∼1 km in the stratosphere.

Global, high vertical resolution, measurements of stratospheric ozone became available with the launch of the Stratospheric Aerosol and Gas Experiment (SAGE, McCormick et al., 1979) instrument. SAGE used the occultation technique, where the instrument views through the side, or *limb*, of the atmosphere straight at the sun, which is shown in Fig. 2.4. The instrument tracks the sun as it sets or rises, obtaining a profile of attenuation as a function of altitude. These measurements may be used to obtain a vertical profile of ozone as a function of altitude with resolutions of ∼1 km (Chu and McCormick, 1979).

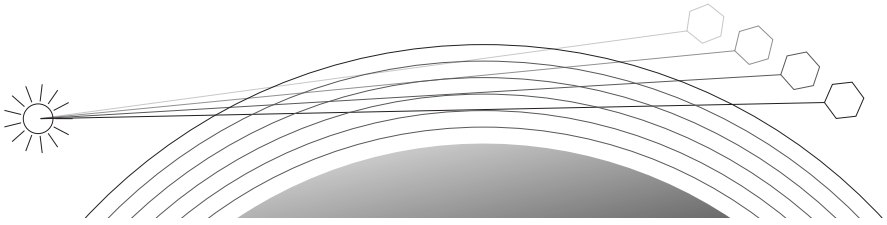

Figure 2.4: Conceptual drawing of the occultation remote sensing technique.

After the success of SAGE, numerous other solar occultation instruments capable of measuring stratospheric ozone were launched. Some of these are, SAGE II, a follow-on instrument to SAGE, was launched in 1984 (Mauldin III et al., 1985), the Halogen Occultation

Experiment (Russell et al., 1993) in 1991, the Atmospheric Chemistry Experiment (Bernath et al., 2005) in 2003, and SAGE III on-board METEO-M in 2001 and on the International Space Station recently in 2017.

While instrumental improvements continue to be made, the occultation measurement technique imposes a fundamental limit on the amount of data that can be collected. During each orbit it is only possible to view one sunrise and one sunset, leading to two measured vertical profiles. A low earth orbit satellite typically orbits the Earth $\sim$15 times a day, leading to $\sim$30 vertical profiles per day. The Global Ozone Monitoring by Occultation of Stars (Kyrölä et al., 2004) instrument is able to obtain orders of magnitude more profiles per day through stellar occultation, however data quality can be dependant on the brightness of the star used.

In an attempt to combine the good global coverage of nadir measurements with the vertical resolution of occultation measurements, the limb viewing technique was developed. A conceptual drawing of the limb viewing geometry is shown in Fig. 2.5. The viewing geometry is similar to occultation in that the instrument looks through the limb of the atmosphere, however measurements are performed looking into dark space rather than the sun or a star. In this case what is measured is either light that has been scattered into the instrument's line of sight, or direct emission from atmospheric constituents. The limb technique has the advantage that measurements can be taken at any time (or at least, the daylit portion of the orbit in the case of scattered light) instead of being limited to sunrise and sunset. However, it is considerably more difficult to invert the spectral measurements to obtain vertical profiles of quantities in the atmosphere.

The atmospheric limb inverse problem, commonly referred to as a limb retrieval, is non-linear and is usually solved through iterative techniques. The procedure begins with a first guess of the atmospheric state and simulating what the instrument would observe for this hypothetical atmospheric state. The simulation requires accurately modelling radiative processes and transfer within the atmosphere. Based on the difference in measurement between what is observed by the instrument and what is simulated by the forward model the atmospheric state is updated. The process is iterated until convergence has been achieved. The inverse problem is fundamentally ill-posed as the quantity of interest, the atmospheric state,

is virtually a continuous quantity. Despite these complications, the inverse problem has been extensively studied and practical techniques have been developed (Rodgers, 2000).

Beginning in the early 2000's there was a surge of newly launched limb instruments capable of measuring stratospheric ozone. The Optical Spectrograph and InfraRed Imaging System (OSIRIS, Llewellyn et al., 2004), a limb scatter instrument, was launched on-board the Odin satellite in 2001. Odin also contains the Sub Millimeter Radiometer (Murtagh et al., 2002) which measures thermal emissions in the microwave spectrum. The European Space Agency's Envisat platform, launched in 2002, houses a limb scatter instrument the SCanning Imaging Absorption SpectroMeter for Atmospheric CHartographY (SCIAMACHY, Bovensmann et al., 1999) and an infrared emission instrument, the Michelson Interferometer for Passive Atmospheric Sounding (MIPAS, Fischer et al., 2008). Another infrared emission instrument the High Resolution Dynamics Limb Sounder (HIRDLS) and a microwave emission instrument, MLS, are orbiting on NASA's Aura satellite. The most recent limb instrument launched is the Ozone Mapping and Profiler Suite Limb Profiler (OMPS-LP) on-board the Suomi-NPP satellite (Flynn et al., 2006).

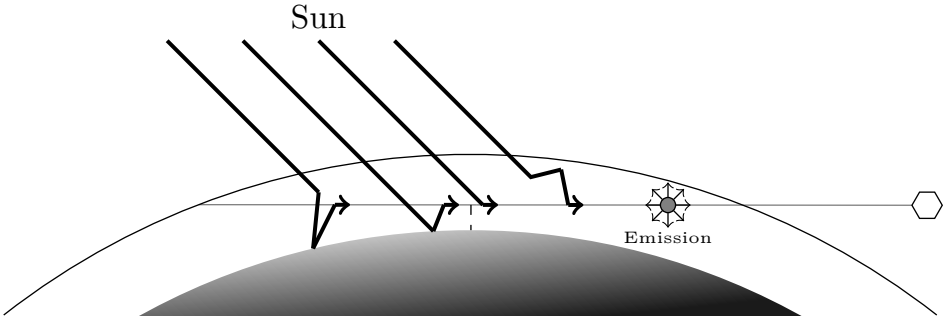

Figure 2.5: Conceptual drawing of the limb scatter/emission remote sensing geometry.

2.2.1 OMPS-LP

OMPS-LP is the most recently launched dedicated limb scatter instrument and measures scattered sunlight from the Suomi-NPP platform. Spectral information is obtained in the 290–1000 nm region using a prism disperser. The spectral resolution varies from ∼1 nm in the UV to ∼40 nm in the near infrared. Figure 2.6 shows an example spectrum measured by OMPS-LP at various tangent heights.

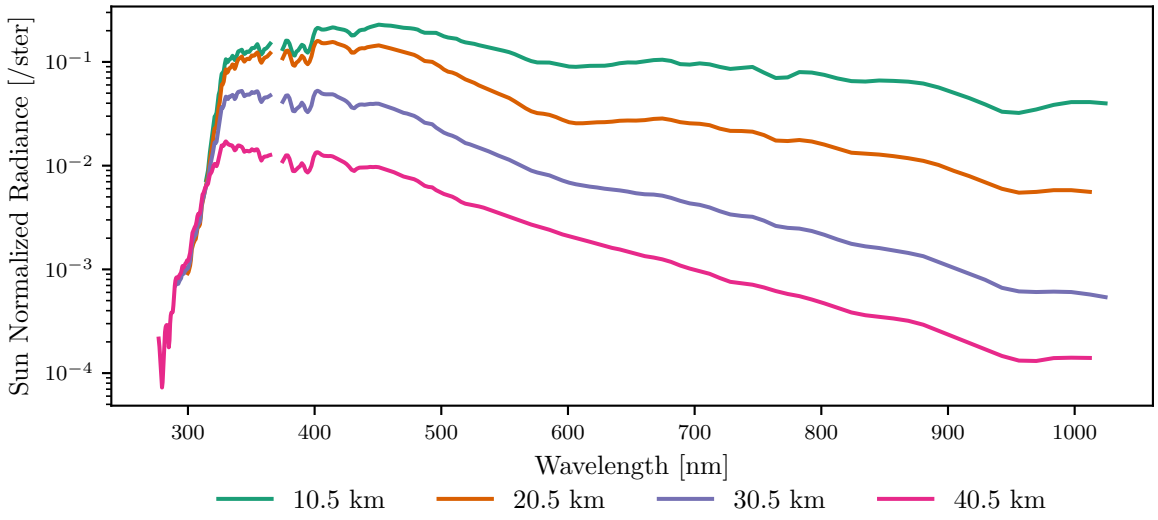

Figure 2.6: Example spectrum measured by the central slit of OMPS-LP for several tangent altitudes. Measurements were taken on May 25th, 2015.

OMPS-LP is unique in that it is the only satellite-borne limb scatter instrument that images the vertical rather than scanning. Through imaging, OMPS-LP takes three vertical images of the atmosphere every ∼19 s (∼125 km along the orbital track). The three vertical images are separated in the across-track direction by 250 km. Figure 2.7 shows the tangent point locations for all OMPS-LP measurements on April 26th, 2015. Each day approximately 7000 vertical, spectrally resolved images are taken of the atmosphere. The latitudinal coverage of OMPS-LP varies throughout the year due to its near polar orbit.

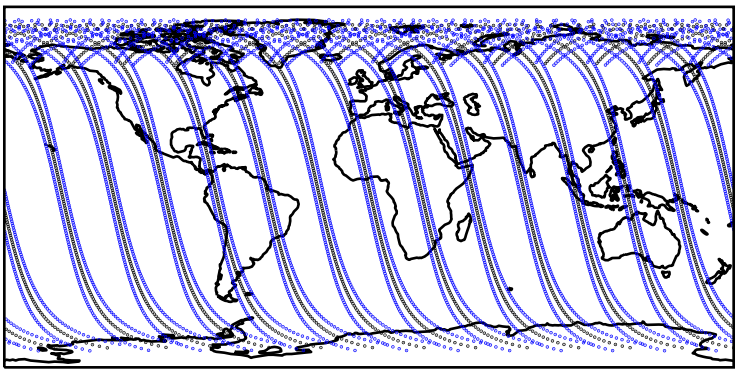

Figure 2.7: Tangent point locations of OMPS-LP measurements for April 26th, 2015. Black dots indicate a vertical image for the central slit, while blue dots represent images from the left and right slits.

Suomi-NPP is in sun-synchronous, near polar orbit with an inclination of 98.7° and an ascending node local time of equator crossing at roughly 1:30 pm. Figure 2.8 shows the year long latitudinal coverage of OMPS-LP. Through this orbit, OMPS-LP is able to uniformly cover the 60° S to 60° N latitude region year long, with coverage extending to 82° in each poles respective summer.

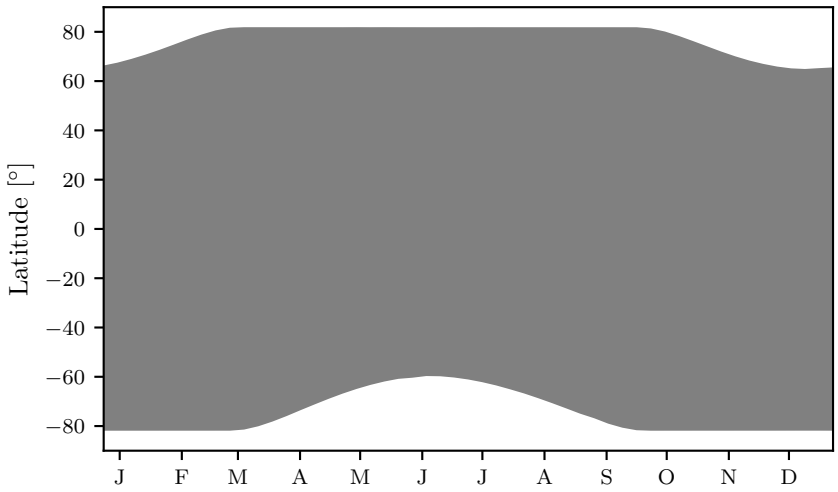

Figure 2.8: Daylit portion of the OMPS-LP orbit for 2016. Gray shaded area indicates that radiances at a given latitude are observed during daytime by OMPS-LP.

2.2.2 The Need for Limb Ozone Measurements

Limb measurements the only way to obtain high vertical resolution (∼1 km) measurements of ozone in the stratosphere on a global scale. As such, limb measurements are the most useful to domains requiring good vertical resolution. Section 2.1 provided an overview of the importance of ozone as part of the Earth's atmosphere, here we present a non-exhaustive list of example uses of limb ozone measurements that highlight the advantages these types of measurements offer.

One of the primary uses for limb ozone measurements today is in the determination of long-term stratospheric ozone change. Ozone decline due to CFCs was expected to diminish following the signing of the Montreal Protocol in 1987, which banned many uses of CFCs. Long-term (∼35 year) nadir records show a clear decrease in total column ozone until ∼1997, with an apparent levelling off with no significant increase post 1997 (Weber

et al., 2018). Similar trend studies have been performed with decadal limb/occultation data records (Steinbrecht et al., 2017, and references therein), which generally show that upper stratospheric ozone is increasing a rate of 1.5–2.5 % per decade. Recently Ball et al. (2018) used limb measurements to show that increasing trends could not be seen in the nadir datasets due to the increase being offset by a decline in lower stratospheric ozone, which could be explained through circulation/dynamical changes in the Upper Troposphere and Lower Stratosphere (UTLS) (Wargan et al., 2018).

Ozone is also commonly used as a tracer species to assess both global and small scale transport, dynamics, and circulation. Large scale transport of ozone is primarily controlled by the Brewer-Dobson circulation, which transports ozone rich tropical air to the poles. Continued study of the Brewer-Dobson circulation is critical as changes due to climate change have been linked to decreases in stratospheric water vapour (Randel et al., 2006), the most important greenhouse gas.

The study of ozone in the UTLS region is also of particular importance for the study of Stratosphere-Troposhere Exchange. Due to the temperature inversion at the tropopause there is little transport between the stratosphere and the troposphere. However, there are cases where the tropopause "folds" over itself, causing a filament of stratospheric air to be released into the troposhere. These stratospheric intrusions have been linked to high ozone amounts at the surface of the Earth. Olsen et al. (2008) showed that stratospheric intrusion events can be observed with the ~ 1 km vertical resolution measurements of HIRDLS. Wargan et al. (2015) demonstrated that assimilating measurements from MLS underestimated the amount of filaments in the UTLS due to the limited vertical resolution of MLS ($\sim 2.5 - 3\,\mathrm{km}$ resolution in the UTLS).

The measurement of tropospheric ozone is particularly important as ozone is a pollutant, and is a common factor included in air quality indexes. Nadir instruments are able to take measurements of the total column ozone amount, which includes the tropospheric column, however it is difficult to isolate the tropospheric column as the majority of ozone is in the stratosphere. Limb measurements are able to accurately resolve the stratosphere, but have trouble probing deep into the troposphere due to the presence of clouds. One technique to obtain measurements of the tropospheric column is the idea of limb/nadir matching.

Here, measurements from a limb instrument are combined with co-located measurements from a different nadir instrument. The limb instrument is able to measure the stratospheric column, while the nadir instrument measures the sum of the stratospheric and tropospheric column. This was first done by Ziemke et al. (2006) using Ozone Monitoring Instrument nadir measurements matched with limb measurements from MLS. Ebojie et al. (2014) performed a similar analysis using measurements from SCIAMACHY in both limb and nadir modes.

2.2.3 Limb Tomography

A common assumption in limb retrievals is horizontal homogeneity. Here the atmosphere is assumed to only vary in the altitude dimension and is homogeneous in the horizontal direction. This simplifies the problem in that every vertical set of measurements can be treated independently, each resulting in a vertical profile of retrieved quantities. The assumption is somewhat justified for limb measurements since the majority of the signal originates from the tangent point due to the geometry of the problem. However, the effect of the horizontal homogeneity assumption is not well understood and there are common situations where the assumption may not be valid.

Horizontal homogeneity breaks down when there are large gradients along the line of sight direction. McLinden et al. (2006) showed that diurnal effects along the line of sight for photochemically active species can have a significant impact on one-dimensional limb scatter retrievals. A study by Kiefer et al. (2010) demonstrated that inhomogeneities in the atmospheric temperature field cause systematic biases in one-dimensional limb emission retrievals for MIPAS, in particular in regions near the polar vortex. One retrieval processor for MIPAS is capable of handling the problem with a two-phase approach (von Clarmann et al., 2003). First, an orbit of measurements is retrieved (one-dimensional) to obtain an estimate of the horizontal gradient; a second pass of the orbit is then performed using information from the previous phase in the forward model (but still performing a one-dimensional retrieval). However, a more systematic approach to account for horizontal inhomogeneity is to abandon the horizontal homogeneity altogether.

If the instrument is capable of sampling fast enough in the along orbital track dimension it is possible to break the assumption of horizontal homogeneity and directly retrieve structure

along this dimension. This two-dimensional, or tomographic, retrieval was first demonstrated using simulated limb emission measurements from MLS by Livesey and Read (2000). Similar techniques have also been applied to infrared measurements from the OSIRIS infrared imager (Degenstein et al., 2004; Degenstein et al., 2003) and MIPAS (Steck et al., 2005). The main complications involved in developing tomographic retrieval technique are obtaining a radiative transfer model capable of handling multi-dimensional atmospheres, and designing the inverse method itself.

While there have been multiple successful attempts at performing tomographic retrievals for thermal emission measurements, only proof of concept studies exist for limb scatter measurements. The primary reason for the discrepancy is the difficulty of modeling the radiance for two- and three-dimensional atmospheres when multiple scattering is present, which is necessary for limb scatter measurements in the UV and visible spectral regions. Puķıte et al. (2008) provided a two-dimensional retrieval of NO_2 and OClO from SCIAMACHY measurements, however a Monte-Carlo forward model was used (Deutschmann et al., 2011), which is computational prohibitive for processing large amounts of data. Rault and Spurr (2010) performed a two-dimensional ozone retrieval for simulated OMPS-LP measurements, but the multiple scattering problem was sidestepped by only using a single scatter radiative transfer model. The present work focuses on developing a two-dimensional retrieval algorithm for OMPS-LP that accounts for multiple scatter and is computationally efficient enough to apply to the entire 6+ years of available measurements.

2.3 Atmospheric Radiative Transfer

The general process of obtaining ozone, or other trace species, from limb scatter measurements is:

1. Create a first guess of the atmospheric state
2. Simulate what the instrument would have measured using the current best guess of the atmosphere
3. Compare the simulated measurements to the actual measurements and update the

atmospheric state based on this information

4. Go back to 2, iterating until convergence has been achieved

This section develops the theory for the second point, radiative transfer within the Earth's atmosphere driven by the solar forcing. Also discussed is the practical implementation of the theory into what is known as Radiative Transfer Models (RTMs). Chapter 3 describes in detail the implementation of a newly created RTM that is suitable for the final goal of the thesis, a tomographic retrieval from OMPS-LP measurements.

2.3.1 The Radiative Transfer Equation

In general, radiative transfer is a problem that is described by Maxwell's equations and the quantum theory of molecular spectroscopy. Since a direct solution of these equations in a system as complicated as the atmosphere is difficult, if not impossible, various approximations have been developed to handle the problem. The most commonly used framework for atmospheric radiative transfer was developed by Chandrasekhar (1960), where the *spectral radiance*, I, is treated as the fundamental quantity.

The spectral radiance (which is often simply referred to as radiance in the field of atmospheric radiative transfer) for a radiating surface with area A is defined as,

$$I = \frac{dE}{d\hat{\Omega} dA \cos(\theta) d\lambda dt}, \tag{2.8}$$

where E is energy, $\hat{\Omega}$ is solid angle, *theta* is the angle between the observer and the surface's normal direction, λ is wavelength, and t is time. The radiance is the energy emitted by a surface per unit area, solid angle, wavelength, and time. The most common units for radiance in atmospheric radiative transfer are,

$$[I] = \frac{\text{photons}}{\text{s nm sr cm}^2}. \tag{2.9}$$

Equivalent photon counts are used as a measure of energy since most practical measurements of radiance involve counting photons. It should be noted that when expressing the radiance using photon counts it does not have physical units of energy as Eq. (2.8) indicates, however it is possible to convert to energy knowing each photon carries an energy of hc/λ where h

is the Planck constant and c is the speed of light. The radiance is a convenient quantity as most measurements from optical instruments can be represented by a scalar product between an instrument response function and the radiance. For example, the response function for an optical spectrometer would include things such as integration time, spectral resolution, and field of view.

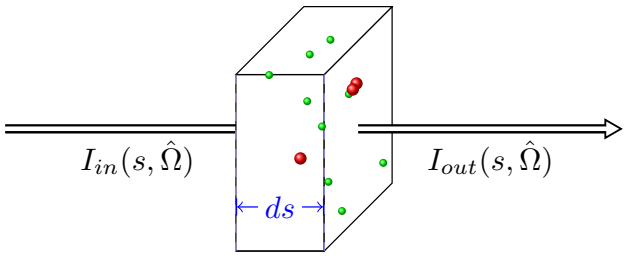

Figure 2.9: Conceptual drawing of radiance passing through a slab of infinitesimal width. The slab contains multiple species (red and green dots) which interact with the incoming radiance.

The equation of radiative transfer can be heuristically derived by considering an incoming radiance incident on an infinitesimal slab, see Fig. 2.9. While passing through the slab, the radiance can be attenuated through interaction with the molecules. The wavelength dependent likelihood of interaction is known as the cross section, σ, with units of area, and for convenience it is often split into separate components for scattering and absorption interactions, $\sigma = \sigma_{\text{scat}} + \sigma_{\text{abs}}$. In principle the cross section can be calculated through quantum theory, however in practice it is usually looked up through experimental databases. As an example, the ozone absorption cross section used in this work is shown in Fig. 2.10. Large absorption is seen in the UV part of the spectrum, with sharp structures present in 320–360 nm region. Broad absorption is also observed in the visible part of the spectrum, with a peak near 600 nm.

The attenuation effect is described by the Beer-Lambert law,

$$dI(s,\hat{\Omega}) = I_{out}(s,\hat{\Omega}) - I_{in}(s,\hat{\Omega}) = -ds \sum_i n_i(s)\sigma_i I(s,\hat{\Omega}), \tag{2.10}$$

where the sum is over each species, n_i is the number density of species indexed by i, and s is the distance along some known path. Note that because of the directional dependence, specifying s is equivalent to specifying position in a three dimensional space. The wavelength

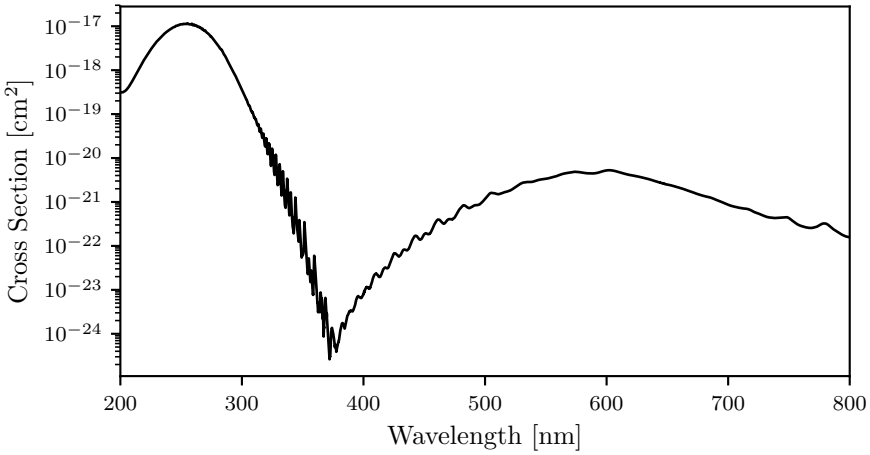

Figure 2.10: Ozone absorption cross section measured by Brion et al. (1993), Daumont et al. (1992), and Malicet et al. (1995).

dependent *extinction* is defined as,

$$k(s) = \sum_i n_i(s)\sigma_i, \tag{2.11}$$

and is often also separated into scattering and absorption components, $k = k_{\text{scat}} + k_{\text{abs}}$. The slab may also contain a source of radiation, which admits a modification of the form,

$$\frac{dI(s,\hat{\Omega})}{ds} = J(s,\hat{\Omega}) - k(s)I(s,\hat{\Omega}), \tag{2.12}$$

where the quantity J is called the *source function*, and will be explained in detail later. Often the equation of radiative transfer is written in integral form,

$$I(\vec{r}_0,\hat{\Omega}) = I(s_{\text{end}},\hat{\Omega})e^{-\tau(0,s_{\text{end}})} + \int_{s_{\text{end}}}^{0} J(s,\hat{\Omega})e^{-\tau(0,s)}\,ds, \tag{2.13}$$

where $\vec{r}_0$ is the observer location, s_{end} is the distance to the end of the ray path respectively, and τ is the *optical depth* given by,

$$\tau(a,b) = \int_a^b k(s)\,ds. \tag{2.14}$$

Note that the convention for s is to be negative in the direction away from the observer. If the source term is known, then the radiance can be calculated (numerically if need be) with just one line integral.

As a side note, consider that the radiative transfer equation was derived using the phenomenological idea of radiance rather than using rigorous electromagnetic theory. Recently

the radiative transfer equation has been re-derived from first principles by Mishchenko (2008) under assumptions that are typical for atmospheric conditions.

2.3.2 Sources of Radiation

Emission

One common source of radiation in the atmosphere is thermal emission from atmospheric constituents themselves or from the Earth. In this case the source function takes the form of the Planck function,

$$J_{\text{emission}}(s) = k(s)\frac{2hc^2}{\lambda^5}\frac{1}{\exp(\frac{hc}{\lambda k_b T(s)}) - 1}, \tag{2.15}$$

where h is Planck's constant, c is the speed of light in vacuum, k_b is Boltzmann's constant, and $T(s)$ is temperature at the location parameterized by s. The source function for thermal emission is isotropic. While the source function for a surface is continuous, molecules are only able to emit at discrete wavelengths corresponding to typically rotational-vibrational transitions.

In the ultraviolet, visible, and near-infrared (UV-VIS-NIR) spectral region emission processes are negligible compared to solar scattering. The thermal emission source function is the dominant source term in the far infrared and microwave spectral regions. For UV-VIS-NIR radiative transfer modelling the thermal emission source is usually neglected, with the possible exception of night-time measurements where there is little scattering.

At some wavelengths, photochemical emission can seen in limb scatter spectra. The most well known photochemical emission originates from airglow from the oxygen A band near 762 nm, which can be observed at high altitudes (e.g. Sheese et al., 2010). While it is possible to model and include this type of emission directly, it is not necessary for the retrieval of ozone as emission sensitive wavelengths can be explicitly ignored.

Scattering

The *spectral irradiance* (once again, commonly the spectral notation is implied in the field of atmospheric radiative transfer) is defined as power per unit area per unit wavelength, and is similar to radiance except that it is not per unit sold angle. If an irradiance, F, is incident

with direction $\hat{\Omega}_{in}$ on a single molecule with scattering cross section σ, then the outgoing scattered radiance far field is,

$$I(\hat{\Omega}_{out}) = F(\hat{\Omega}_{in})\sigma p(\hat{\Omega}_{in}, \hat{\Omega}_{out}), \tag{2.16}$$

which, the angular component of the scattered field is encapsulated by the *phase function*, $p(\hat{\Omega}_{in}, \hat{\Omega}_{out})$. The phase function is normalized such that,

$$\int_{4\pi} p(\hat{\Omega}_{in}, \hat{\Omega}_{out}) d\hat{\Omega}_{out} = 1, \tag{2.17}$$

where $\int_{4\pi}$ represents the surface integral over a unit sphere. Another common convention is to normalize the phase function to integrate to 4π over the unit sphere; however, this work will follow the convention that it is normalized to 1. Formally, the phase function for any arbitrary scatterer can be defined as,

$$p(\hat{\Omega}_{in}, \hat{\Omega}_{out}) = \frac{1}{\sigma} \frac{dI(\hat{\Omega}_{out})}{dF(\hat{\Omega}_{in})}, \tag{2.18}$$

which reveals the phase function as the angular component of the differential scattering cross section.

In atmospheric radiative transfer the assumption is made that molecules are sufficiently spaced that they can each be treated independently. The assumption may be restated that a volume of N identical particles scatters a field that is equal to N times the field scattered by a single particle. The source function was defined such that $J(\hat{\Omega})$ was the scattered radiance per unit length. Thus, for a medium with scattering extinction k_{scat}, and incident irradiance $F(\hat{\Omega}_{in})$, the scattered source function is,

$$J(s, \hat{\Omega}) = k_{\text{scat}}(s) F(\hat{\Omega}_{in}) p(\hat{\Omega}_{in}, \hat{\Omega}_{out}). \tag{2.19}$$

Equation (2.19) can be used to derive an expression for direct scattering due to the solar irradiance. At any point in the atmosphere the incident irradiance due to the direct solar beam is the incident solar irradiance on the Earth attenuated through the Beer-Lambert law. Therefore, the single scattering source function is,

$$J_{\text{SS}}(s, \hat{\Omega}) = k_{\text{scat}}(s) F_{\text{sun}} e^{-\tau(s,\text{sun})} p(\hat{\Omega}_{sun}, \hat{\Omega}_{out}), \tag{2.20}$$

where $\tau(s, \text{sun})$ is the optical depth from a point in the atmosphere to the sun.

Light that has been scattered may also scatter again in the atmosphere any number of times, which is known as multiple scattering. Generally, at any point in the atmosphere there may be incoming radiation from any direction that may scatter into any outgoing direction, and thus the full scattering source function involves the integral over all directions,

$$J_{\mathrm{MS}}(s,\hat{\Omega}) = k_{\mathrm{scat}}(s)\int_{4\pi} I(s,\hat{\Omega}')p(s,\hat{\Omega},\hat{\Omega}')\,d\hat{\Omega}'. \tag{2.21}$$

If the multiple scattering source function is included in Eq. (2.13) then the radiative transfer equation becomes an integral equation of mixed Fredholm-Volterra type. Including the multiple scattering source function greatly complicates finding the solution of the equation.

For wavelengths in the UV to the near infrared multiple scattering is an important term that cannot be ignored. Figure 2.11 shows the contribution of various orders of scatter in a simulated radiance calculation. At all wavelengths the first scatter order is the dominant term as expected, however the second order of scatter remains non-negligible at all wavelengths. Scattering from higher orders than the second is important at shorter wavelengths where the atmosphere is optically thick, but drops off at higher wavelengths when the atmosphere becomes optically thin.

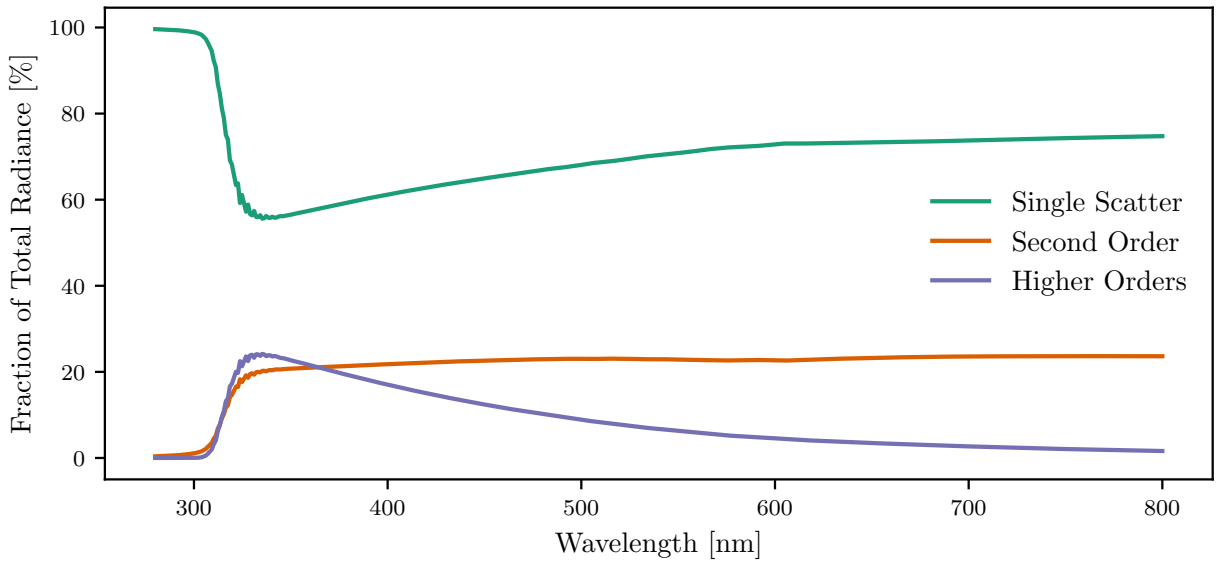

Figure 2.11: Contribution of various orders of scatter to the full radiance for a typical atmospheric scenario at 20 km tangent altitude. The percentage of contribution from the first, second, and all other orders of scatter are shown by the green orange and purple lines respectively.

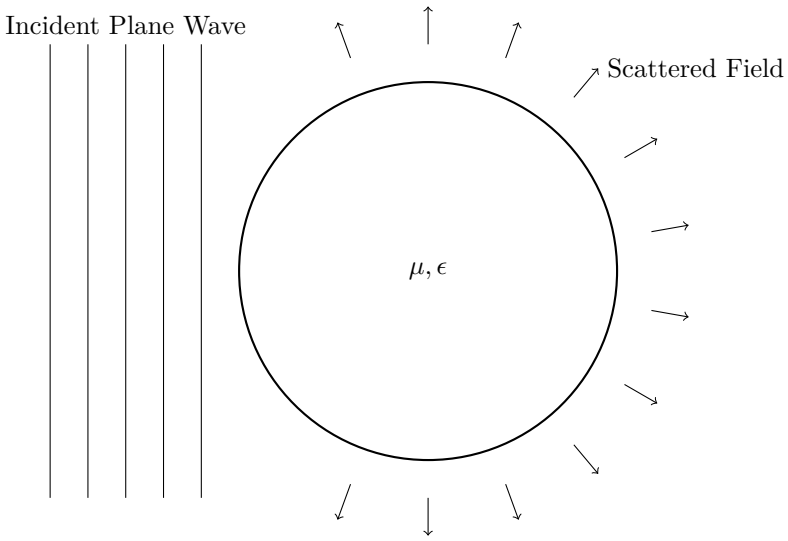

Figure 2.12: Conceptual diagram of the scattering problem for a single particle. A plane wave is incident on a dielectric sphere with properties, μ, ϵ, with the goal of calculating the scattered far field.

Since the assumption is made that molecules can be treated independently, the scattering cross section and the phase function may be calculated using Maxwell's equations directly applied to the microscopic system. The general problem involves a plane wave incident on the particle with given dielectric properties (see Fig. 2.12). The majority of atmospheric scattering occurs from molecular scattering, where the particle size is much less than the wavelength of light. In this case the incoming radiance induces a molecular dipole leading to dipole radiation and a form of scattering known as Rayleigh scattering. For a single molecule which Rayleigh scatters, the scattering cross section may be directly calculated as,

$$\sigma_{\text{ray}} = \frac{128\pi^5}{3}\frac{\alpha^2}{\lambda^4}, \tag{2.22}$$

where α is the molecular polarizability. The Rayleigh scattering phase function is also given as,

$$P_{\text{ray}}(\Theta) = \frac{3}{16\pi}(1 + \cos^2(\Theta)), \tag{2.23}$$

where Θ is the angle between the incoming and outgoing directions. Commonly the Rayleigh scattering cross section is modified to account for molecular anisotropy (Bates, 1984; King, 1923).

In the case of a spherical particle of arbitrary size, an exact solution of Maxwell's equations (for the situation of Fig. 2.12) exists, known as the Lorenz-Mie solution (Mie, 1908). Here,

the incident plane wave as well as the scattered and internal fields are expanded in an infinite series of vector spherical harmonics, with coefficients determined through matching boundary conditions on the particle's surface. The Lorenz-Mie solution is characterized by a quantity known as the *size parameter*,

$$x_s = \frac{2\pi r}{\lambda}, \tag{2.24}$$

where r is the particle radius. In the limiting case of small size parameters the Lorenz-Mie solution reduces to that of Rayleigh scattering. When the size parameter is on the order of $\sim$1, the Lorenz-Mie solution is a fast and practical method for computing scattering properties. There are numerous codes available to calculate the Lorenz-Mie solution, with perhaps the most well known, and the one used in this work, being that of Wiscombe (1980). When the size parameter is large, the Lorenz-Mie solution is slow to converge and often numerically unstable (physically this is interpreted as the increased variability of the incident plane wave over the surface exciting higher modes). For these reasons, scattering of spherical particles when the size parameter is on the order of $\sim$1 is commonly referred to as Mie scattering.

Mie scattering occurs in the Earth's stratosphere through stratospheric aerosols. Stratospheric aerosols primarily consist of a mixture of sulfuric acid and water droplets that are formed through chemical reactions with sulfur compounds. There are enhancements to stratospheric aerosol following injections of sulfates from large volcanic eruptions, however there is also a persistent stratospheric aerosol layer known as the Junge layer (Junge et al., 1961). Stratospheric aerosols do not have a single particle size, but instead follow a distribution of sizes on the orders of $\sim$ 100 nm. In situ measurements suggest that the particle size distribution is well approximated by a log-normal distribution during background loading conditions (Deshler et al., 2003).

Figure 2.13 shows a comparison of stratospheric aerosol and Rayleigh scattering for typical atmospheric conditions at an altitude of 20 km. For short wavelengths Rayleigh scattering is the dominant term in the atmosphere. The scattering cross section of the larger stratospheric aerosols decays at a rate slower than the $1/\lambda^4$ relationship of Rayleigh scattering, causing aerosol scattering to be as, or more, important at wavelengths longer than $\sim$ 700 nm. The larger particle size also causes a large fraction of the scattering to occur in the forward direction compared to the relatively flat phase function of Rayleigh scattering.

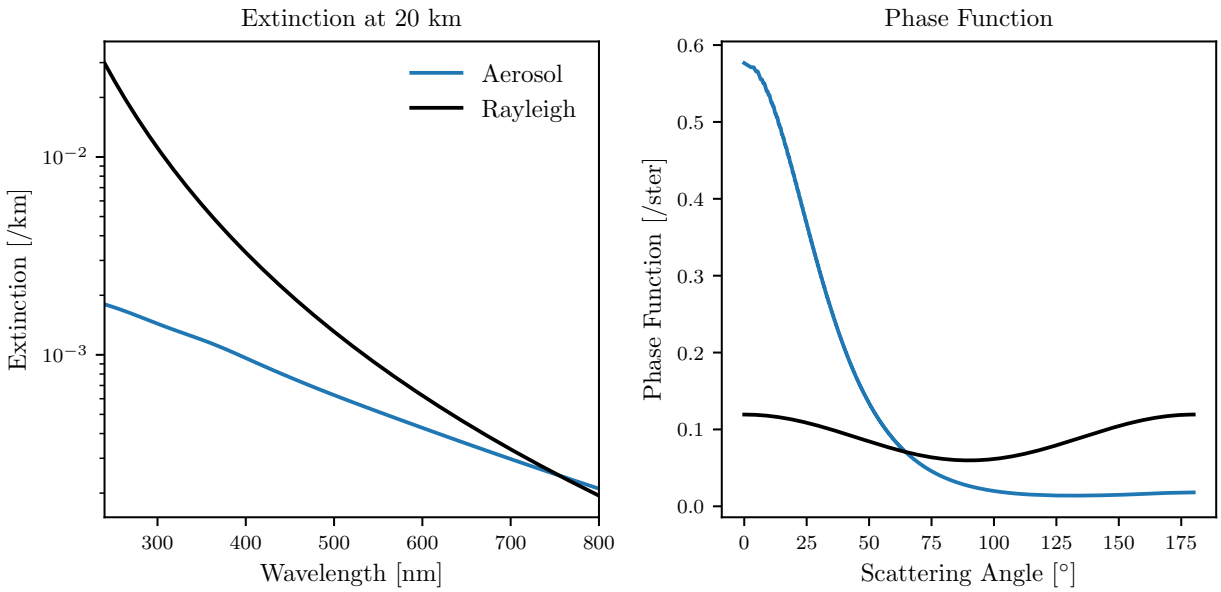

Figure 2.13: The left panel shows stratospheric aerosol and Rayleigh scattering extinction as a function of wavelength at an altitude of 20 km for standard atmospheric conditions. The right panel shows the scattering phase function for stratospheric aerosol and Rayleigh scattering.

Scattering with size parameters much greater than unity is predominantly done by clouds. These particles are usually non-spherical, and require more complicated methods to estimate their scattering properties (see Mishchenko et al., 1999, for a review of some of these techniques). While there has been some success in accounting for thin cirrus clouds in limb scatter calculations, these effects are difficult to model and usually act as a lower bound for how low limb scatter measurements can probe the atmosphere.

Inelastic, or Raman, scattering also occurs within the Earth's atmosphere. While Raman scattering can occur at all wavelengths with the same $1/\lambda^4$ dependance of Rayleigh scattering, it is most noticeable in the 400–500 nm spectral region where it causes the sharp Fraunhofer features of the solar spectrum to appear "filled in" (Vountas et al., 1998). The effect of inelastic scattering is relatively small, and in particular has negligible effect on ozone sensitive wavelengths.

Surface Reflectance

The last term that must be accounted for is the reflectance of the Earth's surface. This term is the most important when the instrument itself is looking at the surface, but it also important for any situation with multiple scattering. Surface reflectance is usually not written in terms of a source function, but instead can be handled through the end of the ray path term in Eq. (2.13).

Surface reflectance is parameterized with that is known as the Bidirectional Reflectance Distribution Function (BRDF). The formal definition of the BRDF is,

$$f(\hat{\Omega}_{in}, \hat{\Omega}_{out}) = \frac{dI(\hat{\Omega}_{out})}{dF(\hat{\Omega}_{in})}, \tag{2.25}$$

where I is the reflected radiance and F is the incident irradiance on the surface. The expression can be integrated to obtain the outgoing radiance at a surface,

$$I(\hat{\Omega}_{out}) = \int_{2\pi} I(\hat{\Omega}_{in}) f(\hat{\Omega}_{in}, \hat{\Omega}_{out}) d\hat{\Omega}_{in}, \tag{2.26}$$

where the integral is over the upper hemisphere of the unit sphere. The BRDF term is mathematically similar to that of the phase function and can be thought of as a phase function for surface reflectance.

The simplest BRDF is that of a Lambertian surface where the observed radiance of the surface is independent of viewing angle. Here, the BRDF is written,

$$f_{\text{Lambertian}}(\hat{\Omega}_{in}, \hat{\Omega}_{out}) = \frac{a}{\pi}, \tag{2.27}$$

where a is a constant. The *albedo* is defined as the ratio between incoming and outgoing energy of a surface and for the Lambertian case is equal to a. An albedo of one indicates that the surface fully reflects all light incident onto it.

The true BRDF of the Earth's surface is more complicated than a Lambertian surface. Various surfaces' BRDFs have significant angular dependence, an extreme example is glinting, or direct reflection, off of ice or water. Wavelength dependant reflectance is also common, one example is the "red edge" where vegetation is known to reflect stronger at longer wavelengths in the visible spectrum. Despite these complications most limb scatter retrieval techniques assume a Lambertian surface.

2.3.3 Radiative Transfer Models

There exist a large number of computer codes written to solve the radiative transfer problem, known as Radiative Transfer Models (RTMs). RTMs are often written with a specific problem in mind, and thus end up being only applicable in a specific domain. What domain a model is useful for is determined by the assumptions employed in the implementation.

This section outlines some common major assumptions that are relevant in the context choosing a model for tomographic retrievals using limb scattered sunlight. Models are usually specialized to solve the radiative transfer problem within a specific spectral domain. For example, in the far infrared region it is not necessary to include the scattering source term in the calculation, greatly simplifying the model. When including the scattering source term the equation becomes more complicated, and an integral equation must be solved. Conversely, models specialized for short wavelengths do not usually include emission terms as they are negligible compared to scattering. Radiance from multiply scattered light in the limb geometry has been shown to be an important term that cannot be neglected (Oikarinen et al., 1999).

Models can further classified by the geometry employed in the solution. Many models assume that the Earth is flat which is known as the plane parallel assumption (e.g. Stamnes et al., 2000). However, it has been shown that plane parallel models are not suitable for the limb viewing geometry (McLinden and Bourassa, 2010). For this reason some models are referred to as spherical, indicating that they do not assume a flat earth in the calculation.

There are several RTMs that account for multiple scattering in a spherical atmosphere. Some examples of RTMs that have been successively used in the retrieval of trace species from limb scatter observations are: SCIATRAN (Rozanov et al., 2014) for SCIAMACHY measurements, SASKTRAN (Bourassa et al., 2008; Zawada et al., 2015) for OSIRIS measurements, and Gauss-Seidel Limb Scattering (Loughman et al., 2015) for SAGE III and OMPS-LP measurements. Extensive comparisons have been performed between these RTMs (Bourassa et al., 2008; Loughman et al., 2004) (among others), and they generally agree at approximately the 1% level. Comparisons are usually performed against a reference Monte Carlo model, such as Siro (Oikarinen et al., 1999), since the Monte Carlo method requires

fewer assumptions with the trade off of computational efficiency.

A common assumption made in deterministic models is horizontal homogeneity, the assumption that the atmosphere only varies in the vertical direction. In this case, the scattering source function of Eq. (2.21) admits a symmetry around the solar direction, reducing its dimensionality from five to four. Most deterministic radiative transfer models operate by first calculating the source term for scattering in a geographic region of interest (often a cone around the tangent point) and then find the observed radiance with one final line integration. Therefore, reducing the dimensionality of the source function alleviates a large computational burden.

The only available radiative transfer models which do not assume horizontal homogeneity are Monte Carlo models. Monte Carlo models solve the radiative transfer equation in a probabilistic fashion, and are usually simpler to implement, leading to less assumptions. For reference, SASKTRAN takes approximately 1 s to perform the radiative transfer calculation for a single wavelength, and Monte Carlo models are orders of magnitude slower than this. It would be possible to use a Monte Carlo model for atmospheric tomography, however the computation burden limits the use to proof of concept studies.

Successive Orders of Scattering

The successive order of scattering technique is a common method to solve the radiative transfer equation. We begin by calculating the single scatter source function from Eq. (2.28) and labelling it as,

$$J^{(1)}(s, \hat{\Omega}) = k_{\text{scat}}(s) F_{\text{sun}} e^{-\tau(s,\text{sun})} p(\hat{\Omega}_{sun}, \hat{\Omega}_{out}), \tag{2.28}$$

which may be calculated at a single location and direction in the atmosphere through one line integral. Having an estimate for J, the radiance may be calculated, once again, for any location and direction in the atmosphere, through the radiative transfer equation,

$$I^{(1)}(\vec{r}_0, \hat{\Omega}) = I(s_{\text{end}}, \hat{\Omega}) e^{-\tau(0,s_{\text{end}})} + \int_{s_{\text{end}}}^{0} J^{(1)}(s, \hat{\Omega}) e^{-\tau(0,s)}\, ds. \tag{2.29}$$

This equation gives the portion of the radiance that has been directly scattered from the incident solar beam, as well as the radiance attenuated from the surface at the end of the line of sight.

Having the single scattered radiance, from Eq. (2.21) we can then calculate the source function for light that has been scattered twice in the atmosphere,

$$J_\lambda^{(2)}(s,\hat{\Omega}) = k_{\text{scat}}(s)\int_{4\pi} I^{(1)}(s,\hat{\Omega}')p(s,\hat{\Omega},\hat{\Omega}')\,d\hat{\Omega}'. \tag{2.30}$$

This new source function can then be used in the radiative transfer equation to calculate $I^{(2)}$, similar to before. The full process can be iterated in the chain,

$$J^{(1)} \Rightarrow I^{(1)} \Rightarrow J^{(2)} \Rightarrow I^{(2)} \Rightarrow J^{(3)} \Rightarrow I^{(3)} \Rightarrow \cdots, \tag{2.31}$$

to obtain $I^{(n)}$ for an arbitrary order of scatter n. The full radiance, accounting for all orders of scatter, is then,

$$I = \sum_{n=1}^{\infty} I^{(n)}. \tag{2.32}$$

The technique is analogous to the Neumann series solution of the integral radiative transfer equation with the solar irradiance as the "first guess". In principle the technique could be initialized with any reasonable value for J (or I), however under this framework the n^{th} term in the Neumann series has the semi-physical interpretation as light that has been scattered n times.

The challenges involved in implementing the successive orders of scattering technique in practice are primarily numerical and computational. The source function and the radiance are five dimensional quantities (four dimensional if horizontal homogeneity is assumed) and the discretization of these dimensions must be handled to balance accuracy and speed. A large number of line integrals must be calculated to go from the source function to the radiance, and the level of accuracy in this integration step must also be considered. There are also many opportunities to cache intermediate results, interpolation weights, etc., which can greatly speed up the computation at the cost of increased system memory usage. The successive orders of scattering method has been implemented by the SASKTRAN radiative transfer model (Bourassa et al., 2008), of which parts of this thesis work extends.

2.3.4 A Note on Polarization

The preceding sections assumed that electromagnetic radiation could be completely described by its radiance, or equivalently, intensity; however, a full description of radiation would re-

quire information on polarization. While polarization information is contained in the raw electromagnetic fields, it is impractical to propagate these quantities directly through radiative transfer. The most common way to handle polarization in atmospheric radiative transfer is through the Stokes vector. The Stokes vector is a four element vector defined as,

$$\mathbf{I} = \begin{pmatrix} I \\ Q \\ U \\ V \end{pmatrix}, \tag{2.33}$$

where the parameters are given by,

$$\begin{aligned} I &= |E_x|^2 + |E_y|^2 \\ Q &= |E_x|^2 - |E_y|^2 \\ U &= 2\mathrm{Re}(E_x E_y^*) \\ V &= -2\mathrm{Im}(E_x E_y^*), \end{aligned} \tag{2.34}$$

and E is the electric field propagating in the z direction. The values of Q, U, V depend on the orientation of the, often arbitrary, $(\hat{x}, \hat{y})$ basis.

The equations of radiative transfer are readily modified account for polarization using the Stokes vector. Everywhere the scalar radiance appears it must be replaced with the Stokes vector. In the general case, specie's cross sections and phase functions become 4×4 matrices rather than scalar quantities. If these quantities are calculated through classical electromagnetic theory it is not difficult to calculate the full matrices as the electromagnetic fields are directly available. However, scalar radiative transfer is often used as an approximation for practical/computational speed reasons.

There are RTMs, known as vector RTMs, that handle polarization using the Stokes formulation (e.g. Dueck et al., 2017; Loughman et al., 2015; Postylyakov, 2004; Rozanov et al., 2014; Spurr, 2006). Solar radiation is naturally unpolarized; however, polarization occurs through scattering in the atmosphere. Some instruments directly measure one polarization state of radiation rather than intensity (e.g. Elash et al., 2016), where correctly handling polarization is critical. Even if the instrument is not sensitive to polarization, multiple scattering, through coupling of off diagonal terms in the phase function matrix, can cause the

I component of the state vector to differ between scalar and vector calculations. However, this effect is generally small and many normalizations commonly used in retrieving atmospheric constituents from limb scatter measurements cancel the errors due to neglecting polarization.

2.4 Inverse Theory

The previous section, Section 2.3, dealt with the nature of limb scatter measurements and the simulation of such measurements with radiative transfer theory. However, the goal of limb based instrumentation is to obtain vertical profiles of an atmospheric quantity of interest. This section deals with the topic of converting radiance measurements to estimates of a quantity of interest, often called the atmospheric inverse problem. A formal statement of the problem is presented with an overview of commonly used methods. Special detail is given to the method of Rodgers (2000), commonly referred to as the optimal estimation method.

In Chapter 5 we have applied the optimal estimation method to perform a tomographic retrieval with measurements from the NASA OMPS-LP instrument. This chapter also provides an overview of specific challenges involved, from the point of view of the inverse problem, in performing a tomographic retrieval.

2.4.1 The Inverse Problem

The full measurement system may be written,

$$\vec{y} = \mathbf{f}(\vec{x}, \vec{b}) + \epsilon, \tag{2.35}$$

where $\vec{y}$ is a vector of measurements of length m, $\mathbf{f}$ is a function encapsulating the physics of the measurement, $\vec{x}$ is a vector of length n describing quantities of interest, $\vec{b}$ describes required ancillary information, and ϵ is measurement error. The quantity $\vec{x}$ is called the state vector, which represents the target of interest for the retrieval process. The inverse problem may be described as finding the best estimate of $\vec{x}$ for a given $\vec{y}$.

The forward function, $\mathbf{f}$, cannot be realized in practice and must be approximated with a forward model, $\mathbf{F}$. The forward model consists of two components, an instrument model and

a radiative transfer model. The instrument model describes the characteristics of the measurement instrument while the radiative transfer model approximates the observed physics. The input to the forward model is the state vector and a set of ancillary information.

Ancillary information is quantities that are necessary to use the forward model, but are not being retrieved. This includes constants such as the cross sections of various species, and geometry information, i.e. where the instrument is, where it is pointing, where the sun is, etc. If a retrieval operates in phases where first species 1 is retrieved, then species 2 is retrieved, then the result of the species 1 phase may be used as ancillary information for the species 2 phase. Very rarely can the ancillary information be known directly and best estimates, or approximations, must be used in most cases.

In real world retrievals the measurement also contains random error, ϵ. The probability distribution of the measurement noise can usually be characterized for a specific instrument and used to improve the retrieval. Since the measurements are random the retrieved target also has a degree of randomness associated with it. Either through linear theory or simulations the random error of the measurements can be propagated through the retrieval procedure to provide an estimate of the error on the state vector.

The Need for Regularization

For practical reasons the atmospheric inverse problem is fundamentally ill-posed. The quantity being retrieved is often intended to be a representation of a specific atmospheric quantity as a function of space, which, for all intents and purposes, is a continuous quantity. As any practical measurement system consists of a finite number of measurements there is not enough information available to obtain an exact, unique solution. Since the ill-posed inverse problem does not have a unique solution, approximations and/or prior information must be included to obtain a unique solution.

A necessary step to solve the inverse problem numerically is to discretize the state vector. Often the state vector represents the number density of a species of interest on a set of vertical levels in the atmosphere. One option to handle the ill-posed nature of the atmospheric inverse problem is to choose the amount of levels such that the number of measurements, m, is greater than the number of elements of the state vector, n. If $n < m$ the system is over-determined

and a choice must be made to find the solution. A common choice is to minimize the least squares difference between the measurements and the model, i.e., minimize the cost function,

$$\chi^2 = [\vec{y} - \mathbf{F}(\vec{x})]^T [\vec{y} - \mathbf{F}(\vec{x})]. \tag{2.36}$$

In the linear case the minimization may be done directly, and in the non-linear case any number of iterative techniques can be used to find the minimum.

While the combination of discretization and the ordinary least squares solution does provide a mechanism for obtaining a solution to the originally ill-posed problem, there are difficulties with characterizing the solution. The bias and variance of the retrieval may be estimated; however, these estimates refer to the discretized state vector and not the true atmospheric state. A discretization that is too coarse may also necessarily result in a loss of information in the final retrieval. It is not typically possible to directly estimate what effect discretizing the state vector has on the overall inversion process.

Instead of handling the ill-posed nature of the inverse problem through coarse discretization, it is possible introduce additional information to the system through the use of an a priori constraint. Here, the state vector is discretized on a fine enough grid that the effect of the discretization is assumed to be negligible compared to other effects of the overall observing system. The next sections deal with how a priori information, or regularization, can formally be included into the retrieval and how the overall bias and variance can be estimated.

2.4.2 The Bayesian Solution to the Inverse Problem

One of the foundational inverse methods uses Bayesian statistics and is referred to as optimal estimation by Rodgers (2000). Bayes' theorem states,

$$P(\vec{x}\,|\vec{y}) = \frac{P(\vec{y}\,|\vec{x})P(\vec{x})}{P(\vec{y})}, \tag{2.37}$$

where $P(A|B)$ indicates the probability of A given B. The posterior distribution, $P(\vec{x}\,|\vec{y})$, is the desired solution to the inverse problem. Knowing the posterior distribution it is possible to calculate either the Maximum a Posteriori (MAP) solution at the maximum of $P(\vec{x}\,|\vec{y})$, or the expected value solution at the expected value of $P(\vec{x}\,|\vec{y})$. The MAP solution and

the expected value solution will be the same in the special case of a unimodal, symmetric posterior distribution. The probability of the measurement occurring, $P(\vec{y})$, is constant and can be neglected as it only serves as a normalization factor for the solution. The probability of the measurement given the state, or the *likelihood*, $P(\vec{y}\,|\vec{x})$, is often assumed to be Gaussian with covariance $\mathbf{S}_y$ and written,

$$P(\vec{y}\,|\vec{x}) \sim \exp\left\{-[\vec{y} - \mathbf{F}(\vec{x})]^T \mathbf{S}_y^{-1} [\vec{y} - \mathbf{F}(\vec{x})]\right\}, \tag{2.38}$$

where the symbol $\sim$ specifies that the relation holds up to to a multiplicative constant. The normality of the likelihood is supported by the fact that experimental errors tend to be well approximated as normal through the central limit theorem.

To demonstrate the relationship between the Bayesian interpretation and the least squares solution of Eq. (2.36), consider the case where $P(\vec{x}) \sim 1$. Then,

$$\log P(\vec{x}\,|\vec{y}) = -[\vec{y} - \mathbf{F}(\vec{x})]^T \mathbf{S}_y^{-1} [\vec{y} - \mathbf{F}(\vec{x})] + \text{constant}. \tag{2.39}$$

In this case the least squares solution is equivalent to maximizing the likelihood of the state vector weighted by the measurement covariance, which is known as the Maximal Likelihood solution. To reiterate, the classical least squares solution is equivalent to assuming the measurements are normally distributed and that all prior states are equally probable.

Often it is possible to include a better estimate of the prior state in the form of a probability distribution. In this case the posterior distribution can be formally evaluated through Eq. (2.37), however this requires evaluating the likelihood at all values supported by $P(\vec{x})$. Even with efficient sampling algorithms such as Markov Chain Monte Carlo (MCMC) it is not possible to evaluate the posterior distribution for more than a few trial cases. MCMC methods have been explored for use in validation purposes (e.g. Tamminen and Kyrölä, 2001).

The standard approximation made to evaluate the posterior distribution is that the prior distribution is well modelled by a normal distribution with mean $\vec{x}_a$, and associated covariance $\mathbf{S}_a$. Then, the prior distribution may be written,

$$P(\vec{x}) \sim \exp[-(\vec{x} - \vec{x}_a)^T \mathbf{S}_a^{-1} (\vec{x} - \vec{x}_a)]. \tag{2.40}$$

The assumption of normality is convenient in terms of the algebra involved, however it can be shown that if only the mean and variance of a quantity are specified then the maximal entropy

distribution is Gaussian (Dowson and Wragg, 1973). Applying Bayes' theorem results in,

$$-\log P(\vec{x}\,|\vec{y}) = [\vec{y} - \mathbf{F}(\vec{x})]^T \mathbf{S}_y^{-1} [\vec{y} - \mathbf{F}(\vec{x})] + (\vec{x} - \vec{x}_a)^T \mathbf{S}_a^{-1} (\vec{x} - \vec{x}_a) + \text{constant}. \tag{2.41}$$

The MAP solution of this problem can be computed by minimizing the cost function,

$$\chi^2 = [\vec{y} - \mathbf{F}(\vec{x})]^T \mathbf{S}_y^{-1} [\vec{y} - \mathbf{F}(\vec{x})] + (\vec{x} - \vec{x}_a)^T \mathbf{S}_a^{-1} (\vec{x} - \vec{x}_a), \tag{2.42}$$

which resembles the regular least squares cost function with an additional penalty or regularization term. The method can be interpreted as a form of Tikhonov regularization (Tikhonov, 1943) and is commonly used in the domains of statistics and machine learning.

Linearization

In the case that the forward model is linear, $\mathbf{F}(\vec{x}) = \mathbf{K}\vec{x}$, the Bayesian solution of Eq. (2.41) reduces to a single Gaussian,

$$-\log P(\vec{x}\,|\vec{y}) = (\vec{x} - \hat{\vec{x}})^T \hat{\mathbf{S}}^{-1} (\vec{x} - \hat{\vec{x}}) + \text{constant}, \tag{2.43}$$

where the MAP solution, $\hat{\vec{x}}$, is,

$$\hat{\vec{x}} = \vec{x}_a + (\mathbf{K}^T \mathbf{S}_y^{-1} \mathbf{K} + \mathbf{S}_a^{-1})^{-1} \left[\mathbf{K}^T \mathbf{S}_y^{-1} (\vec{y} - \mathbf{K}\vec{x}_a)\right], \tag{2.44}$$

with associated covariance,

$$\hat{\mathbf{S}} = (\mathbf{K}^T \mathbf{S}_y^{-1} \mathbf{K} + \mathbf{S}_a^{-1})^{-1}. \tag{2.45}$$

While we know from Section 2.3 that the forward model is not linear, the atmospheric inverse problem is usually not so non-linear that it can be solved with iterative linear methods. The forward model may be expanded around a state, $\vec{x}_l$, as,

$$\mathbf{F}(\vec{x}) = \vec{x}_l + \mathbf{K}(\vec{x} - \vec{x}_l), \tag{2.46}$$

where $\mathbf{K}$ is now the Jacobian matrix defined as,

$$\mathbf{K} = \frac{\partial \mathbf{F}(\vec{x})}{\partial \vec{x}}, \tag{2.47}$$

evaluated at $\vec{x} = \vec{x}_l$. Substituting the expanded forward model into Eq. (2.41) and solving for the mean and covariance of the resulting Gaussian distribution gives,

$$\hat{\vec{x}} = \vec{x}_l + (\mathbf{K}^T \mathbf{S}_y^{-1} \mathbf{K} + \mathbf{S}_a^{-1})^{-1} \left[\mathbf{K}^T \mathbf{S}_y^{-1} (\vec{y} - \mathbf{F}(\vec{x}_l)) - \mathbf{S}_a^{-1} (\vec{x}_l - \vec{x}_a)\right], \tag{2.48}$$

with an identical covariance as Eq. (2.45). Repeatedly linearizing around the current state, $\vec{x}_i$, to find the next state, $\vec{x}_{i+1}$, gives the iterative procedure,

$$\vec{x}_{i+1} = \vec{x}_i + (\mathbf{K}^T\mathbf{S}_y^{-1}\mathbf{K} + \mathbf{S}_a^{-1})^{-1}\left[\mathbf{K}^T\mathbf{S}_y^{-1}(\vec{y} - \mathbf{F}(\vec{x}_i)) - \mathbf{S}_a^{-1}(\vec{x}_i - \vec{x}_a)\right]. \tag{2.49}$$

It can be shown that an identical equation arises from applying the Gauss-Newton minimization technique to Eq. (2.42). The Gauss-Newton method is derived by applying Newton's method to find the root of the gradient of the cost function, neglecting second order terms.

As the Gauss-Newton method approaches a solution, or equivalently as the retrieval becomes more linear in the range of the step size, the convergence of the Gauss-Newton method approaches quadratic. However, far from the solution where the problem may not necessarily be close to linear, the Gauss-Newton method has poor performance. The poor performance often manifests as a repeated overshooting of the true solution, and in some cases can even prevent convergence from being achieved. A solution to this problem was proposed by Levenberg (1944) which modifies the Gauss-Newton step,

$$\vec{x}_{i+1} = \vec{x}_i + (\mathbf{K}^T\mathbf{S}_y^{-1}\mathbf{K} + \mathbf{S}_a^{-1} + \gamma\mathbf{I})^{-1}\left[\mathbf{K}^T\mathbf{S}_y^{-1}(\vec{y} - \mathbf{F}(\vec{x}_i)) - \mathbf{S}_a^{-1}(\vec{x}_i - \vec{x}_a)\right], \tag{2.50}$$

where γ is a positive constant. For $\gamma = 0$ the iteration is standard Gauss-Newton, but for large values of γ the iterative step approaches that of gradient descent.

The optimal value of γ depends on how linear the problem is relative to the proposed Gauss-Newton step. For problems that are approximately linear, the Gauss-Newton method approaches quadratic convergence and a small value of γ is ideal. When the problem has a higher degree of non-linearity, a large value of γ is optimal to give preference to the more stable gradient descent step. Most optimization routines will update the value of γ every iteration taking advantage of the above ideas. If, after any iteration, the cost function decreases then the value of γ is decreased as the state is moving closer to the domain of linearity. Conversely if the cost function increases as a result of one iteration, the algorithm retreats one iteration and increases the value of γ to move to a more stable regime.

Marquardt (1963) proposed a modification of Levenberg's algorithm, where the damping term, $\gamma\mathbf{I}$, is replaced with, $\gamma\,\mathrm{diag}(\mathbf{K}^T\mathbf{S}_y^{-1}\mathbf{K})$. The full iteration is,

$$\vec{x}_{i+1} = \vec{x}_i + (\mathbf{K}^T\mathbf{S}_y^{-1}\mathbf{K} + \mathbf{S}_a^{-1} + \gamma\mathrm{diag}\,(\mathbf{K}^T\mathbf{S}_y^{-1}\mathbf{K}))^{-1}\left[\mathbf{K}^T\mathbf{S}_y^{-1}(\vec{y} - \mathbf{F}(\vec{x}_i)) - \mathbf{S}_a^{-1}(\vec{x}_i - \vec{x}_a)\right], \tag{2.51}$$

and is known as the Levenberg-Marquardt algorithm. Marquardt's modification takes into account that different elements of the state vector may have considerably different magnitudes, and thus should be scaled accordingly. The Levenberg-Marquardt algorithm can be seen as a primitive form of a trust region method, where the problem is problem is only trusted to be linearly approximated within a certain range.

Characterizing the Retrieval

The retrieval can be cast in the statistical framework of estimation theory. The process of going from $\vec{y}$ to $\hat{\vec{x}}$ is referred to as an *estimator* and $\hat{\vec{x}}$ is known as the *estimate*. An estimator is commonly characterized by its Mean Squared Error (MSE),

$$\mathrm{MSE}[\hat{\vec{x}}] = \mathrm{E}_{\{\vec{y}\}}[(\hat{\vec{x}} - \vec{x}_{\mathrm{true}})^T(\hat{\vec{x}} - \vec{x}_{\mathrm{true}})], \tag{2.52}$$

where $\vec{x}_{\mathrm{true}}$ is the true atmospheric state, and $\mathrm{E}_{\{\vec{y}\}}$ indicates expectation value over all possible measurement values. The MSE is a function of the true atmospheric state, which in the optimal estimation type retrieval is also assumed to be a random variable. Therefore the solution covariance of Eq. (2.45) is given by the expectation value of the MSE over the true atmospheric state,

$$\mathrm{E}_{\{\vec{x}_{\mathrm{true}}\}}[\mathrm{MSE}[\hat{\vec{x}}]] = \hat{\mathbf{S}}. \tag{2.53}$$

The MSE may be decomposed into bias and variance components,

$$\mathrm{MSE}[\hat{\vec{x}}] = \mathrm{var}(\hat{\vec{x}}) + B(\hat{\vec{x}})^T B(\hat{\vec{x}}), \tag{2.54}$$

where the variance is defined as,

$$\mathrm{var}(\hat{\vec{x}}) = \mathrm{E}_{\{\vec{y}\}}[(\hat{\vec{x}} - \mathrm{E}_{\{\vec{y}\}}[\hat{\vec{x}}])^T(\hat{\vec{x}} - \mathrm{E}_{\{\vec{y}\}}[\hat{\vec{x}}])], \tag{2.55}$$

and the bias is,

$$B(\hat{\vec{x}}) = \mathrm{E}_{\{\vec{y}\}}[\hat{\vec{x}}] - \vec{x}_{\mathrm{true}}. \tag{2.56}$$

Since the atmospheric inverse problem is often assumed to be sufficiently linear around the minimum to allow linear propagation of uncertainties, it is possible to estimate the variance with standard error propagation. The gain matrix, $\mathbf{G}$, is defined as,

$$\mathbf{G} = \frac{\partial \vec{y}}{\partial \hat{\vec{x}}}, \tag{2.57}$$

and can be evaluated for the linear case in Eq. (2.44) directly as,

$$\mathbf{G} = (\mathbf{K}^T\mathbf{S}_y^{-1}\mathbf{K} + \mathbf{S}_a^{-1})\mathbf{K}^T\mathbf{S}_y^{-1}. \tag{2.58}$$

Therefore, the variance, or as it is often referred to as, the covariance of the solution due to measurement noise, can be written,

$$\mathrm{var}(\hat{\vec{x}}) = \hat{\mathbf{S}}_{\mathrm{noise}} = \mathbf{G}\mathbf{S}_y\mathbf{G}^T, \tag{2.59}$$

which maps noise in the measurements directly to noise in the solution space and follows from standard linear error propagation.

The bias of the retrieval process is analyzed by evaluating the expected value of the estimator directly. The full retrieval process is written as,

$$\hat{\vec{x}} = R(\vec{y}, \mathbf{S}_y, \vec{x}_a, \mathbf{S}_a), \tag{2.60}$$

where R is a function defining the retrieval, e.g., an iterative process of Eq. (2.49). The bias of the retrieval can be calculated assuming there is no measurement error (zero variance), or equivalently, that $\mathrm{E}_{\{\vec{y}\}}[\hat{\vec{x}}] = \hat{\vec{x}}$. For a perfect forward model, $\vec{y} = \mathbf{F}(\vec{x}_{\mathrm{true}})$, linearizing the retrieval process about the true state gives,

$$\hat{\vec{x}} = R(\mathbf{F}(\vec{x}_a), \mathbf{S}_y, \vec{x}_a, \mathbf{S}_a) + \mathbf{A}(\vec{x}_{\mathrm{true}} - \vec{x}_a), \tag{2.61}$$

where

$$\mathbf{A} = \frac{\partial\hat{\vec{x}}}{\partial\vec{x}_{\mathrm{true}}}, \tag{2.62}$$

is known as the averaging kernel. For any well-behaved retrieval we must have,

$$R(\mathbf{F}(\vec{x}_a), \mathbf{S}_y, \vec{x}_a, \mathbf{S}_a) = \vec{x}_a, \tag{2.63}$$

thus,

$$\hat{\vec{x}} = \vec{x}_a + \mathbf{A}(\vec{x}_{\mathrm{true}} - \vec{x}_a), \tag{2.64}$$

or, expressing the estimate as a deviation from the true atmospheric state,

$$\hat{\vec{x}} - \vec{x}_{\mathrm{true}} = (\mathbf{A} - \mathbf{I})(\vec{x}_{\mathrm{true}} - \vec{x}_a), \tag{2.65}$$

which provides an expression for the bias of the retrieval.

If the averaging kernel is the identity matrix, then we have the relation $\hat{\vec{x}} = \vec{x}_{\text{true}}$ and the retrieval is said to be unbiased. From Eq. (2.64), when the averaging kernel differs from identity it acts as a smoothing operator. The averaging kernel for Eq. (2.44) can be calculated directly to obtain,

$$\mathbf{A} = (\mathbf{K}^T\mathbf{S}_y^{-1}\mathbf{K} + \mathbf{S}_a^{-1})^{-1}\mathbf{K}^T\mathbf{S}_y^{-1}\frac{\partial \mathbf{F}(\vec{x}_{\text{true}})}{\partial \vec{x}_{\text{true}}}. \tag{2.66}$$

It is common to assume that the Jacobian evaluated at the true atmospheric state is equal to the Jacobian evaluated at the final retrieved atmospheric state, reducing the averaging kernel to,

$$\mathbf{A} = (\mathbf{K}^T\mathbf{S}_y^{-1}\mathbf{K} + \mathbf{S}_a^{-1})^{-1}\mathbf{K}^T\mathbf{S}_y^{-1}\mathbf{K}. \tag{2.67}$$

If $\mathbf{S}_a^{-1} = 0$, indicating that no information is available about the a priori state, then the averaging kernel is the identity matrix (assuming $\mathbf{K}^T\mathbf{S}_y^{-1}\mathbf{K}$ is invertible).

Calculating the bias requires knowing the true atmospheric state; however, the statistics of the bias may be estimated. For an ensemble of retrievals where the true state is assumed to be described by a Gaussian prior distribution with covariance $\mathbf{S}_a$ and expectation value $\vec{x}_a$,

$$\mathrm{E}_{\{\vec{x}_{\text{true}}\}}[B(\vec{x})^T B(\vec{x})] = (\mathbf{A} - \mathbf{I})^T\mathbf{S}_a(\mathbf{A} - \mathbf{I}). \tag{2.68}$$

This term is often referred to as the smoothing error, and is donated as $\hat{\mathbf{S}}_{\text{smooth}}$. A simple calculation verifies that $\hat{\mathbf{S}} = \hat{\mathbf{S}}_{\text{noise}} + \hat{\mathbf{S}}_{\text{smooth}}$. If the averaging kernel is identity, i.e. the retrieval is unregularized, then the smoothing error reduces to zero. The smoothing error attempts to quantify the effect the averaging kernel has on the retrieved state. However, for the smoothing error to be meaningful $\mathbf{S}_a$ has to be an accurate measure of the covariance of the true atmosphere, which is rarely the case in practical retrievals (Von Clarmann, 2014). For this reason smoothing error is often not included in the final precision estimate of most retrieval systems.

In evaluating the bias of the retrieval we assumed that the forward model was perfect, which is clearly not the case in reality. Errors related to the forward model can be split into two categories: errors due to an imperfect model and errors due to imperfect knowledge of the auxillary parameters. Imperfect forward model errors can be difficult to identify, much less evaluate. In some cases a potential error can be identified, e.g. imperfect treatment

of clouds in the forward model, but there is no standard method to estimate its effect on the overall inverse process. Only in special cases can these forward model errors actually be evaluated. One example could be if the forward model is capable of handling polarization, the effect of neglecting polarization could be estimated by comparing retrieval results with and without polarization enabled.

Forward model parameter errors are also not possible to evaluate in many cases. In the special cases that a parameter, b, has a known covariance, $\mathbf{S}_b$, then the covariance of the solution due to the parameter is,

$$\hat{\mathbf{S}}_b = \mathbf{G}\mathbf{K}_b\mathbf{S}_b\mathbf{K}_b^T\mathbf{G}^T, \tag{2.69}$$

where,

$$\mathbf{K}_b = \frac{\partial \mathbf{F}}{\partial b}, \tag{2.70}$$

which follows from standard linear error propagation. However in most cases it is easier to directly perturb b and repeat the retrieval process to estimate the effect, rather than calculate $\mathbf{K}_b$.

2.4.3 Challenges for Tomography

The final goal of the thesis is to perform a two-dimensional retrieval using limb scatter measurements from OMPS-LP. While the theory presented in this chapter is general and applies equally to a two-dimensional retrieval, there are several specific challenges that should be mentioned. For a standard, one-dimensional retrieval, the state vector might represent a vertical profile of a single species in the atmosphere, having on the order of $\sim$100 elements. The measurement vector would be all the relevant measurements from a single vertical scan, or vertical image, and using a modest 10 wavelengths could be on the order of $\sim$1 000 elements. When switching to a two-dimensional retrieval, both of these vectors are orders of magnitude larger.

For a two-dimensional retrieval, the horizontal dimension typically has around 100 grid points (the OMPS-LP retrieval performed later has $\sim$160). Therefore the state vector is on the order of $\sim$10 000 elements, and the measurement vector is on the order of $\sim$100 000 elements. Handling these individually is not an issue; however it becomes challenging to both

calculate and store the $100\,000 \times 10\,000$ Jacobian matrix. In one-dimensional retrievals it is possible to calculate the Jacobian matrix using perturbation methods, perhaps using some approximations such as in **kaiser2003**. In the two-dimensional retrieval this quickly becomes computationally unfeasible and other methods need to be explored. Chapter 4 describes the solution that was developed to approximate the Jacobian matrix using closed form techniques rather than perturbation methods.

Chapter 3

High-resolution and Monte Carlo Additions to the SASKTRAN Radiative Transfer Model

D. J. Zawada, S. R. Dueck, L. A. Rieger, A. E. Bourassa, N. D. Lloyd, D. A. Degenstein

As previously discussed, one of the major challenges in developing a two-dimensional retrieval for limb scatter measurements is the additional complications involved for the forward model. This manuscript outlines modifications made to the original SASKTRAN radiative transfer model (Bourassa et al., 2008) in the interest of performing tomographic retrievals. The newly developed model, SASKTRAN-HR (HR), is also compared to a reference monte carlo model to evaluate its performance. Lastly, the capabilities of HR are demonstrated by quantifying and suggesting a possible fix for biases present due to radiative transfer model capabilities in the OSIRIS v5.07 ozone data product (Degenstein et al., 2009).

While the primary purpose of the manuscript was to develop a model for future tomographic retrievals, it has been used in a variety of projects. Sioris et al. (2017) used the HR model to include diurnal variations along the OSIRIS line of sight for the retrieval of stratospheric NO_2. Dueck et al. (2017) has extended the model to include the effects of polarization, which was then used to retrieve stratospheric aerosol from ALI measurements (Elash et al., 2016; Elash et al., 2017). The added adaptive integration feature designed to help in optically thick scenarios has proven useful in modelling water vapor absorption features for the SHOW instrument (Langille et al., 2018). Currently HR has become the default recommended module in SASKTRAN, and was used in processing the most recent data products from the OSIRIS mission (Bourassa et al., 2018).

The HR engine presented in the manuscript was developed primarily by myself, while the Monte Carlo engine was developed by S. R. Dueck. The majority of the manuscript was

written by myself, with the exception of the Monte Carlo section which was written by S. R. Dueck. The analysis of the OSIRIS data was performed jointly by myself, S. R. Dueck, and L. A. Rieger.

This manuscript has been published in Atmospheric Measurement Techniques, and unless otherwise stated the version presented here is unchanged. The layout of figures and equations and the format of cross references has been modified to match that of the overall document.

Zawada, D. J., Dueck, S. R., Rieger, L. A., Bourassa, A. E., Lloyd, N. D., & Degenstein, D. A. (2015). High-resolution and Monte Carlo additions to the SASKTRAN radiative transfer model. *Atmos. Meas. Tech. 8*(6), 2609–2623. doi:10.5194/amt-8-2609-2015

3.1 Abstract

The Optical Spectrograph and InfraRed Imaging System (OSIRIS) instrument on board the Odin spacecraft has been measuring limb-scattered radiance since 2001. The vertical radiance profiles measured as the instrument nods are inverted, with the aid of the SASKTRAN radiative transfer model, to obtain vertical profiles of trace atmospheric constituents. Here we describe two newly developed modes of the SASKTRAN radiative transfer model: a high-spatial-resolution mode and a Monte Carlo mode. The high-spatial-resolution mode is a successive-orders model capable of modelling the multiply scattered radiance when the atmosphere is not spherically symmetric; the Monte Carlo mode is intended for use as a highly accurate reference model. It is shown that the two models agree in a wide variety of solar conditions to within 0.2 %. As an example case for both models, Odin–OSIRIS scans were simulated with the Monte Carlo model and retrieved using the high-resolution model. A systematic bias of up to 4 % in retrieved ozone number density between scans where the instrument is scanning up or scanning down was identified. The bias is largest when the sun is near the horizon and the solar scattering angle is far from 90°. It was found that calculating the multiply scattered diffuse field at five discrete solar zenith angles is sufficient to eliminate the bias for typical Odin–OSIRIS geometries.

3.2 Introduction

Remote sensing has played an integral role in our understanding and monitoring of Earth's atmosphere, notably in the study of ozone and the retrieval of vertically resolved atmospheric constituent profiles. Some of the first standard ozone profiles were retrieved using data from occultation instruments which provided high-quality, near-direct measurement of optical depth profiles. Although highly accurate, these instruments had limited sampling capabilities, generally measuring between 16 and 32 profiles per day. To help address this, several instruments that measure limb-scattered light in the ultraviolet (UV) to near infrared (NIR) have since been placed in orbit, including SCanning Imaging Absorption spectroMeter for Atmospheric CHartographY (SCIAMACHY) (Bovensmann et al., 1999), OSIRIS (Optical Spectrograph and InfraRed Imaging System; Llewellyn et al., 2004), and OMPS (Ozone Mapping and Profiler Suite; Rault and Loughman, 2013a).

While limb-scatter measurement provides greatly improved sampling rates, the signal interpretation is much more convoluted than for occultation measurements, owing to the complicated scattering paths of UV and visible light. Nevertheless, several successful retrieval algorithms have been implemented by the SCIAMACHY (Rozanov et al., 2007; Sonkaew et al., 2009; von Savigny et al., 2005), OMPS (Rault and Loughman, 2013a), and OSIRIS (Degenstein et al., 2009; Haley et al., 2004) data processing groups to retrieve ozone profiles using the Hartley–Huggins and Chappuis absorption bands. In addition, several other species have been retrieved including NO_2 (Bourassa et al., 2011), BrO (Rozanov et al., 2011a), and H_2O (Rozanov et al., 2011c). These retrievals rely heavily on the ability to accurately forward-model the radiance over a variety of solar illumination conditions, both over the course of an orbit and over the course of a single vertical scan. This is particularly important for retrievals, such as those listed above, which use a high-altitude normalization, as the local solar illumination condition varies with altitude and errors in modelling the diffuse radiance field leads to errors in the retrieved atmospheric constituents. While this effect is greater in scanning instruments such as SCIAMACHY and OSIRIS, it is still present to a lesser degree in imaging instruments such as OMPS. For forward modelling, OSIRIS retrievals have typically relied on SASKTRAN, a spherical, successive-orders radiative transfer model

(Bourassa et al., 2008).

This paper describes the addition of two new engines to the SASKTRAN framework which allow for Monte Carlo and high-spatial-resolution radiative transfer modelling. As an example of usage, systematic errors in the OSIRIS ozone retrieval due to low-resolution radiative transfer limitations are explored and results from model simulations are used to identify and improve treatment of problematic measurement conditions.

3.3 The Forward Model

3.3.1 The SASKTRAN Framework

The forward model used in this study is SASKTRAN. SASKTRAN is a radiative transfer framework consisting of two major components: a set of climatologies and optical properties which are used to specify the atmospheric state and an engine which solves the equation of radiative transfer for quantities of interest. Currently SASKTRAN consists of three separate engines: a standard successive-orders-of-scattering engine (SO), a high-spatial-resolution engine (HR), and a Monte Carlo engine (MC). All components of the SASKTRAN framework treat the planet and atmosphere as spherical, and all path lengths and angles are computed using a spherical geometry.

3.3.2 The Successive-Orders Engine

The original SASKTRAN radiative transfer model outlined in Bourassa et al. (2008) has been incorporated into the newly designed SASKTRAN framework. The successive-orders engine (SO) uses the successive-orders-of-scattering method to calculate the radiance field in a region of interest and closely resembles the original model in Bourassa et al. (2008). Here we provide a brief overview of the method.

The radiance can be written in integral form,

$$I(\vec{r}_0, \hat{\Omega}) = \int_{s_{\text{end}}}^{0} J(s) e^{-\tau(s,0)} \, \mathrm{d}s + I_{\text{end}}(s_{\text{end}}) e^{-\tau(s_{\text{end}},0)}, \tag{3.1}$$

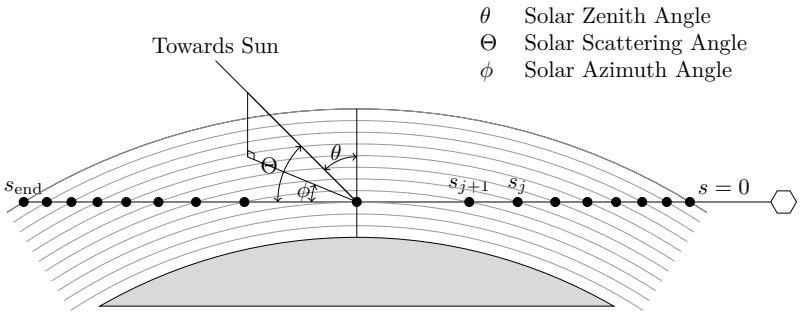

Figure 3.1: The limb-scatter geometry used in SO, HR, and MC. The solar viewing angles are defined at the tangent point.

where s is distance along a path implicitly defined by an $\vec{r}_0$ and $\hat{\Omega}$, J is the source function, I_{end} is the radiance at the end of the line of sight, and $\tau(s, 0)$ is the optical depth given by

$$\tau(s, 0) = \int_s^0 k(s)\, \mathrm{d}s, \tag{3.2}$$

where k is the extinction. Here we have followed the convention used in Bourassa et al. (2008) that s is 0 at the observer location and negative at the end point s_{end} (see Fig. 3.1). In general, the source function depends on position in the atmosphere and a local look direction, making it a five-dimensional field. In the UV to NIR region, the source function consists of scattering alone and is given by

$$J(s, \hat{\Omega}) = k_{\text{scat}}(s) \int_{4\pi} I(s, \hat{\Omega}')\overline{p}(s, \hat{\Omega}', \hat{\Omega})\, \mathrm{d}\hat{\Omega}', \tag{3.3}$$

where k_{scat} is the scattering extinction, $\overline{p}$ is the normalized phase function, and the integral is over the unit sphere.

The radiance is calculated with the successive-orders-of-scattering method. Ignoring the discretization that needs to be done in a real model, the technique has an intuitive explanation beginning with the incoming solar irradiance. Solar rays are attenuated to all points in the atmosphere and scattered, forming the source function for light that has been scattered once. The scattered rays are then propagated through the atmosphere and, once again, scattered at all points, forming the source function for light that has been scattered twice. The process can then be repeated to find the source function for light that has been scattered to an arbitrary order. Mathematically we are applying Eqs. (3.1) and (3.3) iteratively until convergence is achieved. The ground surface is assumed to be Lambertian and is handled through the I_{end}

term in Eq. (3.1). For most wavelengths the source term becomes negligibly small (for limb-scatter retrievals) after 10 orders of scatter. More orders of scatter are required for strict convergence of the observed radiance in the 350–500 nm window, however, where Rayleigh scattering is strong and there is little absorption.

Once the full source function is known, the radiance for a specific line of sight can be calculated through a relatively simple line integral. We approximate the line integral by splitting the ray into segments where the extinction and source function are assumed to be constant. We call these segments *cells*. The successive-orders model finds the cell boundaries by calculating intersections of the line of sight with a set of spherical shells (Fig. 3.1), which by default are spaced uniformly in altitude with a separation of 1 km but can be placed on any user defined grid. An additional cell boundary is added at the tangent point to ensure that the start and end of a cell are not at the same altitude.

To perform the actual calculation of the source term, the integral in Eq. (3.3) must be discretized. If atmospheric properties are invariant with respect to rotation about the solar direction, then the diffuse radiation field is a function of altitude, solar zenith angle, and local look direction. This reduces the iterative integral from five dimensions to four. Fineness of the discretization of solar zenith angle is of particular importance when balancing accuracy with execution speed. We call the diffuse field calculated for a discrete set of local look directions and altitudes above a geographic location a *diffuse profile*. This is specified at a set of *diffuse points* at discrete altitudes and *diffuse incoming* and *outgoing rays* originating from each point at which the field is calculated in discrete directions. The lowest point on every diffuse profile is placed on the ground and handles the surface contributions to higher orders of scatter. Incoming and outgoing rays simply represent the discretization of Eq. (3.3) inside the engine. Accurate simulation of observed radiance requires more diffuse profiles when the line of sight spans a large gradient in solar zenith angle or when the tangent point is near the terminator. A limited study of the number of required diffuse profiles to achieve a precision of 0.2 % for extreme conditions is done in Sect. 3.3.5. When performing the final radiance line integral, source terms from diffuse profiles are interpolated linearly in solar zenith angle; interpolation between points is linear in altitude, and interpolation between diffuse rays is bilinear on the triangle that bounds a query point or direction on a unit sphere.

Previously, SO would approximate the diffuse field by assuming the diffuse profiles are uncoupled. For example, when calculating the third-order-of-scatter source term a diffuse profile uses only its own second-order source term, rather than coupling to other profiles. The approximation affects the third and higher orders of scatter, and is thus small at many wavelengths, but can be significant in certain conditions, for example, near 350 nm looking across the terminator. This approximation has since been lifted, fully coupling diffuse profiles together. It should be noted that the coupling does not change the theoretical basis of the algorithm, as diffuse profiles were initially uncoupled only for ease of implementation. The coupling of diffuse profiles causes the model to use a large amount of RAM, approximately 700 MB for each diffuse profile.

3.3.3 The High-Resolution Engine

A new high-spatial-resolution engine under the SASKTRAN radiative transfer framework has been developed. The engine is intended for use in future satellite missions requiring higher detail in the radiative transfer calculation. The radiative transfer equation is solved in the same fashion as SO, but less information is cached for each wavelength. The reduction in caching causes HR to use approximately one-seventh the RAM in identical configurations, at the expense of increased execution time.

Lower memory usage allows for higher-accuracy computations in both the single-scattered and diffuse radiation fields. In addition, several new features have been implemented:

- the ability to handle areas of large or highly variable extinction (e.g. cirrus clouds, see Wiensz et al. (2013) for information about specifying subvisual cirrus in SASKTRAN) through adaptive cell splitting;

- support for atmospheric constituents which vary in two or three dimensions, e.g. latitude and longitude, rather than exclusively in altitude;

- weighting functions for absorbing species can be approximated analytically in one and two dimensions for little computational cost.

Numerical Integration Improvements

Line integrals must be performed in two different areas when performing the successive-orders method: the calculation of optical depth and the integration of source terms along a path. Optical depth is calculated as in Loughman et al. (2015), where extinction is allowed to vary linearly in altitude within each cell. The integration of source terms requires the definition of both optical depth and extinction as functions of distance along a ray. The total optical depth for a ray is simply the sum of the optical depth for each cell individually. For a single cell,

$$\tau(s_{j+1}, s_j) = \int_{s_{j+1}}^{s_j} k(s)\,\mathrm{d}s \approx \int_{h(s_{j+1})}^{h(s_j)} (k_0 + k_h h)\frac{\mathrm{d}h}{\mathrm{d}s}\mathrm{d}s, \tag{3.4}$$

where $\tau(s_{j+1}, s_j)$ is the optical depth for cell j, $k(s)$ and $h(s)$ are the extinction and altitude as a function of path length respectively, and k_0 and k_h are constants determined by values of $k(s)$ on the cell boundary. From Eq. (3.4) we define an effective extinction, $\tilde{k}_j$, for the cell j:

$$\tilde{k}_j = \frac{\tau(s_{j+1}, s_j)}{\Delta s_j}, \tag{3.5}$$

where $\Delta s_j = |s_{j+1} - s_j|$ is the distance from the start (s_j) to the end of the cell (s_{j+1}).

When the extinction varies significantly between s_1 and s_2, $\tilde{k}_j$ becomes a poor representation of the atmospheric state. To improve the representation of extinction along a ray, HR adds the capability to split cells when the ratio of total extinction between the start and end of a cell,

$$\frac{\min(k(s_j), k(s_{j+1}))}{\max(k(s_j), k(s_{j+1}))}, \tag{3.6}$$

is less than a user-specified value (typically on the order of 0.95). This condition by itself can cause excessive splitting near the top of the atmosphere where the extinction is small but highly variable. Therefore, an additional condition is added that the optical depth of the cell must be greater than another user-specified value (typically 0.01) for the splitting to occur.

The radiance along a specific line of sight as a result of atmospheric scattering may be written as the sum of radiance contributions from individual cells attenuated back to the

observer,

$$I = \sum_{j=1}^{N} e^{-\tau(s_j,0)} I_j, \tag{3.7}$$

where I is the radiance seen by the observer, $\tau(s_j, 0)$ is the optical depth from the observer to the start of cell j, and I_j is the radiance at the start of the cell due to sources within the cell. The quantity I_j may be written

$$I_j = \int_{s_{j+1}}^{s_j} e^{-k(s)(s-s_j)} J(s)\,\mathrm{d}s, \tag{3.8}$$

where $J(s)$ is the source function. SO computes this integral by evaluating $k(s)$ and $J(s)$ at the cell midpoint and performing the integral

$$I_j = J(s_\mathrm{m}) \left(\frac{1 - e^{-k(s_\mathrm{m})\Delta s_j}}{k(s_\mathrm{m})} \right), \tag{3.9}$$

where $s_\mathrm{m} = (s_j + s_{j+1})/2$. The HR mode improves this computation by letting $J(s)$ be a quadratic function in $(s - s_j)$ while keeping $k(s)$ constant. The constant value of $k(s)$ is chosen as the effective value of the extinction across the cell, $\tilde{k}_j$, defined in Eq. (3.5). Note that the cell-splitting procedure outlined removes conditions where the assumption of constant $k(s)$ is poor. The source function, $J(s)$, is computed as the Lagrange interpolating polynomial through the start, middle, and end points of the cell. Similar techniques are used in Olson and Kunasz (1987) and Griffioen and Oikarinen (2000). By writing $J(s) = \alpha_j + \beta_j(s - s_j) + \gamma_j(s - s_j)^2$ for one cell j, the integral in Eq. (3.8) can be explicitly evaluated to obtain

$$\begin{aligned} I_j = \quad & \alpha_j \left[\frac{1 - e^{-\tilde{k}_j \Delta s_j}}{\tilde{k}_j} \right] \\ & + \beta_j \left[\frac{1 - e^{-\tilde{k}_j \Delta s_j}(1 + \tilde{k}_j \Delta s_j)}{\tilde{k}_j^2} \right] \\ & + \gamma_j \left[\frac{2 + e^{-\tilde{k}_j \Delta s_j}(-2 - \tilde{k}_j \Delta s_j (2 + \tilde{k}_j \Delta s_j))}{\tilde{k}_j^3} \right], \end{aligned} \tag{3.10}$$

where the Lagrange coefficients $\alpha_j, \beta_j, \gamma_j$ are given by

$$\begin{aligned}
\alpha_j &= J(s_j) \\
\beta_j &= \frac{-3J(s_j) + 4J(s_\mathrm{m}) - J(s_{j+1})}{\Delta s} \\
\gamma_j &= \frac{2J(s_j) - 4J(s_\mathrm{m}) + 2J(s_{j+1})}{\Delta s^2}.
\end{aligned} \tag{3.11}$$

Terms of the form $1 - \exp\left(-\tilde{k}_j \Delta s_j\right)$ when $\tilde{k}_j \Delta s_j \ll 1$ are evaluated through a Taylor series approximation to avoid issues with numerical precision.

Two- and Three-Dimensional Atmospheres

Support has been added in HR mode for the atmospheric constituents to vary in two or three dimensions. There are two main complications in breaking the assumption of horizontal homogeneity. First, the diffuse field now varies in an additional dimension; second, the line integration techniques need to be modified to deal with an additional dimension in which quantities may vary.

To account for the now five-dimensional diffuse field, diffuse profiles are not limited to placement at discrete solar zenith angles. Interpolation of the source function between diffuse profiles is done by finding the nearest three diffuse profiles and performing linear interpolation using the vertices of the formed triangle.

For a limb geometry measurement, simply finding intersections with a set of spherical shells, as is done in SO, causes cells near the tangent point to have lengths of up to 100 times the vertical spacing (usually 1 km). To combat this, the HR mode enhances the ray tracing stage by finding intersections with a list of arbitrary geometry primitives (e.g. spheres, cones, planes). The list of primitives used depends on the mode in which the model is operating. For a one-dimensional atmosphere the list consists of a set of spheres, replicating SO.

There are three primary modes where the HR model supports variation of atmospheric constituents in more than one dimension. The first is the fully three-dimensional mode, wherein atmosphere is allowed to vary arbitrarily. Internally, the atmosphere is stored as a set of vertical profiles, specified above discrete geographic locations. For HR it is sufficient (and desirable, for time efficiency) to specify the atmosphere only on a region slightly larger than that where the diffuse field is to be solved. The Delaunay triangulation on a sphere of

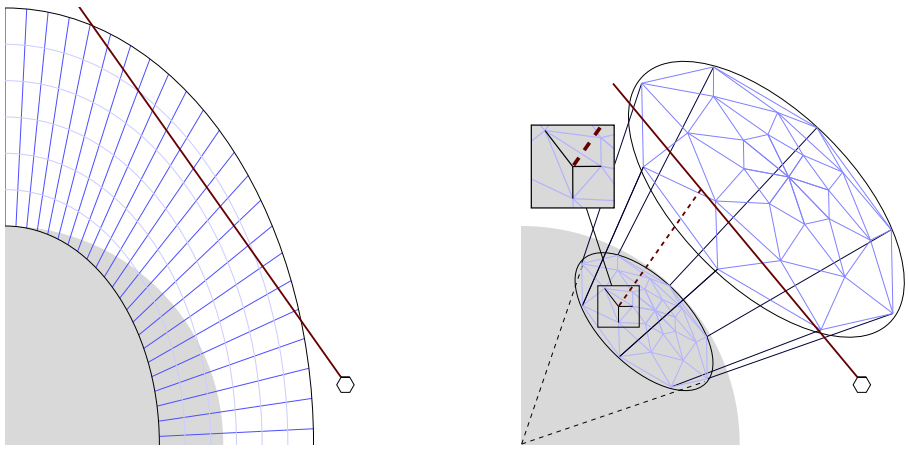

Figure 3.2: The two- and three-dimensional atmospheric grids used in HR. **(a)** A grid is shown consisting of altitude and angle along the line of sight direction, however, the plane can be placed in any direction (latitude, solar zenith angle, etc.). **(b)** The Delaunay grid used for three-dimensional atmospheres. The barycentric interpolation on the surface of the Earth is also shown.

atmospheric profile locations is found, and queries of the atmospheric state are answered by interpolating between the three profiles which, when their locations are joined by geodesics to form a spherical triangle, bound the query point (Delaunay, 1934). The grid is conceptually shown in Fig. 3.2b. Calculating the points along the ray at which the bounding Delaunay triangle changes is computationally intensive, so for ray tracing purposes we approximate the grid by the intersections of a set of cones and planes. Successively larger ray tracing concentric cones are placed at the tangent point; planes containing the tangent point and centre of the Earth with various azimuth angles are also added.

For satellite tomography applications, a second mode is implemented where the atmosphere varies in the orbital plane, i.e. in altitude and in angle along the orbit track (Fig. 3.2a). The ray tracing primitives added in addition to the spherical shells are planes perpendicular to the orbit plane and passing through the centre of the Earth. These guarantee that variations in optical properties along the orbit plane are resolved even when sphere intersections are sparse.

As previously stated, the assumption of horizontal atmospheric homogeneity leads to the simplification that the diffuse field does not vary in solar azimuth. This simplification also holds when atmospheric constituents are allowed to vary in solar zenith angle as well

as altitude. This special case is particularly useful for the inclusion of photochemically active species. Here, diffuse profiles can be placed once again in solar zenith angle without compromising the accuracy of the solution. To account for the additional variation in the numerical integration, cones of constant solar zenith angle are added to the ray tracing primitives list.

Analytical Weighting Functions

The HR model adds the capability to calculate weighting functions (derivatives of radiance with respect to atmospheric parameters) analytically with little computational overhead. Fast calculation of weighting functions is necessary for many retrieval algorithms. One method to compute the weighting functions is through finite-difference schemes, which requires the forward model to be run a second time with an atmospheric parameter slightly perturbed. Often when calculating weighting functions the forward model is run for single-scattering only to save on execution time. The single-scattering approximation was shown to produce weighting functions sufficient for use in O_3 and NO_2 retrievals in Kaiser and Burrows (2003).

Here we present a simple method for analytical computation of weighting functions which is fast, is more accurate than the single-scattering approximation, and extends naturally to two- and three-dimensional atmospheres. We start by taking the derivative of Eq. (3.7),

$$w(x) \stackrel{\text{def}}{=} \frac{\partial I}{\partial x} = \sum_{j=1}^{N} e^{-\tau(s_j,0)} \left(\frac{\partial I_j}{\partial x} - \frac{\partial \tau(s_j,0)}{\partial x} I_j \right), \tag{3.12}$$

or using the formulae for I_j and $\tau(s_j, 0)$,

$$\begin{aligned} w(x) = \sum_{j=1}^{N} \Bigg[& - \int_{s_{j+1}}^{s_j} s \frac{\partial k(s)}{\partial x} e^{-k(s)(s-s_j)} J(s)\, \mathrm{d}s \\ & + \int_{s_{j+1}}^{s_j} e^{-k(s)(s-s_j)} \frac{\partial J(s)}{\partial x}\, \mathrm{d}s \\ & - I_j \int_{s_j}^{0} \frac{\partial k(s)}{\partial x} \mathrm{d}s \Bigg]. \end{aligned} \tag{3.13}$$

The first and second terms in the sum represent changes to the radiance contribution from specific cells, while the third term is the added attenuation. By adding ray tracing primitives which bound the perturbation ∂x, the integrals in the first and third terms can be performed

(assuming we know $\partial k(s)/\partial x$) using the techniques described in Sect. 3.3.3. The second term is expensive to calculate exactly and depends on the nature of ∂x.

For absorbing species, i.e. $x = k_{\text{abs}}$, we approximate $\partial J(s)/\partial k_{\text{abs}}$ by only computing changes to the first-order-of-scattering source term, $J_1(s)$, analytically. The first-order source term is light scattered directly from the sun; thus a change in absorbing species can only affect the solar transmission (the optical depth from the sun to the scattering point), and therefore

$$\frac{\partial J_1(s)}{\partial x} = -J_1(s)\frac{\partial \tau_{\text{sun}}}{\partial x}. \tag{3.14}$$

In spherically symmetric atmospheres the change in the higher-orders-of-scattering source term may be approximated by assuming the incoming radiance to a point in the atmosphere is constant below the local horizon and zero above. Then the derivative of the multiply scattered source term, $\partial J_{\text{ms}}/\partial k_{\text{abs}}$, is equal to the average slant extinction. The final weighting function may then be calculated using Eq. (3.13) and the same numerical integration techniques already within the model. The weighting functions for number density of a specific absorbing species can then be found by multiplying by that species' absorption cross section.

As an example, weighting functions for a typical ozone distribution were calculated for a line of sight with tangent altitude of 24.5 km and are shown in Fig. 3.3. Generally the analytical weighting functions agree with those calculated through the finite-difference method to within 2 % down to the peak value. Agreement below the peak value is worse. However, values below the peak have much less relevance to retrieval applications as they represent contributions from higher orders of scatter. In all cases the analytical weighting functions agree better than ones calculated with the single-scattering approximation. Calculation of the analytical weighting functions takes approximately one-fifth the time of a single radiative transfer calculation.

For a single-scattering species, $x = k_{i,\text{scat}}$, the scattering extinction of species i. Writing the normalized phase function of all species, $\overline{p}(s)$, as

$$\overline{p}(s) = \frac{\sum_i k_{i,\text{scat}}(s)\overline{p}_i}{k_{\text{scat}}(s)}, \tag{3.15}$$

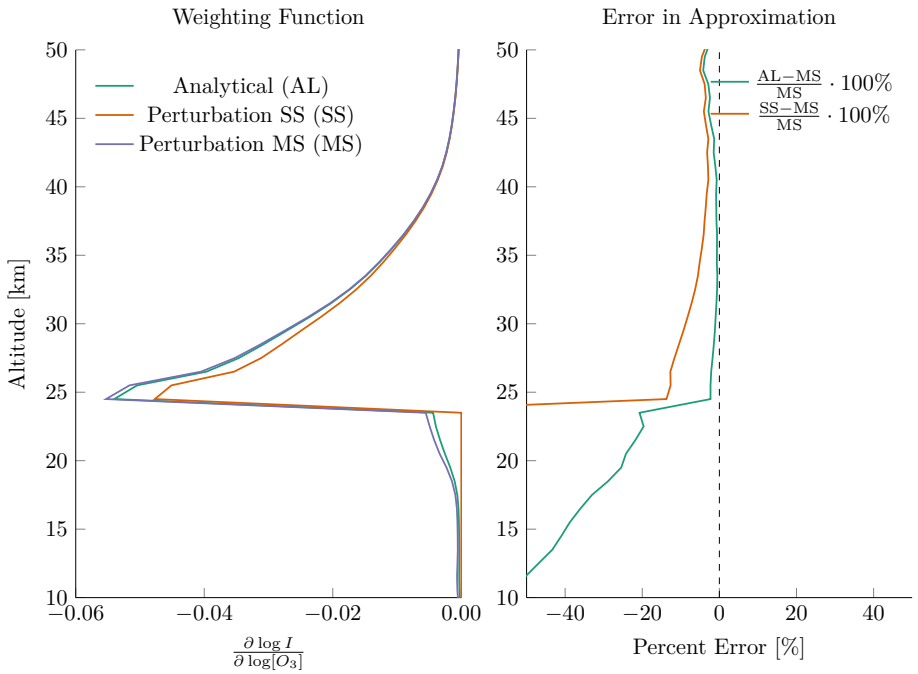

Figure 3.3: Ozone weighting functions at a wavelength of 330 nm for a line of sight with tangent altitude 24.5 km. Shown are the results for the analytical method (AL), the finite-difference method when single scattering is only considered (SS), and the finite-difference method when multiple scattering is included (MS). The right panel shows the error in the analytical and single-scattering methods compared to the multiple scattering method.

with $\overline{p}_i$ representing the phase function of species i, and taking the derivative yields

$$\frac{\partial J_1(s)}{\partial x} = J_1 \left[\frac{\omega_i(s)\overline{p}_i(s)}{k_{\text{scat}}(s)\overline{p}(s)} - \frac{\partial \tau_{\text{sun}}}{\partial x} \right], \tag{3.16}$$

where ω_i is the single scatter albedo of species i. Weighting functions for scattering species can then be found through the same line integration techniques described previously.

3.3.4 The Monte Carlo Engine

As shown in Bourassa et al. (2008), the successive-orders method is sensitive to the density (and implicitly the placement) of diffuse profiles and to the resolution of rays incoming and outgoing to diffuse points. In particular, where gradients in the diffuse radiance field are large many profiles are required to capture the horizontal diffusion of light, and where the field is highly non-isotropic a high resolution of incoming/outgoing rays is required to preserve detail ergodic to the phase function. Since the order-n diffuse field is used to compute the

order-$(n+1)$ field, any deficiencies in these resolutions or the interpolation schemes used in HR are necessarily compounded and amplified in the higher-order diffuse field. Diagnosis of such errors by comparison of the output of HR to that of other models is difficult, as support for various optical property and climatological species libraries is not common across models. Furthermore, the method used to solve the radiative transfer problem varies greatly from model to model, and each implementation is sensitive to computational limits in its own way.

It is desired, therefore, to test the discrete-ordinates successive-orders method as implemented in SO and HR while preserving the underlying framework of atmospheric state, optical properties, climatological species, ray tracing, and numerical integration. This motivates the development of the Monte Carlo engine, which uses optical properties, ray tracing algorithms, and quadrature identical to that of SO and HR (including those developments noted in Sects. 3.3.3 and 3.3.3) but uses Monte Carlo integration to produce an *unbiased* (i.e. zero error in mean) estimate of observed radiance.

Monte Carlo Integration

The backwards Monte Carlo algorithm for observers with a narrow field of view, as implemented in several radiative transfer codes (Collins et al., 1972; Deutschmann et al., 2011; Oikarinen et al., 1999; Postylyakov, 2004), relies on the method of inverse transform sampling, explained briefly below in terms of the diffuse radiance and source terms used in the SASKTRAN framework. The scope of this paper is limited to scalar radiative transfer; the addition of polarization to the SASKTRAN framework (for both MC and HR) is the subject of ongoing work.

The exactly $(n+1)$ times scattered radiance, I_{n+1}, at a point $\vec{r}$ and in look direction $\hat{\Omega}$ as derived from the equation of radiative transfer is written (for scalar light, for brevity) as

$$I_{n+1}(\vec{r},\hat{\Omega}) = \int_0^{t_{\text{end}}} J_n(\vec{r}',\hat{\Omega}) e^{-\int_0^t k(\vec{r}'')\,\mathrm{d}t'} k(\vec{r}')\,\mathrm{d}t, \tag{3.17}$$

where t is distance along the line of sight measured away from the observer (opposite to the direction of s), $\vec{r}' := \vec{r} + t\hat{\Omega}$, $\vec{r}'' := \vec{r} + t'\hat{\Omega}$ (Bourassa et al., 2008). The change of variables from s (as used in 3.1) to $t = -s$ is made because the backwards Monte Carlo

algorithm considers ray paths coming "out of" the observer, whereas the successive-orders method considers diffuse light scattering "into" the observer line of sight. Under a change of variables to $T(t) = e^{-\int_0^t k(t')\,\mathrm{d}t'}$, Eq. (3.17) becomes

$$I_{n+1}(\vec{r}, \hat{\Omega}) = \int_{T(t_{\text{end}})}^{1} J_n(\vec{r}'(T), \hat{\Omega})\,\mathrm{d}T, \tag{3.18}$$

$\vec{r}'(T) = \vec{r} + t\hat{\Omega} : T = T(t)$. Therefore, an unbiased estimate of $I_{n+1}(\vec{r}, \hat{\Omega})$ is formed by taking the expected value of $J_n(\vec{r}(T), \hat{\Omega})$ over the domain of integration and multiplying by the measure of the domain. Because the integral is over T, the expected value of the integrand must be taken with $\vec{r}'(T)$ distributed such that the distribution of T is uniform. Taking the notation that $\langle F(X)\rangle_{X\sim\xi}$ is the expected value of the random variable F when its argument X follows the distribution ξ, an unbiased estimate of Eq. (3.18) is given by

$$\langle I_{n+1}(\vec{r}, \hat{\Omega})\rangle = [1 - T(t_{\text{end}})] \left\langle J_n(\vec{r}'(T), \hat{\Omega})\right\rangle_{T\sim\text{uni}(T(t_{\text{end}}),1)}. \tag{3.19}$$

Similarly, for scalar light (recall the scalar phase function depends on scattering angle only) the nth-order diffuse source term is

$$J_n(\vec{r}, \hat{\Omega}) = \omega_0(\vec{r}) \int_0^{\pi} \sin(\theta)\bar{p}(\vec{r}, \theta) \int_0^{2\pi} I_n(\vec{r}, \Omega(\theta, \phi))\,\mathrm{d}\phi\,\mathrm{d}\theta, \tag{3.20}$$

where $\bar{p}(\vec{r}, \theta)$ is the normalized phase function and $\omega_0(\vec{r})$ is the single-scattering albedo $k_{\text{scat}}(\vec{r})/k(\vec{r})$. Then the expected value of the integrand over both domains of integration,

$$\langle J_n(\vec{r}, \hat{\Omega})\rangle = 4\pi\omega_0(\vec{r}) \left\langle J_n^{\theta}(\vec{r}, \phi)\right\rangle_{\phi\sim\text{uni}(0,2\pi)}, \tag{3.21}$$

where the scattering angle is sampled by

$$J_n^{\theta}(\vec{r}, \phi) = \langle I_n(\vec{r}, \Omega(\theta, \phi))\rangle_{\theta\sim\bar{p}(\vec{r},\theta),\,\theta\in[0,\pi]}, \tag{3.22}$$

forms an unbiased estimate of the integral.

Implementation

Estimates of I_n for any observer are made by taking the mean of m_n independent samples of Eq. (3.19). To draw a single sample of Eq. (3.19) for order of scatter n, transmission through the atmosphere along a ray is calculated. The atmosphere may be of any type supported

generally in the SASKTRAN framework; i.e. the code supports 1-D, 2-D, and 3-D geometries. The ray may be any ray connected to the observer through some arbitrary *ray history* composed of $(n-1)$ scattering points joined by rays and terminating at the observer. If the ray intersects the ground it is terminated with transmission zero, i.e. photons are not allowed to enter the planetary surface. A target transmission is chosen randomly from a uniform distribution between 1 and the transmission at the end of the ray. If the ray hits the ground and the target transmission is smaller than the ray's transmission through the atmosphere, the scatter is said to happen at the ground intersection, where the ground is treated as a Lambertian surface. Otherwise, the cell in which the target transmission occurs is found, and the scatter point is found by iterating the transmission calculation inside the cell to within some user-defined threshold distance. For most applications this threshold is set to 50.0 m, and finer values result in no significant change in simulated radiances. For atmospheres with regions where the scattering extinction is very large (e.g. cloudy atmospheres); however, it may be desired to decrease this value to better capture the subsurface-like scattering that occurs on the boundary of the optically thick region. Transmission from the sun to the chosen scattering point, T_{sun}, is then calculated, and the sample of I_n is taken as T_{sun} attenuated by the scattering probability from the sun direction into the ray direction, $\overline{p}(\vec{r}, \theta_{\text{sun}})$, and by any factors $(1 - T(t_{\text{end}}))$ and ω_0 (from Eq. 3.19 and 3.21 respectively) in the ray history back to the observer.

Higher-order radiance I_{n+1} is sampled by using a scatter point $\vec{r}_s^{(n)}$ chosen during a sampling of I_n to choose the distribution $\overline{p}(\vec{r}_s^{(n)}, \theta)$ used to sample Eq. (3.21); for ground reflection $\overline{p}(\vec{r}_s^{(n)}, \theta)$ is chosen according to Lambert's cosine law. In a time-forward sense, this chooses an incoming direction for the multiply scattered light; in the backwards Monte Carlo algorithm this chooses an outgoing direction $\hat{\Omega}_s$ for the next element of the ray history. A sample of the higher-order radiance $I_{n+1}(\vec{r}_s^{(n+1)}, \hat{\Omega}_s)$ is then drawn as was done for I_n and is attenuated back to the observer through $\prod_{i=1}^{n}(1 - T^{(i)}(t_{\text{end}}))\omega_0^{(i)}$ as described above. Reusing the 1 through n scattering points as the ray path history for the $(n+1)$th-order scatter allows samples of I_{n+1} to be correlated to samples of $I_{n'}, n' < (n+1)$ to reduce the computational effort of sampling I_{n+1}. Because the observer line of sight ray is cached and the $(n+1)$ order scattering point is connected to the observer through $(n+1)$ rays, reusing ray histories decreases the effort

of sampling I_{n+1} by a factor n.

Following the backwards Monte Carlo algorithm, the ray history begins at the observer, with transmission along the observer line of sight providing the distribution $T^{(1)}(s)$ used to sample I_1. The path is propagated to higher orders of scattering until the attenuation factor $\prod_{i=1}^{n-1}(1 - T^{(i)}(s_{\text{end}}))\omega_0^{(i)}$ falls below some user-specified *minimum weight fraction*, $w_{\min}$, of the already-measured radiance $\sum_{i=1}^{n-1}\langle I_n\rangle$ along that ray history. If the attenuation factor falls below $w_{\min}\sum_{i=1}^{n-1}\langle I_n\rangle$, propagation is stopped; i.e. the ray path is truncated and samples of higher-order radiance are assumed to be zero. Truncation is typically performed for $w_{\min} = \frac{\overline{\sigma}_u}{3000}$, where $\overline{\sigma}_u$ is the user-desired standard deviation (SD) of the algorithm output as a fraction of the simulated signal. Thus the systematic underestimation of higher-order radiance is smaller than the SD in total simulated radiance by a factor of about 3000, which can be considered negligible. If $w_{\min} = 0$, no truncation will occur and this error will be zero as all rays are propagated to some maximum order n_p chosen according to a stratified sampling technique.

The algorithm is multithreaded over ray histories. That is, each thread propagates a separate ray history to n_p orders of scatter, adding a sample to its thread-local estimate of $\langle I_n\rangle$ when the ray is propagated to the nth order. The sample variance of samples of each order and sample covariance between samples of different orders are tracked in each thread. This continues until the estimated SD of $\sum_n\langle I_n\rangle$ falls below $\overline{\sigma}_u\sum_n\langle I_n\rangle$ or until a user-specified maximum number of ray histories, M_u, have been generated. At this point samples of each order of scatter are merged between threads. Since each thread operates completely independently and there is no covariance between estimates from different ray histories, the samples generated by all threads can be merged and treated as though they were generated by a single thread. The sample variance of each $\langle I_n\rangle$ and sample covariance between each $\langle I_{n_1}\rangle$, $\langle I_{n_2}\rangle$ are calculated to estimate the sample variance in $\sum_{n=1}^{n_{\max}}\langle I_n\rangle$. Because the number of covariance terms grows as the square of the number of orders being tracked, samples of $n \geq n_{\text{bin}}$ are binned together; typically $n_{\text{bin}} = 8$ in our implementation. This estimate of sample variance of the observed radiance is accurate to approximately 5 or 10 % (when the higher-order signal is weak or strong respectively) when compared against the variance in MC output from many identical runs. SD of simulation output is therefore equal to the user-desired value to within

5 %.

Because MC resolves rays at every scattering event, it is simple to collect statistics about the physical distribution of scattering points as well as the variance and covariance of different orders of $\langle I_n \rangle$ with essentially zero overhead; user options exist to allow output of these statistics.

3.3.5 Comparison Between the High-Resolution and Monte Carlo Engines

Timing

All timing is carried out on an Intel Core i7-4770 CPU at 3.40 GHz, with 16 GB RAM on a 64 bit Windows 7 OS. All calculations are performed with multithreading over seven threads where the algorithm can be multithreaded.

Timing of the Monte Carlo engine is highly sensitive to wavelength and solar zenith angle: these determine the relative importance of higher-order scattering and geometry dependence of the solar source term in the neighbourhood of the line of sight. The importance of higher-order scattering is discussed in Sect. 3.3.4. Variance of the solar source term increases the variance in samples of I_n because ray histories are chosen independent of the spatial variation in the solar source term. For example, for a limb-viewing line of sight along the terminator many scattering points will be chosen close to the tangent point, but if the path from the tangent point to the sun is optically thick (e.g. as for UV wavelengths) these samples are effectively zero, while most of the non-zero contribution to $\langle I_n \rangle$ comes from samples at higher-altitude scattering points.

Table 3.1 shows the time required to produce MC data for the geometries shown in Fig. 3.4 (discussed in Sect. 3.3.5), averaged over tangent altitude and solar azimuth angle. This is the time required to sample the observed radiance for SD 0.2 and 1.0 % of the measured signal, neglecting the time to fill look-up tables of optical properties and solar transmission (0.98 s per wavelength in MC, which caches solar transmission at high resolution). The above-mentioned deterioration in performance for optically thick lines of sight is obvious – this can be ameliorated using multiple-importance sampling techniques (Veach and Guibas,

Table 3.1: Seconds for MC to estimate the observed radiance for 3 wavelengths [nm] at 4 tangent point solar zenith angles (SZA) and 2 precisions (σ/I_r).

	$\sigma/I_r = 0.002$			$\sigma/I_r = 0.01$		
	wavelength [nm]			wavelength [nm]		
SZA	322.5	350.3	602.4	322.5	350.3	602.4
20°	15.7	12.5	2.7	0.67	0.61	0.126
60°	5.9	5.6	1.5	0.25	0.23	0.074
80°	1.5	2.1	0.8	0.07	0.10	0.046
89°	17.7	2.0	0.7	0.68	0.11	0.040

1995), which will be implemented in future releases. For tangent heights above 30 km, where the atmosphere is less optically thick in the near UV, equivalent values for the leftmost data column of Table 3.1 are between 0.03 and 0.42 s.

HR simulations of the accuracy shown in Fig. 3.4, by contrast, require approximately 79 s per wavelength. The HR engine can simulate many observer lines of sight simultaneously and becomes slightly more efficient when many wavelengths are simulated, so direct comparison to MC is difficult. If HR is run at lower resolution but still with 11 diffuse profiles, which increases the error with respect to MC by at most 0.8 % for the configurations in Fig. 3.4, and by less than 0.4 % for the SZA $< 89°$ cases, the same simulation requires only 17 s per wavelength.

Direct comparison of the HR and SO (with coupled diffuse profiles) is more straightforward. Runtime (per wavelength) to simulate radiance over a large range of near-UV through near-IR wavelengths is shown in Table 3.2. The time required for either model to run is largely independent of wavelength and geometry, and is approximately constant for a reasonable number (i.e. ≤ 5000) of lines of sight. While HR is consistently slower than SO by a factor of approximately 1.25, SO is memory-limited and cannot reproduce the accuracy of HR under conditions requiring many diffuse profiles.

Table 3.2: Representative runtime (per wavelength) and RAM usage for HR and SO for similar resolutions and various numbers of diffuse profiles (DP).

DP		1	5	11
Runtime (s)	SO	0.41	2.64	6.06
	HR	0.53	3.26	7.51
RAM (GB)	SO	0.57	3.88	8.72
	HR	0.09	0.56	1.27

Accuracy

The SO engine was compared to several other radiative transfer models in Bourassa et al. (2008). The HR engine can be configured to give results identical to those of SO to approximately machine precision; in any case their difference is orders of magnitude lower than the differences reported between models in Bourassa et al. (2008). The validation of SO in Bourassa et al. (2008) then applies equally to HR in this configuration. We will now compare the output of HR, configured at resolution higher than that which gives output identical to that of SO, to the MC engine built into the SASKTRAN framework.

HR and MC have been compared for a variety of solar conditions and wavelengths. The atmosphere used is representative of a "standard" atmosphere away from the Earth surface, consisting of Rayleigh scatterers, ozone, and aerosol. The surface albedo was set to 0.95 in order to maximize the multiply scattered signal and thereby accentuate divergence of the two engines.

Figure 3.4 shows the percent difference between output of the two engines for a set of observer–sun geometries at three wavelengths, with HR run using 11 diffuse profiles and MC run with 250 000 ray histories per line of sight for SD better than 0.2 % (recall the first-order signal often dominates and converges quickly in MC). With the exception of dusk conditions where the observer is looking across the terminator towards the dayside (top left-hand frames), there is agreement between the engines to within the 0.2 % maximum SD of MC output. The divergent cases are those in which the line of sight spans a large range of solar zenith angles and is optically thick due to scattering. Note that agreement is still good for wavelength 602.29 nm, for which the Rayleigh atmosphere is optically thin relative

to wavelengths in the range of 340 nm. Figure 3.4 indicates that more than 11 diffuse profiles are needed for HR to converge only when the atmosphere is quite optically thick and the observer geometry is such that the diffuse source term changes drastically along the line of sight.

Figure 3.5 shows the number of diffuse profiles required to reach 0.2 % agreement between HR and MC for tangent altitude 10 km and wavelength 345 nm. The single-scattering albedo at 345 nm is high; therefore higher orders of scatter represent a large contribution to the simulated radiance. Figure 3.5 then represents the number of diffuse profiles required to simulate limb radiance accurate to 0.2 % in the approximate "worst-case" scenario in a one-dimensional atmosphere. Where MC is slow to converge (when the line of sight is in darkness where $T(t)$ changes rapidly, the shaded region in Fig. 3.5), HR, using 119 coupled diffuse profiles, is taken as the reference engine.

3.4 Optical Spectrograph and InfraRed Imaging System

As an example usage case, the two radiative transfer models are applied to data from the Optical Spectrograph and InfraRed Imaging System (OSIRIS), a limb-scatter instrument launched in 2001 on board the Odin satellite (Llewellyn et al., 2004). Odin is in a sun-synchronous orbit at an altitude of 600 km with ascending and descending node local times of 18:00 and 06:00 respectively, providing coverage from 82° S to 82° N. The Optical Spectrograph (OS) is the primary instrument, measuring wavelengths between 284 and 810 nm with approximately 1.0 nm resolution. A single line of sight extends from the instrument and exposes the OS detector to limb-scatter radiance. Odin nods as it orbits, scanning the line of sight tangent point from 7 to 75 km during typical operation; during some scans this range is extended up to 110 km. A scan takes approximately 90 s and provides vertical sampling every 2 km with a vertical resolution of approximately 1 km. Solar zenith angle at the tangent point varies between 60 and 120 °, with the solar scattering angle between 60 and 120 ° as well. For operational retrievals, only scans with a solar zenith angle at the tangent point less than 90° are used.

Figure 3.6 illustrates an up-scan–down-scan sequence of the OS line of sight when OSIRIS scans to 110 km. In panel A the satellite position is marked by open circles, and the tangent point by solid dots. For clarity only every fifth measurement is shown. Panel B shows the ground track of the tangent points and with contours of constant solar zenith angle. These scans have a solar scattering angle close to 60°, which is representative of the largest change in solar zenith angle over the course of any OSIRIS scan. Scans with solar scattering angle near 90° run more parallel to the contours and therefore experience little to no change in solar zenith angle.

A consequence of the scanning of the line of sight is that the line of sight tangent point traverses a larger distance during down-scans than up-scans, as up-scans tend to cancel the forward motion of the satellite. This causes larger changes in the local illumination conditions and has implications for the accurate modelling of the limb-scatter radiances. The tangent point of an up-scan typically covers approximately 4° along the orbit track, with that of a down-scan covering 7°; most of this distance is covered in the latitudinal direction. For scans reaching 110 km this is extended to 7 and 11° for up- and down-scans respectively. Many OSIRIS scans therefore span the terminator to an extent dependent upon solar angles and whether Odin is scanning up or down. The UV diffuse radiance field is remarkably difficult to model accurately in this geometry, which is problematic as bias in a radiative transfer model can propagate through a retrieval algorithm to cause systematic errors in retrieved atmospheric parameters. The character of this error in the OSIRIS ozone retrieval is explored in the following section, and it is shown to be remedied through the use of higher-resolution radiative transfer modelling.

3.5 Radiative Transfer Impacts on Ozone Retrieval

3.5.1 Testing Procedure

From Figs. 3.4 and 3.5, the most difficult cases to model are geometries with high solar zenith angles, in particular forward-scattering scenarios when the line of sight begins in darkness. The operational OSIRIS ozone product, version 5.07, uses one diffuse profile for retrievals:

inaccuracies in this configuration of the forward model may have induced errors in retrieved species profiles when OSIRIS is measuring difficult-to-model geometries.

To test this two studies were performed. First, approximately 2600 OSIRIS scans where it is difficult to accurately model the diffuse field were selected from 2008 and 2009. These are scans with solar zenith angles greater than 80°, and where the maximum scan altitude is greater than 100 km. Special mode scans where the line of sight is out of the orbital plane are excluded from this set. These criteria serve to maximize the variation in solar zenith angles over the duration of a scan. HR was then used to retrieve ozone with the OSIRIS data, once using one diffuse profile and again using five diffuse profiles. The single-profile retrieval represents the current Odin–OSIRIS data processing algorithm, whereas the five-profile retrieval represents roughly the best-quality retrieval that could easily be performed using the faster SO engine on a computer with 4 GB RAM. Ozone is retrieved using a multiplicative algebraic reconstruction technique as described in detail by Degenstein et al. (2009).

Next a simulation study was performed where MC was used to simulate the OSIRIS data with a SD of at most 0.2 %, roughly the reported precision of OSIRIS radiance measurements in the UV. For simulation purposes a monthly averaged ozone climatology, specified on a 500 m grid, was used rather than the scan-by-scan retrieved values to avoid biasing the results with retrieval errors. For each scan, the OSIRIS v5.07 NO_2 and aerosol data products were supplied as inputs to both MC and HR. Ozone was then retrieved with HR from the simulated data, again with both one and five diffuse profiles. Note that all simulations were performed using a one-dimensional atmosphere as is done in the OSIRIS operational retrievals. We make no attempt to quantify the effect of three-dimensional variability on the retrieval.

3.5.2 Discussion

Figure 3.8 shows the percent difference in retrieved ozone when the forward model is run with five diffuse profiles rather than one. The left panel shows the percent difference when retrieving from OSIRIS radiance measurements, while the right panel shows percent difference when retrieving from the MC-simulated scans. In general there is excellent agreement between the results retrieved from OSIRIS data and those retrieved from Monte Carlo-simulated data.

This indicates that the observed biases are a consequence of the retrieval algorithm sensitivity to errors in the forward model rather than error inherent to the OSIRIS measurements. Furthermore, it is good evidence that MC is able to simulate OSIRIS scans effectively. The simulated data are noisier than the OSIRIS data, suggesting that the random noise component of the OSIRIS data is less than the maximum Monte Carlo SD of 0.2 %.

Using more diffuse profiles in the retrieval forward model has the effect of changing retrieved values by up to a few percent for solar scattering angles far from 90°. There is a distinct separation in the magnitude and direction of this effect when the instrument is scanning up vs. when the instrument is scanning down. The magnitude of the effect is less for up-scans owing to their smaller span in solar zenith angle (see Fig. 3.6). At high altitudes the effect is stronger, with a maximum systematic bias of approximately 4 % in the down-scanning backscatter case. Near 30 km the separation in the effect between up- and down-scans disappears; however there is still a clear systematic effect which depends on solar scattering angle. At low tangent altitudes the separation reappears and is reversed; down-scans now underestimate retrieved ozone, whereas at high altitudes this is overestimated.

To better understand the effect as a function of altitude, we separate scans into three distinct cases based on scattering angle, Θ:

- $\Theta < 70°$ (solar zenith angle increasing over the period of a scan),
- $85° < \Theta < 105°$ (solar zenith angle roughly constant over the period of a scan),
- $110° < \Theta$ (solar zenith angle decreasing over the period of a scan),

as shown in Fig. 3.7. No separation is observed between up- and down-scans in the $85° < \Theta < 95°$ case. In the forward-scatter case ($\Theta < 70°$), the magnitude of the relative bias between up- and down-scanning directions is largest at high altitudes, decreases to 0 at approximately 30 km, then switches sign and continues to increase with decreasing altitude. The backward-scatter case ($110° < \Theta$) shows a similar but reverse relative bias to the forward-scatter case: up-scans overestimate at high altitudes for backward-scatter geometries and underestimate in forward-scatter geometries. The forward and backward-scatter cases are not perfectly mirrored below approximately 30 km because changes in retrieved ozone are sensitive to the amount of forward-scattering aerosol present in the atmosphere. The excellent agreement of

relative biases when comparing retrievals from simulated vs. OSIRIS measurements seen in Fig. 3.7 reinforces that the observed up-scan/down-scan bias separation is due to errors in the forward model, as suggested by Fig. 3.8.

In order to understand the cause of the bias, we need to understand how changes in radiance affect the ozone retrieval. At high altitudes, the ozone retrieval uses measurement vectors of the form

$$\vec{y} = \log\left(\frac{I(\lambda_{\text{ref}}, h)}{I(\lambda_{\text{ref}}, h_{\text{ref}})}\right) - \log\left(\frac{I(\lambda, h)}{I(\lambda, h_{\text{ref}})}\right), \tag{3.23}$$

where λ is a wavelength sensitive to changes in ozone at tangent altitude h, λ_{ref} is a reference wavelength not sensitive to ozone, and h_{ref} is a high altitude where the radiances are normalized. The measurement vector, $\vec{y}$, increases monotonically with the amount of ozone. For up-scans in which solar zenith angle increases over the period of one scan (solar scattering angle less than 90°), the high-altitude normalization measurement occurs at a solar zenith angle greater than that of the measurements used in the retrieval. As the diffuse field is (for simple atmospheres) a strictly decreasing function in solar zenith angle, both terms of the form $I/I(h_{\text{ref}})$ are systematically underestimated by the use of one diffuse profile. High altitudes in the ozone retrieval use retrieval wavelengths in the Hartley–Huggins absorption band: here the strong absorption means this wavelength is not very sensitive to changes in the diffuse field. The reference wavelength used at high altitude is approximately 350 nm, which has little absorption and is very sensitive to changes in the diffuse field. Thus the measurement vector is overall underestimated in this case, leading to an underestimation of retrieved ozone at high altitude, as seen in Fig. 3.7.

At low altitudes the opposite effect is observed. Here, the retrieval wavelength used is in the Chappuis band, with normalization wavelengths on both sides of the band. The relative sensitivity of these wavelengths to changes in the diffuse field depends on the amount and type of aerosol present. Overall, however, the retrieval wavelength is more sensitive to the diffuse field than the reference wavelengths, leading to an overestimation of the measurement vector and thus ozone.

Down-scans have the opposite effect of up-scans. For the same geometry, the reference altitude measurement occurs at a solar zenith angle less than the retrieval measurements.

This means that the terms $I/I(h_{\text{ref}})$ are systematically overestimated through the use of one diffuse profile. Therefore, by the same reasoning, retrieval from down-scan measurements should overestimate ozone at high altitudes and underestimate ozone at low altitudes, as observed in Fig. 3.7.

Similarly, scans with solar scattering angle greater than 90° produce a reversed profile (solar zenith angle decreasing over the period of one scan). For up-scans, the normalization altitude has a local solar zenith angle less than the measurement's solar zenith angles, causing an overestimation of ozone at high altitudes and an underestimation of ozone at low altitudes. Once again, down-scans demonstrate the reverse bias.

The primary advantage of retrieving from simulated measurements is that the true state is known and can be compared against. In Fig. 3.9 the retrieved ozone profile using five diffuse profiles is compared to the known true state. The bias between up- and down-scanning directions is not present. Furthermore, there is excellent agreement in all cases above 20 km, suggesting five diffuse profiles is sufficient to estimate the multiply scattered field for ozone retrievals in OSIRIS geometries. The remaining $\sim 0.5\,\%$ underestimation in the backscattering case between 25 and 50 km is thought to be caused by the use of 1000 m homogeneous shells in the forward model. The cause of the "wobble" above 50 km is currently unknown, but it is suspected to be an issue of interpolating coarse-resolution OSIRIS measurements onto a finer grid near the highest reference altitude.

So far we have limited our discussion to ozone retrievals with OSIRIS geometries; however similar effects should exist for other instruments and species. The effect on other species is heavily dependent on the exact retrieval algorithm used; thus we merely reiterate that when using one diffuse profile the altitude normalized radiance, $I/I(h_{\text{ref}})$, has systematic biases which depend on the measurement geometry. For imaging instruments a similar effect exists. In an image, the high-altitude measurement has a tangent point closer to the observer than the low-altitude measurements (there is approximately a 1° change from 0 to 60 km in the tangent point for an imaging instrument orbiting at an altitude of 600 km). Therefore an imaging instrument will only exhibit the down-scan biases shown in Figs. 3.8 and 3.6, albeit to a lesser degree. However, in more extreme cases where the scattering angle is closer to pure forward or backward scatter, the bias may be significant.

3.6 Conclusions

Two new radiative transfer models have been developed within the SASKTRAN framework: A new high-resolution successive-orders model and a Monte Carlo reference model.

The high-resolution model is intended for use as an accurate spherical radiative transfer model that operates without the assumption of horizontal homogeneity of the atmosphere and is fast enough for use in limb-scatter retrievals. Regions of large extinction (e.g. cirrus clouds) are handled through an adaptive integration step. Variations in atmospheric composition along the horizontal direction are accounted for through new two- and three-dimensional atmosphere modes. Weighting functions for number density of scattering and absorbing species can be approximated analytically. These approximate weighting functions deliver better performance than those calculated using the traditional single-scattering approximation and require negligible time to compute compared to the full radiative transfer calculation.

The Monte Carlo model is intended for use as an accurate reference model that estimates solutions to the radiative transfer problem without bias. The model is implemented within the SASKTRAN framework and is therefore useful as a tool for error checking other models within the framework. Furthermore, it can been used to prescribe the resolution necessary in faster successive-orders discrete-ordinates models to achieve accuracy to within some limit. In this work, configurations were found that allow the high-resolution model to agree with the Monte Carlo reference model to within 0.2 % for a wide variety of solar geometries and wavelengths.

The two radiative transfer models were used to identify and eliminate a bias in the OSIRIS ozone product. OSIRIS scans were simulated using the Monte Carlo model, and vertical profiles of ozone were retrieved from these simulated scans using the high-resolution model. It was shown that calculating the multiply scattered diffuse radiance field at only one solar zenith angle introduces a bias of up to 4 % for typical OSIRIS geometries. The shape and magnitude of the bias is different when the instrument is scanning up or down, and is an artefact of the correlation between scan height and local solar zenith angle, complicated by the use of a high-altitude normalization measurement in the retrieval algorithm. It was found

that calculating the diffuse radiance field at five equally spaced solar zenith angles eliminates the effect and is sufficient to reduce biases in the OSIRIS ozone retrieval originating from horizontal gradients in the diffuse field to within 0.5 %.

3.7 Acknowledgements

This work was supported by the Natural Sciences and Engineering Research Council (Canada) and the Canadian Space Agency. Odin is a Swedish-led satellite project funded jointly by Sweden (SNSB), Canada (CSA), France (CNES), and Finland (Tekes).

Edited by: M. Weber

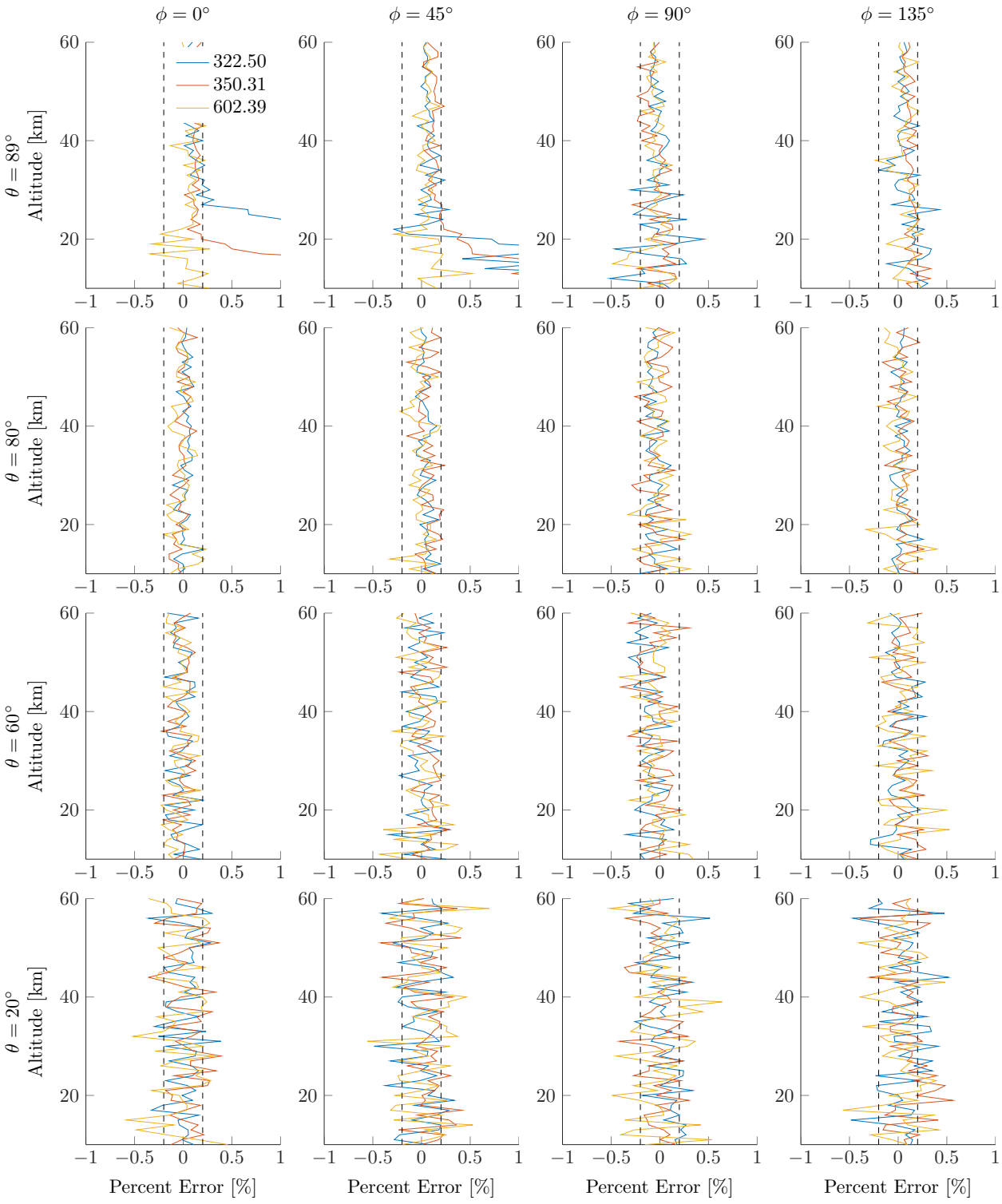

Figure 3.4: Percent difference in simulated radiance between HR and MC ((HR − MC)/MC · 100 %) as a function of altitude at select solar zenith angles, θ, and solar azimuth angles ϕ. Dashed vertical lines indicate the estimated SD of the Monte Carlo results. HR was run with 11 diffuse profiles.

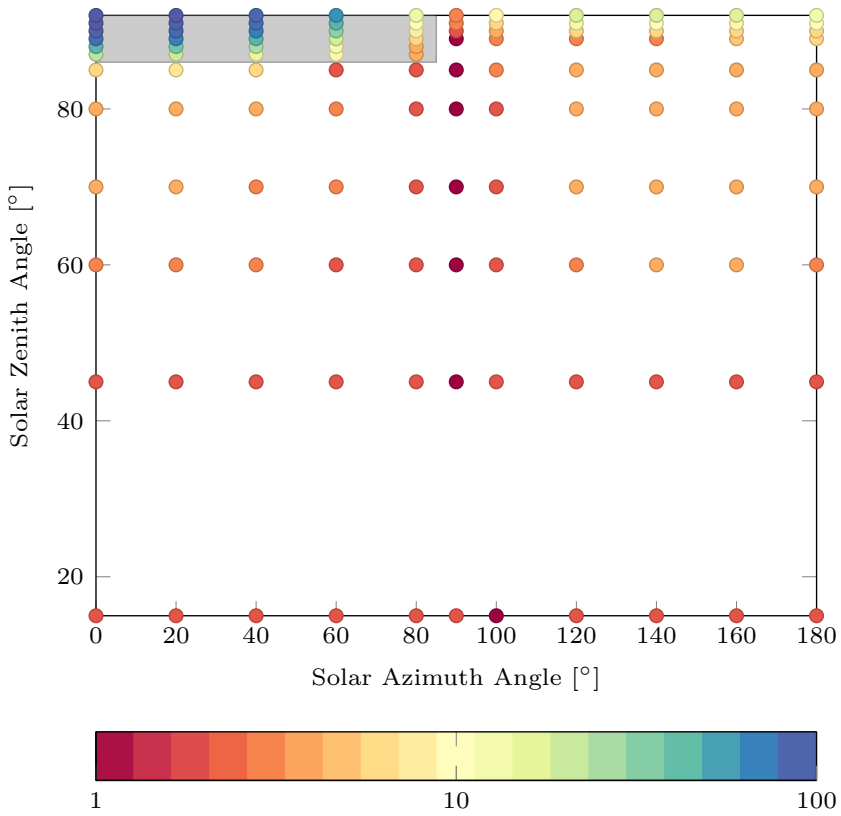

Figure 3.5: Number of diffuse profiles needed to get 0.2 % agreement with MC, at 10 km altitude and 345 nm. In the shaded region the reference calculation was done using HR with 119 diffuse profiles.

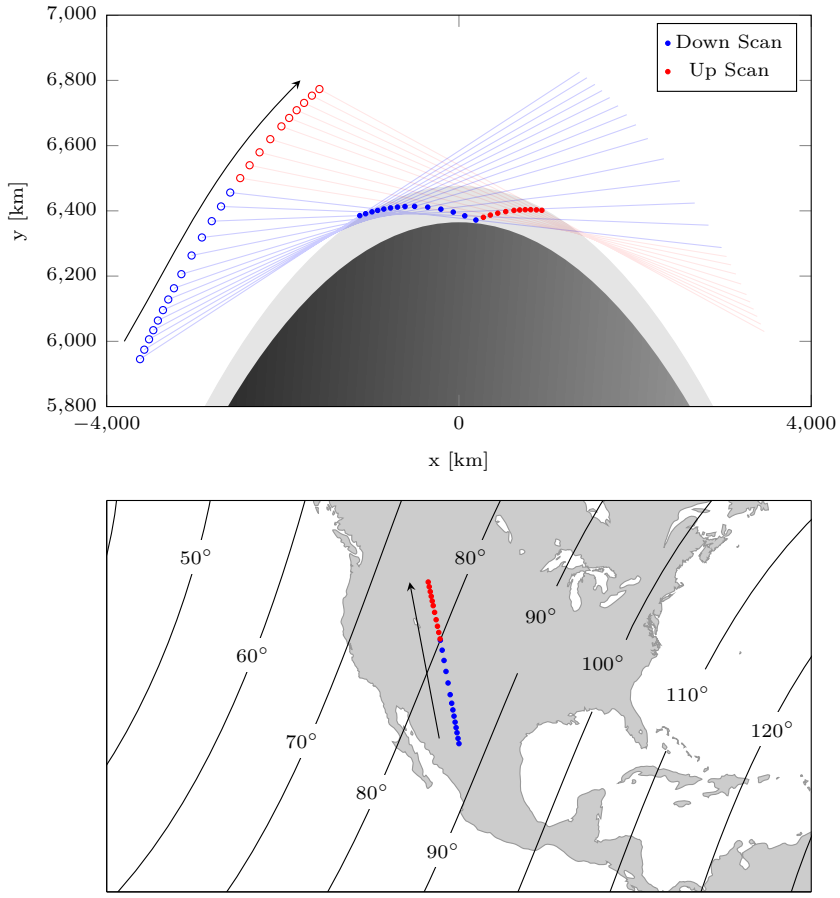

Figure 3.6: Typical movement of the Odin satellite (open circles) and tangent point (closed circles) as the line of sight is scanned down and up, shown in red and blue respectively. The bottom panel shows the ground tracks of the tangent points; contours mark lines of constant zenith angle.

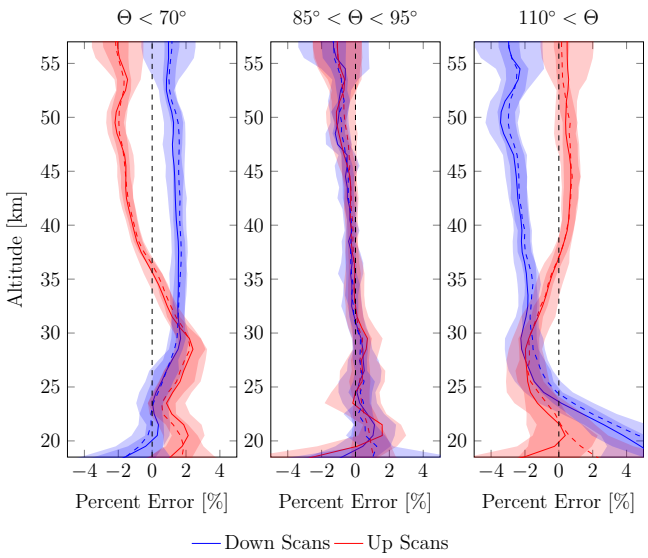

Figure 3.7: Mean percent difference between retrieved ozone number density when the forward model is run with one diffuse profile compared to five, i.e. $([O_3]^{(1)} - [O_3]^{(5)})/[O_3]^{(5)} \cdot 100\,\%$, as a function of altitude in select solar scattering angle bins. Shaded areas are the SD of the values. Solid and dashed lines represent simulated and OSIRIS measurements respectively.

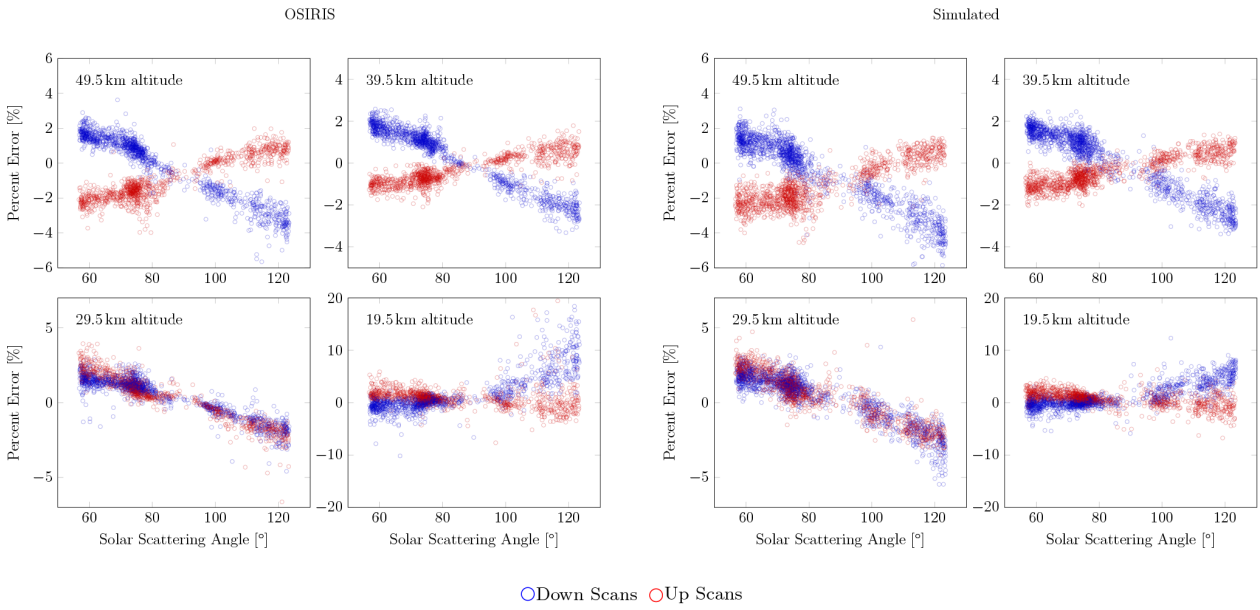

Figure 3.8: Percent difference between retrieved ozone number density when the forward model is run with one diffuse profile compared to five, i.e. $([O_3]^{(1)} - [O_3]^{(5)})/[O_3]^{(5)} \cdot 100\,\%$, as a function of solar scattering angle at select altitudes. Red and blue circles correspond to when the instrument is scanning upward and downward respectively. The left panel shows the results when retrieving from OSIRIS measurements, while the right panel is the results when retrieving from MC-simulated measurements.

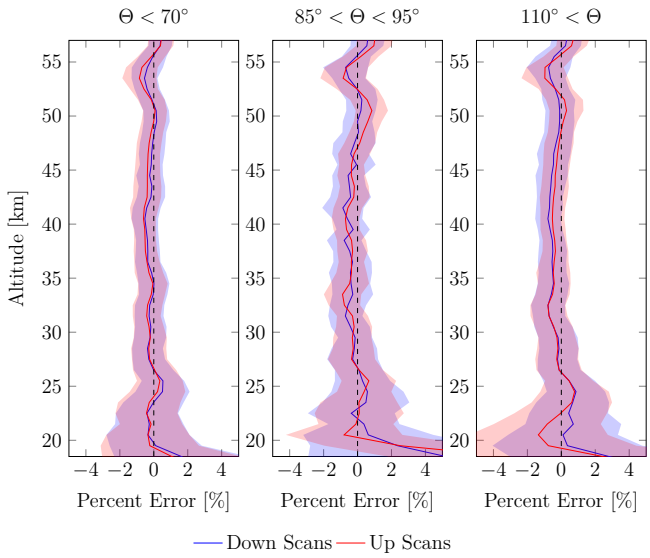

Figure 3.9: Mean percent error between the ozone profile retrieved when using five diffuse profiles in the forward model and the simulated known value, i.e. $([O_3]^{(5)} - \text{correct})/\text{correct} \cdot 100\,\%$.

Chapter 4

Two-Dimensional Analytic Weighting Functions For Limb Scattering

D. J. Zawada, A. E. Bourassa, D. A. Degenstein

Most retrieval methods require the Jacobian matrix of the forward model, i.e., the derivative of the forward model with respect the quantities being retrieved. It is always possible to calculate the Jacobian matrix using perturbation techniques, but computationally efficient methods are required for retrieval problems. This manuscript presents efforts performed to solve one of the major challenges of performing a tomographic retrieval identified in Section 2.4.3, efficiently calculating the Jacobian matrix. Also shown is a quantification of the effect of the approximation used through comparisons with perturbation methods.

The two-dimensional (in altitude and along line of sight dimension) Jacobian matrix calculation is necessary for the future tomographic retrieval; however the same methods are also applicable to one-dimensional (altitude) Jacobian calculations. These one-dimensional Jacobians have been used for the retrieval of water vapour from the Special Heterodyne Observations of Water (SHOW) instrument Langille et al. (2018). They are also currently being explored for use in future versions of the OSIRIS retrievals.

I was responsible for developing the technique, performing the analysis, and authoring the manuscript.

This manuscript has been published in the Journal of Quantitative Spectroscopy and Radiative Transfer, and unless otherwise stated the version presented here is unchanged. The layout of figures and equations and the format of cross references has been modified to match that of the overall document.

the entirety of the article in a thesis or dissertation that is not commercially published (see https://www.elsevier.com/about/our-business/policies/copyright#Author-rights).

Zawada, D., Bourassa, A., & Degenstein, D. (2017). Two-Dimensional Analytic Weighting Functions For Limb Scattering. *Journal of Quantitative Spectroscopy and Radiative Transfer*, *200*, 125–136. doi:10.1016/j.jqsrt.2017.06.008

4.1 Abstract

Through the inversion of limb scatter measurements it is possible to obtain vertical profiles of trace species in the atmosphere. Many of these inversion methods require what is often referred to as weighting functions, or derivatives of the radiance with respect to concentrations of trace species in the atmosphere. Several radiative transfer models have implemented analytic methods to calculate weighting functions, alleviating the computational burden of traditional numerical perturbation methods. Here we describe the implementation of analytic two-dimensional weighting functions, where derivatives are calculated relative to atmospheric constituents in a two-dimensional grid of altitude and angle along the line of sight direction, in the SASKTRAN-HR radiative transfer model. Two-dimensional weighting functions are required for two-dimensional inversions of limb scatter measurements. Examples are presented where the analytic two-dimensional weighting functions are calculated with an underlying one-dimensional atmosphere. It is shown that the analytic weighting functions are more accurate than ones calculated with a single scatter approximation, and are orders of magnitude faster than a typical perturbation method. Evidence is presented that weighting functions for stratospheric aerosols calculated under a single scatter approximation may not be suitable for use in retrieval algorithms under solar backscatter conditions.

4.2 Introduction

Recent satellite based instruments which measure limb scattered sunlight in the ultraviolet-visible-near infrared (UV-VIS-NIR) spectral region (Bovensmann et al., 1999; Flynn et al., 2004; Llewellyn et al., 2004; Mauldin et al., 1998) have been successfully used to obtain

vertical profiles of trace species in the atmosphere with near global coverage (e.g. Bourassa et al., 2007; Degenstein et al., 2009; Rault, 2005; Rault and Loughman, 2013b; Rozanov et al., 2005; Rozanov et al., 2011b; Taha et al., 2011; von Savigny et al., 2003). In order to convert raw limb spectra to vertical profiles of atmospheric constituents both a radiative transfer model and a retrieval technique are required. For modelling the observed radiance in this geometry and spectral region it is necessary to account for both the multiple scattering component (Oikarinen et al., 1999) and the curvature of the Earth (McLinden and Bourassa, 2010).

Derivatives of the radiance with respect to atmospheric constituents, or weighting functions (WF), are useful quantities for many retrieval algorithms from limb measurements (Rodgers, 2000). Given any radiative transfer model (RTM), weighting functions can be calculated by perturbing the quantity of interest and using a finite difference technique. However, these methods require one additional run of the RTM for every atmospheric grid cell, which quickly becomes computationally prohibitive. A common approximation made is to calculate the WFs only considering single scatter effects in the RTM. These calculations can be performed with analytic expressions or with numerical perturbation techniques. Kaiser and Burrows (2003) have shown that these single scatter WFs are sufficient for limb retrievals of ozone and nitrogen dioxide in the stratosphere, and this technique is commonly used in operational retrieval algorithms (e.g. Rault and Loughman, 2013b; Rozanov et al., 2007; Rozanov et al., 2011b).

All current operational retrievals from limb scatter measurements employ the assumption of horizontal homogeneity, i.e, the assumption that atmospheric constituents vary only in altitude. Retrievals from limb emission measurements commonly use a two-dimensional retrieval technique, where quantities of interest are retrieved simultaneously in altitude and in an along orbital track dimension (e.g. Degenstein et al., 2003; Livesey et al., 2006; Papandrea et al., 2010). To perform these retrievals it is required to calculate two dimensional WFs i.e. the derivative of the radiance with respect to atmospheric constituents varying both in altitude and the along line of sight direction. These weighting functions are typically calculated through direct differentiation of the solution of the radiative transfer equation (RTE), and the resultant closed form expressions are evaluated alongside the RTE solution. Analogous

techniques are difficult to apply to limb scatter measurements due to the inclusion of the scattering source function which complicates the solution of the RTE.

In the plane-parallel scattering case there exist a wide variety of techniques to perform the WF calculation (see Rozanov and Rozanov, 2007, and references therein) but relatively little work has been done for the fully spherical geometry. Walter et al. (2006) have outlined a general method to obtain WFs for the spherical geometry, however implementations have only been performed for the homogeneous shell atmosphere (1D) case. To our knowledge the only RTM capable of calculating two dimensional WFs without perturbation methods is the Monte Carlo model McArtim which has implemented methods to calculate these two dimensional WFs by storing photon trajectories (Deutschmann et al., 2011). An earlier version of the model was used to perform a two-dimensional retrieval of NO2 from SCIAMACHY measurements (Puķıte et al., 2008). However, Monte Carlo RTMs are usually not suitable for operational retrieval algorithms due to the implicit variance and large computational burden.

Recently the SASKTRAN-HR RTM has been developed (Zawada et al., 2015) as an extension to the original SASKTRAN RTM (Bourassa et al., 2008). SASKTRAN-HR adds the ability to model the radiance field when the atmosphere is varying in three dimensions. One of the design goals of SASKTRAN-HR is to create an RTM suitable for two-dimensional retrievals of trace species from limb scatter measurements. This paper describes the theory and performance of the two-dimensional analytic weighting function calculation in SASKTRAN-HR. The method includes all contributions from the first order of scatter and contains approximations for higher scatter order effects. Sections 4.3 and 4.4 describe the basic theory and implementation of the method within SASKTRAN-HR. Section 4.5 demonstrates the accuracy of the method by comparing the results to perturbation methods and also looks at the timing differences between the methods.

4.3 Theoretical Basis

4.3.1 Forward Model Description

Following the notation of Bourassa et al. (2007) and Zawada et al. (2015) for an implicit wavelength λ, the observed radiance, I, is given by,

$$I(\vec{r}_0, \hat{\Omega}) = \int_{s_{\text{end}}}^{0} J(s, \hat{\Omega}) e^{-\tau(s,0)}\, ds + I_{\text{end}}(\vec{r}_{\text{end}}, \hat{\Omega}) e^{-\tau(\vec{r}_{\text{end}}, \vec{r}_0)}, \tag{4.1}$$

here $J(s)$ is the source function, I_{end} is the radiance at the end of the path, s is the distance along the path defined by the observer location $\vec{r}_0$ and look direction $\hat{\Omega}$, and the optical depth, τ, is given by,

$$\tau(s, 0) = \int_{s}^{0} k(s)\, ds, \tag{4.2}$$

where k is the extinction. The extinction may be broken up into two terms,

$$k(s) = k_{\text{abs}}(s) + k_{\text{scat}}(s), \tag{4.3}$$

where k_{abs} is the extinction from absorption processes, and k_{scat} is the extinction from scattering processes. Each observer location and look direction pair is referred to as a single line of sight.

In the UV-VIS-NIR spectral region the dominant radiation source is scattering, given by,

$$J(s, \hat{\Omega}) = k_{\text{scat}}(s) \int_{4\pi} I(s, \hat{\Omega}') \bar{p}(s, \hat{\Omega}', \hat{\Omega})\, d\hat{\Omega}', \tag{4.4}$$

where $\bar{p}$ is the extinction weighted sum of normalized phase functions for each individual species, p_i, i.e.

$$\bar{p}(s, \hat{\Omega}', \hat{\Omega}) = \sum_i p_i(s, \hat{\Omega}', \hat{\Omega}) \cdot \frac{k_{\text{scat},i}(s)}{k_{\text{scat}}(s)}. \tag{4.5}$$

Together, these equations form a coupled integral equation for the radiance. SASKTRAN-HR solves this equation with a successive orders technique (Bourassa et al., 2008; Zawada et al., 2015); the radiance from light that is scattered n times is used as the source term to calculate the radiance from light that has been scattered $n + 1$ times. The technique is equivalent to the Neumann series solution of the RTE initialized with the source from the direct solar beam.

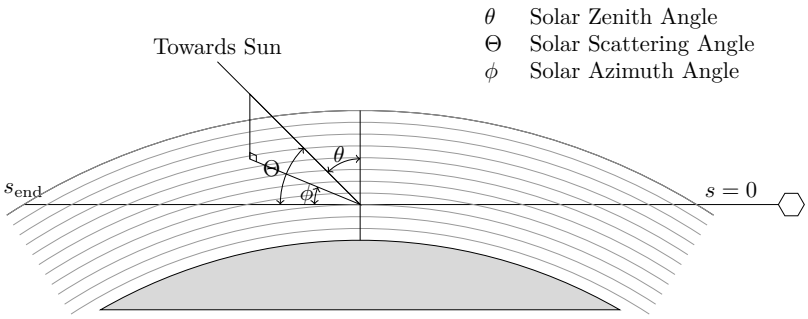

Figure 4.1: Sample limb viewing geometry and associated solar angles. Figure adapted from Zawada et al. (2015).

At the end of the iterative solution, the quantity obtained is the scattering source function in a region of interest which is typically the smallest possible cone containing every line of sight. The final observed radiance for each observer location and look direction (line of sight) is found by evaluating the line integral in Eq. (4.1). These line integrations are computationally fast relative to the solution of the RTE, therefore the calculation time is only weakly dependent on the number of lines of sight.

4.3.2 Calculation of Weighting Functions

The weighting function of an arbitrary quantity is defined as the derivative of the radiance with respect to that quantity. Typically what is desired for inverse problems is the weighting function with respect to the extinction of species i within atmospheric grid cell j, which we will denote $w(k_{i,j})$ and define by the relation,

$$w(k_{i,j}) = \frac{\partial I(\vec{r}, \hat{\Omega})}{\partial k_{i,j}}. \tag{4.6}$$

To calculate the weighting function, we begin by taking the derivative of Eq. (4.1) neglecting refraction effects,

$$w(k_{i,j}) = \int_{s_{\text{end}}}^{0} \left[\frac{\partial J(s, \hat{\Omega})}{\partial k_{i,j}} - \frac{\partial \tau(s,0)}{\partial k_{i,j}} J(s, \hat{\Omega}) \right] e^{-\tau(s,0)}\, ds - I(\vec{r_{\text{end}}}, \hat{\Omega}) \frac{\partial \tau(\vec{r}_{\text{end}}, \vec{r}_0)}{\partial k_{i,j}} e^{-\tau(\vec{r}_{\text{end}}, \vec{r}_0)}. \tag{4.7}$$

The scattering source function can be split into two terms, the solar and diffuse sources, i.e. $J = J_{\text{sun}} + J_{\text{dif}}$. The solar source represents light directly from the sun and is,

$$J_{\text{sun}}(\vec{r}, \hat{\Omega}) = F_{\text{sun}} e^{-\tau(\text{sun}, \vec{r})} \overline{p}(\vec{r}, \hat{\Omega}_{\text{sun}}, \hat{\Omega}) k_{\text{scat}}(\vec{r}), \tag{4.8}$$

where F_{sun} is the solar irradiance. The diffuse source is,

$$J_{\text{dif}}(\vec{r},\hat{\Omega}) = k_{\text{scat}}(\vec{r}) \int_{4\pi} I_{\text{dif}}(\vec{r},\hat{\Omega}')\overline{p}(\vec{r},\hat{\Omega}',\hat{\Omega})\ d\hat{\Omega}', \tag{4.9}$$

where I_{dif} represents the radiance from all sources other than the direct solar beam, i.e., light that has been scattered more than once in the atmosphere or reflected off the ground and then scattered. Straightforward calculations yield,

$$\begin{aligned}\frac{\partial J_{\text{sun}}(\vec{r},\hat{\Omega})}{\partial k_{i,j}} = J_{\text{sun}}(\vec{r},\hat{\Omega})\Bigg[&- \frac{\partial \tau(\text{sun},\vec{r})}{\partial k_{i,j}} \\ &+ \frac{1}{\overline{p}(\vec{r},\hat{\Omega}_{\text{sun}},\hat{\Omega})}\frac{\partial \overline{p}(\vec{r},\hat{\Omega}_{\text{sun}},\hat{\Omega})}{\partial k_{i,j}} \\ &+ \frac{1}{k_{\text{scat}}(\vec{r})}\frac{\partial k_{\text{scat}}(\vec{r})}{\partial k_{i,j}}\Bigg],\end{aligned} \tag{4.10}$$

and,

$$\begin{aligned}\frac{\partial J_{\text{dif}}(\vec{r},\hat{\Omega})}{\partial k_{i,j}} = &\frac{J_{\text{dif}}(\vec{r},\hat{\Omega})}{k_{\text{scat}}(\vec{r})}\frac{\partial k_{\text{scat}}(\vec{r})}{\partial k_{i,j}} \\ &+ k_{\text{scat}}(\vec{r}) \int_{4\pi} \frac{\partial I_{\text{dif}}(\vec{r},\hat{\Omega})}{\partial k_{i,j}}\overline{p}(\vec{r},\hat{\Omega}',\hat{\Omega})\ d\hat{\Omega}' \\ &+ k_{\text{scat}}(\vec{r}) \int_{4\pi} I_{\text{dif}}(\vec{r},\hat{\Omega})\frac{\partial \overline{p}(\vec{r},\hat{\Omega}',\hat{\Omega})}{\partial k_{i,j}}\ d\hat{\Omega}'.\end{aligned} \tag{4.11}$$

In order to continue with the computation we need information on how a specific RTM handles the discrete representation of the atmosphere, which may vary drastically between RTMs. For example, one RTM may assume the atmosphere is homogeneous within each grid cell, while another performs linear interpolation between grid cells. Thus to remain implementation agnostic for now, we define a response function, $R(\vec{r})$, such that,

$$R(\vec{r}) = \frac{\partial k(\vec{r})}{\partial k_{i,j}}. \tag{4.12}$$

As an example of how the response function can be realized in practice, in most RTMs the continuous representation of extinction can be expressed in the form,

$$k(\vec{r}) = \sum_i \sum_j k_{i,j} R_j(\vec{r}), \tag{4.13}$$

where $R_j(\vec{r})$ is the corresponding basis function of grid cell j. If this is the case then from Eq. (4.12) we see that the response function is equivalent to the basis function for that

specific grid cell. For an RTM which assumes homogeneous spherical shells, the basis function would be a constant within that cell. However, if an RTM represents the atmosphere as a piecewise linear function specified at spherical shells then the response function may be a linear decreasing function peaked at the center of a specific shell.

With the definition of the response function, we can also calculate,

$$\frac{\partial k_{\text{scat}}(\vec{r})}{\partial k_{i,j}} = \frac{k_{\text{scat},i}(\vec{r})}{k_i(\vec{r})} R(\vec{r}), \tag{4.14}$$

and the derivative of the average phase function,

$$\frac{\partial \overline{p}(\vec{r}, \hat{\Omega}', \hat{\Omega})}{\partial k_{i,j}} = \frac{k_{\text{scat},i}(\vec{r})}{k_i(\vec{r})} \frac{R(\vec{r})}{k_{\text{scat}}(\vec{r})} (p_i(\vec{r}, \hat{\Omega}', \hat{\Omega}) - \overline{p}(\vec{r}, \hat{\Omega}', \hat{\Omega})), \tag{4.15}$$

note that both of these quantities are explicitly dependent on the species i. Lastly, for optical depth,

$$\frac{\partial \tau(s_0, s_1)}{\partial k_{i,j}} = \int_{s_0}^{s_1} R(s)\, ds. \tag{4.16}$$

Combining Eqs. (4.10) and (4.11) the partial derivative of the source function simplifies to,

$$\begin{aligned} \frac{\partial J(\vec{r}, \hat{\Omega})}{\partial k_{i,j}} = J_{\text{sun}}(\vec{r}, \hat{\Omega}) \Bigg[& - \int_{\text{sun}}^{\vec{r}} R(s)\, ds \\ & + \frac{k_{\text{scat},i}(\vec{r})}{k_i(\vec{r})} \frac{R(\vec{r})}{k_{\text{scat}}(\vec{r}) \overline{p}(\vec{r}, \hat{\Omega}_{\text{sun}}, \hat{\Omega})} p_i(\vec{r}, \hat{\Omega}_{\text{sun}}, \hat{\Omega}) \Bigg] \\ & + k_{\text{scat}}(\vec{r}) \int_{4\pi} \frac{\partial I_{\text{dif}}(\vec{r}, \hat{\Omega})}{\partial k_{ij}} \overline{p}(\vec{r}, \hat{\Omega}', \hat{\Omega})\, d\Omega' \\ & + k_{\text{scat}}(\vec{r}) \int_{4\pi} I_{\text{dif}}(\vec{r}, \hat{\Omega}) p_i(\vec{r}, \hat{\Omega}', \hat{\Omega})\, d\Omega'. \end{aligned} \tag{4.17}$$

Calculating the term $\partial I_{\text{dif}} / \partial k_{i,j}$ exactly would require an iterative solution analogous to the original radiative transfer equation (for an example in the plane parallel case see Spurr (2002)), therefore to find a simple, fast, and approximate solution we completely neglect this term. Contributions from $\partial I_{\text{dif}} / \partial k_{i,j}$ are higher order in k_{scat} and are thus expected to be small. The effects of neglecting this term will be further discussed in later sections. Substituting Eq. (4.17) into Eq. (4.7) results in the final weighting function expression used

in this work,

$$
\begin{aligned}
w(k_{i,j}) \approx & -I(\vec{r}_{\text{end}}, \hat{\Omega}) e^{-\tau(\vec{r}_{\text{end}}, \vec{r}_0)} \int_{s_{\text{end}}}^{0} R(s)\, ds \\
& - \int_{s_{\text{end}}}^{0} \left[\int_{0}^{s} R(s')\, ds' e^{-\tau(s,0)} J(s, \hat{\Omega}) \right] ds \\
& - \int_{s_{\text{end}}}^{0} J_{\text{sun}}(s, \hat{\Omega}) \left[\int_{\text{sun}}^{\vec{r}} R(s')\, ds' \right] ds \\
& + \int_{s_{\text{end}}}^{0} J_{\text{sun}}(s, \hat{\Omega}) \frac{k_{\text{scat},i}(s)}{k_i(s)} \frac{R(s) p_i(s, \hat{\Omega}_{\text{sun}}, \hat{\Omega})}{k_{\text{scat}}(s) \overline{p}(s, \hat{\Omega}_{\text{sun}}, \hat{\Omega})}\, ds \\
& + \int_{s_{\text{end}}}^{0} \frac{k_{\text{scat},i}(s)}{k_i(s)} R(s) \int_{4\pi} I_{\text{dif}}(s, \hat{\Omega}) p_i(s, \hat{\Omega}', \hat{\Omega})\, d\Omega'\, ds,
\end{aligned}
\tag{4.18}
$$

the first three terms are attenuation effects, the second last term is an increase of the single scatter source function, and the last term is an increase of the multiple scatter source function.

It should be noted that the majority of these terms arise from single scatter effects. If we take Eq. (4.18) and set $I_{\text{dif}} = 0$, and $J = J_{\text{sun}}$ we obtain an expression for the single scatter weighting function,

$$
\begin{aligned}
w_{\text{SS}}(k_{i,j}) = & -I(\vec{r}_{\text{end}}, \hat{\Omega}) e^{-\tau(\vec{r}_{\text{end}}, \vec{r}_0)} \int_{s_{\text{end}}}^{0} R(s)\, ds \\
& - \int_{s_{\text{end}}}^{0} \left[\int_{0}^{s} R(s')\, ds' e^{-\tau(s,0)} J_{\text{sun}}(s, \hat{\Omega}) \right] ds \\
& - \int_{s_{\text{end}}}^{0} J_{\text{sun}}(s, \hat{\Omega}) \left[\int_{\text{sun}}^{\vec{r}} R(s')\, ds' \right] ds \\
& + \int_{s_{\text{end}}}^{0} J_{\text{sun}}(s, \hat{\Omega}) \frac{k_{\text{scat},i}(s)}{k_i(s)} \frac{R(s) p_i(s, \hat{\Omega}_{\text{sun}}, \hat{\Omega})}{k_{\text{scat}}(s) \overline{p}(s, \hat{\Omega}_{\text{sun}}, \hat{\Omega})}\, ds.
\end{aligned}
\tag{4.19}
$$

Comparing Eqs. (4.18) and (4.19) we see that the full weighting function expression can be written as the single scatter weighting function with two additional terms,

$$
\begin{aligned}
w(k_{i,j}) = & \, w_{\text{SS}}(k_{i,j}) \\
& - \int_{s_{\text{end}}}^{0} \left[\int_{0}^{s} R(s')\, ds' e^{-\tau(s,0)} J_{\text{dif}}(s, \hat{\Omega}) \right] ds \\
& + \int_{s_{\text{end}}}^{0} \frac{k_{\text{scat},i}(s)}{k_i(s)} R(s) \int_{4\pi} I_{\text{dif}}(s, \hat{\Omega}) p_i(s, \hat{\Omega}', \hat{\Omega})\, d\Omega'\, ds.
\end{aligned}
\tag{4.20}
$$

The first additional term contains attenuation of the diffuse source, and including this term is equivalent to replacing the single scatter source function (J_{sun}) with the full source function

$(J_{\text{sun}} + J_{\text{dif}})$ in Eq. (4.19). The second term represents additional scattering of the diffuse radiance, and can not be included by simple modifications of the single scatter weighting function. Later sections will demonstrate the effects of including these additional terms.

4.4 Implementation in SASKTRAN-HR

4.4.1 Overview

With Eq. (4.18) we have a closed form expression for the weighting functions. As alluded in the previous section, it is critical that these weighting functions are calculated relative to how the specific RTM handles changes in the atmospheric state. Defining the weighting function in terms of the response function provides the framework to handle this, but it is still necessary to find the response function for every location j, $R_j(\vec{r})$. Finding $R_j(\vec{r})$ is the first step of the weighting function calculation and will be discussed in detail in Section 4.4.2.

The second step of the weighting function calculation is performing the line integrals of Eq. (4.18). All quantities inside the integrals of Eq. (4.18) are known or can easily be calculated while the radiative transfer calculation is being done. The approach taken by SASKTRAN-HR is to calculate these quantities during the radiative transfer calculation and cache them. After the radiance calculation is complete, the final line integrals are performed to find the weighting functions.

To summarize, the general flow of the full SASKTRAN-HR radiance and weighting function calculation for a single species, i, is:

1. For every location j, find and store the response function, R_j.
2. Using the set of all the response functions, reconfigure the model to ensure the accuracy of line integration over each response function.
3. Perform the radiance calculation and cache useful quantities that are necessary to calculate $w(k_{i,j})$.
4. Using Eq. (4.18) calculate $w(k_{i,j})$ for every response function.
5. Convert each weighting function to the derivative with respect to number density.

4.4.2 Atmospheric Grids and Ray Tracing

Operating in two-dimensional mode, SASKTRAN-HR constructs a discrete atmospheric grid consisting of altitude and angle in the line of sight direction. Atmospheric constituents are assumed to vary bi-linearly within this plane for the radiative transfer calculation. To perform the required line integration, a ray-tracing step is performed. Ray-tracing in SASKTRAN-HR is done through calculating intersections with a set of geometry primitives (spheres, cones, planes, etc.), currently refraction is neglected by the model. The set of geometry primitives is chosen based on how the atmosphere is specified and represented internally in order to ensure that no information is lost when performing the radiative transfer calculation. For the standard two-dimensional atmosphere mode, the set of geometry primitives consists of both spheres, i.e. the spherical shells of the atmospheric layers, and planes, i.e. the orbit plane.

The first step in the weighting function calculation is for every grid cell, j, find the corresponding response function. The response function is species independent, and can be inferred from the implementation of the discrete atmosphere in SASKTRAN-HR. Figure 4.2 shows a slice of the atmospheric grid inside SASKTRAN-HR. Every intersection is a place where the atmospheric state is specified, and bilinear interpolation is done between the intersections. Shown in color is the response function for a single grid cell labeled by "x". The bold lines represent the bounding geometry primitives of the response function.

Internally, a separate ray-tracer is created containing the set of all geometry primitives for the WFs. This helps to improve computational efficiency since for every WF it is only necessary to evaluate integrals involving R_j between these geometry primitives. An advantage of this approach is that it is not strictly necessary for the grid the WFs are calculated on to match the internal atmosphere grid, which may be desired for some retrieval problems. Under this framework it is possible, for example, to calculate weighting functions for a two dimensional atmosphere even when the internal model atmosphere is one dimensional.

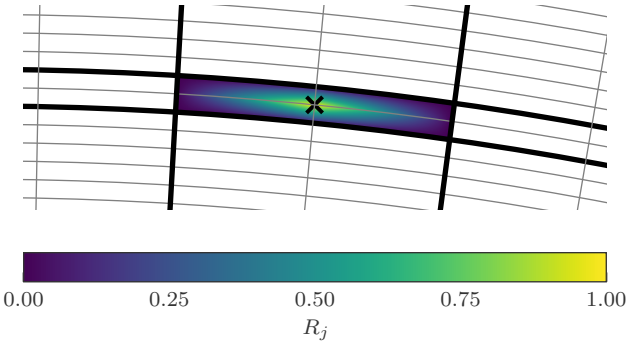

Figure 4.2: The response or basis function in SASKTRAN-HR for the atmospheric grid cell labeled by "x". Intersections between the gray lines represent discrete locations in which the atmospheric state is specified. The bold black lines are the bounding geometry objects for this response function.

4.4.3 Performing the Calculation

Care is taken to evaluate all line integrals as close as possible to how SASKTRAN-HR would evaluate analogous ones in the radiance calculation. For example, the same code is used to calculate $\partial\tau/\partial k_{i,j}$ that is used to calculate τ, except the extinction is replaced with the response function. However, it is not always possible to use identical methods for line integration. When evaluating integrals involving the source function in the radiance calculation, a quadratic fit is applied to J within each grid cell and closed form expressions are used to evaluate the resulting integrals (Zawada et al., 2015). Similar closed form expressions do not exist when evaluating integrals involving $\partial J/\partial k_{i,j}$ in the weighting function calculation. For these cases a Gaussian quadrature scheme is used to evaluate the integrals numerically.

4.4.4 Weighting Functions with Respect to Number Density

Having calculated $w(k_{i,j})$, it is straightforward to calculate,

$$\frac{\partial I}{\partial n_{i,j}} = \sigma_{i,j} w(k_{i,j}), \tag{4.21}$$

where $\sigma_{i,j}$ is the cross section of species i in cell j. It is useful to note that in the case of purely absorbing species ($k_{\text{scat},i} = 0$), the weighting function $w(k_{i,j})$ only depends on the response function and is independent of the actual species of interest. Therefore weighting functions for any number of purely absorbing species can be calculated simultaneously as long as they

share the same response function. In general any RTM which assumes homogeneous shells or uses linear interpolation between grid points will have the same response function for every species, but this may not be true for more involved interpolation schemes.

4.5 Performance and Discussion

4.5.1 Comparisons to Perturbation Methods

Methodology

The following sections analyze the performance of the analytical weighting functions calculation (AL) by comparing with perturbation methods for a few test cases. The atmosphere is specified by a uniform grid in altitude and angle along the line of sight plane, with 0° being the tangent point and increasing away from the instrument. The grid spacing used is 1 km in the vertical ranging from 0 to 100 km, and 1° in the horizontal from $-10°$ to 10°. Weighting functions are calculated on the same grid that the atmosphere is specified on to allow for direct comparisons to perturbation methods. We calculate the perturbation methods with a forward difference scheme,

$$w(n_{i,j}) = \frac{I(n_{i,j} + \Delta n_{i,j}) - I(n_{i,j})}{\Delta n_{i,j}}, \tag{4.22}$$

where here $n_{i,j}$ is the number density of a specific species, i, in a single atmospheric grid cell, j. The perturbation of number density, $\Delta n_{i,j}$, is chosen to be 0.1% of the number density within each cell. Through testing it was found that values smaller than this do not noticeably change the weighting functions and have the potential to introduce numerical instability. The perturbation calculation is performed twice, first with the model set to calculate 50 orders of scatter (MS-P), and then again with the model in single scatter mode (SS-P). The MS-P method is considered to be the correct answer, while the SS-P method is a common simplifying assumption made in the context of retrieval problems.

Weighting functions from the SS-P approximation may be improved by considering the relative weighting function,

$$w_{\text{rel}}(n_{i,j}) = \frac{d \log I}{d \log n_{i,j}} = \frac{n_{i,j}}{I} \frac{dI}{dn_{i,j}}. \tag{4.23}$$

The normalization by the radiance cancels some of the errors associated with the single scattering approximation while the number density normalization is included to make the weighting functions unitless. The AL weighting functions are normalized by the full multiple scatter radiance.

All comparisons use the same model atmosphere containing Rayleigh scatterers, ozone, and sulfate aerosol. To simplify the subsequent discussion, we will use a model atmosphere which only varies one-dimensionally (in altitude), even though the RTM's atmosphere is two-dimensional. The ozone and stratospheric aerosol profiles are tropical zonal means derived from a climatology based on the OSIRIS 5.07 data product (Bourassa et al., 2007; Degenstein et al., 2009) and are shown in Fig. 4.3. Aerosols in the model are assumed to be Mie scatterers using a log-normal particle size distribution with a mode radius of 80 nm and a mode width of 1.6 and an index of refraction of sulfuric acid. Ground reflection is assumed to be Lambertian with an albedo of 1 (perfectly reflecting). Ground reflection manifests in the $\partial I_{\text{dif}}/\partial k_{i,j}$ term which is neglected in the analytical calculation. Therefore an albedo of 1 is a worst case comparison. Comparisons are done for several solar angles which are defined in Fig. 4.1.

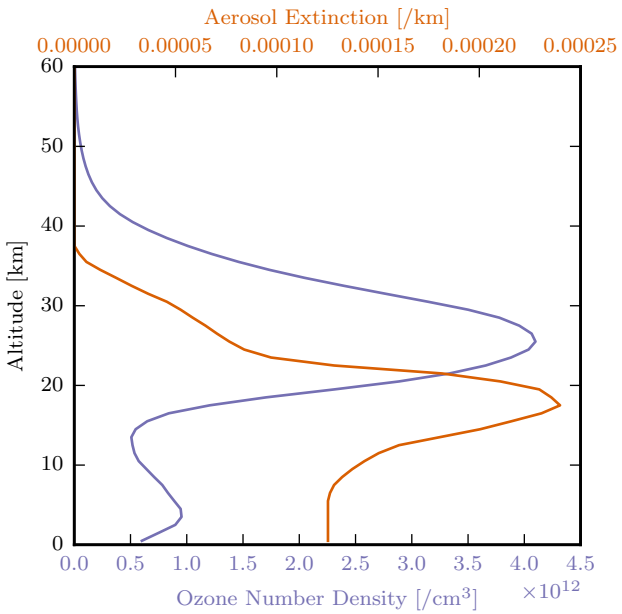

Figure 4.3: Vertical profiles of ozone number density and aerosol extinction used for comparisons.

Weighting Functions For Ozone

For the first test case we look at two-dimensional ozone weighting functions in both the UV and VIS spectral regions. As seen in Section 4.4.4, the majority of the analytic WF calculation is largely independent of the species itself. Therefore comparisons for ozone weighting functions are representative of all purely absorbing species at these wavelengths and atmospheric state. Figure 4.4 shows example two dimensional weighting functions calculated for a 25.5 km line of sight, solar zenith and azimuth angles of 60° and 90° respectively, and at a variety of wavelengths with the MS-P method. For wavelengths where the line of sight optical path is thin (330 nm and 600 nm) the sensitivity is largest at the tangent point and is greater in magnitude on the instrument side of the line of sight, which is expected for absorption effects. When the line of sight optical path is thin the majority of the signal originates near the tangent point where the limb path length is longest. Adding ozone on the near side of the line of sight will attenuate this signal, while adding ozone on the far side will not, resulting in the observed asymmetry. The increasing sensitivity as we approach the tangent point along the line of sight is a direct effect of the limb path length through each cell increasing.

When the atmosphere is not optically thin, the largest sensitivity occurs between the tangent point and the observer. As the wavelength becomes shorter the ozone cross section increases and the area of maximal sensitivity moves towards the instrument. In all cases there is also broad sensitivity above the line of sight, representing attenuation of the incoming solar beam.

At 310 nm and 320 nm we observe significant attenuation originating from beneath the line of sight. Here the additional absorption primarily attenuates the signal originating from the Lambertian surface and scattering into the line of sight and is a higher order effect which is picked up in the MS-P calculation. At 290 nm and 300 nm the atmosphere is too optically thick to see the ground and the effect cannot be observed, while at 330 nm and 600 nm the atmosphere is too optically thin for the additional relative change in absorption to attenuate the ground.

Next we perform a systematic comparison of the AL weighting functions to those calcu-

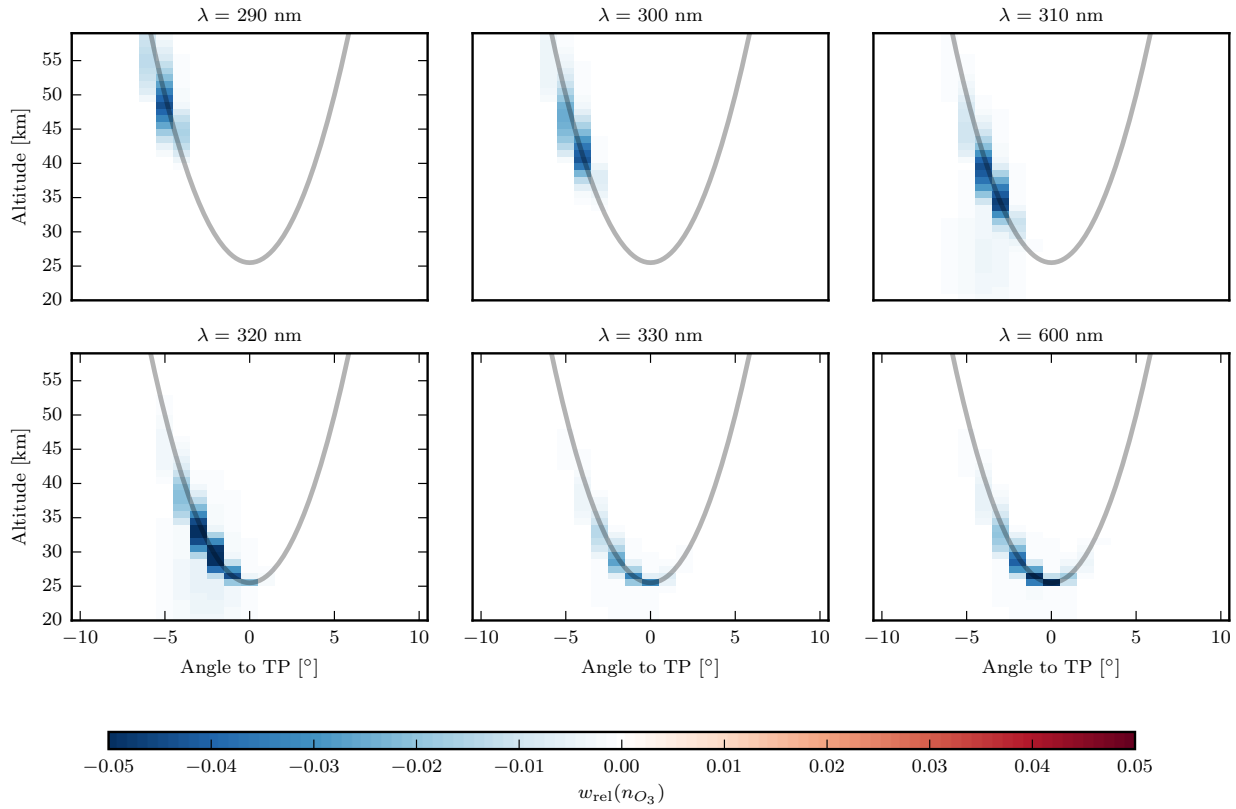

Figure 4.4: Relative ozone weighting functions using the MS-P method for a 25.5 km line of sight at several wavelengths. For this calculation a solar zenith angle of 60° and a solar azimuth of 90° was used (single scatter angle of 90°).

lated with perturbation methods. We focus our comparisons on two wavelengths: 310 nm where at low tangent altitudes the line of sight path is optically thick, and 600 nm where the line of sight path is generally optically thin. Figure 4.5 shows the absolute difference of the relative AL weighting functions compared to the SS-P and MS-P methods, as well as the reference MS-P weighting function. Results are shown for varying tangent altitudes and wavelengths, and with solar conditions of $\theta = 40°$, $\phi = 0°$. In general there is good agreement between the AL and SS-P WFs, which suggests that the radiance normalization done in the SS-P calculation is roughly equivalent to the inclusion of the extra attenuation term in Eq. (4.20). Small differences between the AL and SS-P weighting functions are observed in optically thick scenarios, which will be quantified later.

There are also differences observed between the AL and MS-P weighting functions on the order of 10% of the maximum value, however most of these differences are from altitudes

below the line of sight near the ozone peak. The MS-P WFs show higher sensitivity primarily below the area of maximal sensitivity due to the inclusion of higher scatter order effects in the calculation. The scatter path for these terms is dominated by ground to line of sight, and the neglected $\partial I_{\text{dif}}/\partial k_{ij}$ term in the AL weighting function contains attenuation of the ground to line of sight ray. The differences between the methods are larger at 310 nm than at 600 nm. For the used atmospheric state and viewing conditions the ground to line of sight path is generally optically thin at 600 nm, thus relative increases in the ozone profile have small effects on the radiance. However at 310 nm there is significant attenuation of the ground to line of sight path by ozone, therefore relative increases in the ozone profile have a significant effect on the upwelling signal and hence the observed radiance.

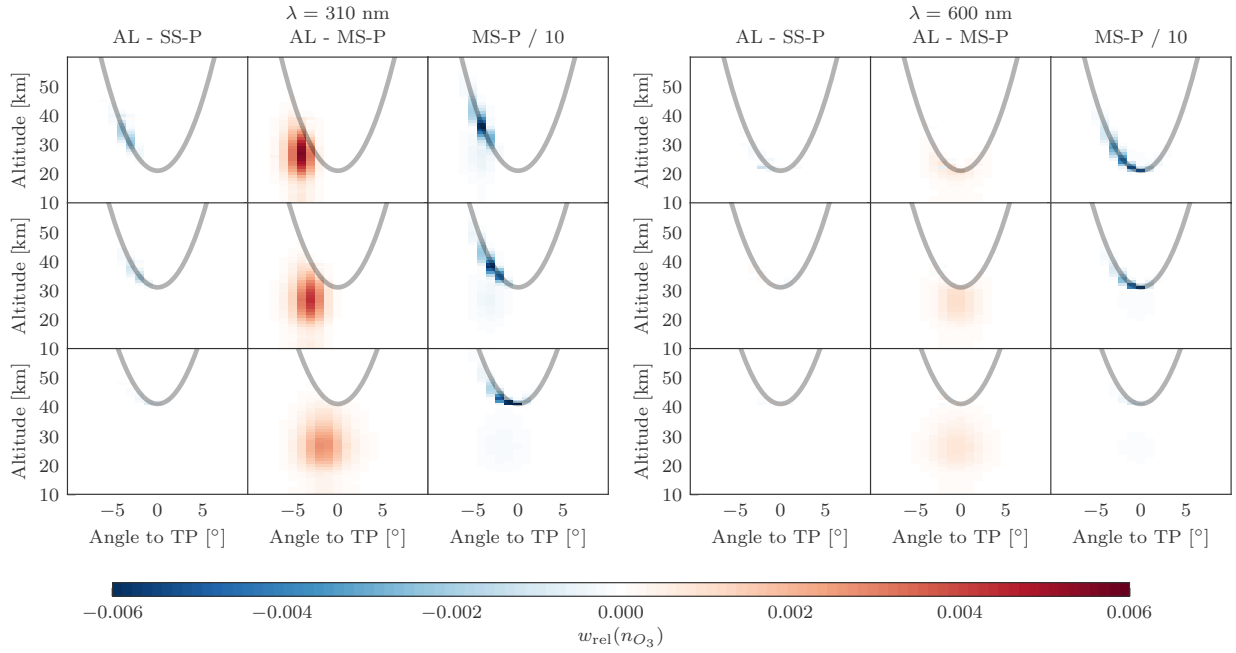

Figure 4.5: Relative weighting functions for a variety of wavelengths and tangent altitudes with a solar zenith angle of 40° and a solar azimuth angle of 0° ($\Theta = 50°$). The left panel is for a wavelength of 310 nm, while the right panel is for a wavelength of 600 nm. Each row represents a line of sight (gray line) with a different tangent altitude with the top row at 20.5 km, the middle row at 30.5 km, and the bottom row at 40.5 km. Within each panel, the first column shows the difference between the AL and SS-P WFs, the middle column the difference between the AL and MS-P WFs, and the right most column the MS-P WFs (divided by 10 for scale).

Since the observed differences arise due to attenuation of upwelling effects, we expect differences to depend on the solar geometry.

To examine the agreement between the MS-P and AL WFs systematically in optically thick conditions as a function of solar condition, we take the AL relative weighting functions at 310 nm for a set of lines of sights with tangent altitudes ranging from 0.5 km to 30.5 km in steps of 1 km. We then create a scatter plot of each of these values compared to the corresponding value calculated by the MS-P method. For reference, the same comparison is also done for the SS-P weighting functions relative to the MS-P weighting functions. The process is performed for a set of varying solar zenith and azimuth angles, and the results are shown in Fig. 4.6. The slope of the resulting correlation line is an approximate measure of bias and the R^2 value is a metric for agreement of shape of the weighting functions.

The agreement between the AL and MS-P WFs sharply depends on solar zenith angle. At low solar zenith angles where there is a large upwelling signal the agreement is worse (slopes of 0.91–0.93 at $\theta = 20°$) compared to high solar zenith angles (slopes of 1.0 at $\theta = 85°$), which is as expected. There is a weak dependence on solar azimuth angle, likely a direct consequence of the balance of the single scatter and multiple scatter source terms as a function of solar scattering angle. The AL WFs perform significantly better than the SS-P WFs in these optically thick conditions, most noticeably at large values which are indicative of being along the line of sight. Examples of these differences were seen previously in Fig. 4.5.

It should be noted that situations where the AL and MS-P WFs differ are typically situations that are explicitly ignored in many retrieval algorithms. For example, it is common to only allow each limb measurement to only influence profiles at, or above, its tangent altitude, and also to filter optically thick scenarios. With these constraints implemented there would only be negligible differences between the weighting functions for all three techniques. Furthermore, all comparisons shown were done with a ground albedo of 1, which is the worst case scenario. For these reasons we expect that the AL weighting functions presented will be suitable for two-dimensional retrieval applications and perform similary to those calculated with a single-scatter approximation.

Aerosols

For the second test case we examine two-dimensional weighting functions for stratospheric aerosols at 750 nm. It is well known (e.g. Bourassa et al., 2007; Taha et al., 2011) that

in backscatter cases or at high aerosol optical depths, weighting functions for aerosols may undergo a sign change. At high altitudes adding aerosol to the atmospheric state will increase the observed radiance, in contrast at low altitudes adding aerosol decreases the observed radiance.

Figure 4.7 shows the two dimensional aerosol weighting function calculated with three different methods for a 10.5 km line of sight, solar zenith angle of 60°, and in both back-scatter ($\Theta = 150°$) and forward-scatter ($\Theta = 30°$) cases. In the forward scatter case all three weighting functions have similar shape, with the single scatter weighting function being slightly lower in magnitude. In the back-scatter case the single scatter weighting function has a completely different structure to the other two methods.

In contrast with weighting functions for purely absorbing species, these weighting functions appear to be symmetric around the tangent point. Once again, this is explained by noting that the atmosphere is optically thin under these conditions. Since there is very little attenuation along the line of sight, adding signal on the near side or the far side is essentially the same. However as the weighting function also contains attenuation effects (negative terms in Eq. (4.18)) which are asymmetric, the observed symmetry indicates that the scattering terms (positive terms in Eq. (4.18)) far outweigh the attenuation terms.

For scattering species there is a balance between attenuation effects and scattering effects. Attenuation effects are primarily on the near side of the instrument, since the majority of the signal is either at or between the tangent point and the observer. However, in a relatively thin atmosphere (as is the case here at 750 nm) scattering effects are relatively symmetric around the tangent point. For the single scatter calculation, all scattering effects in the weighting function are from the single scatter source function. In backscatter the single scatter source function is relatively small owing to the Mie phase function, and we can directly see attenuation effects dominate between the tangent point and the observer and scattering effects dominate on the other side. In the forward scatter case the single scatter source is large and we do not see the same sign change.

Figure 4.8 shows the absolute differences between the different methods for the same geometry. It can be seen that the single scatter weighting function overestimates in the forward scatter case, and underestimates in the backscatter case. In the forward scatter

case the overestimation occurs through the normalization by I_{SS}, suggesting that the relative contribution to the total radiance due to aerosol is larger for the first order of scatter than the second. Even though there is a large difference in the value of the weighting function, looking back at Fig. 4.7 we see that the relative error is not that large and there is still good qualitative agreement. In the backscatter case the underestimation suggests that the relatively the aerosol contribution to the radiance is larger for higher orders of scatter. Unlike the forward scatter case, from Fig. 4.7 we know that the underestimation completely changes the shape of the WFs and there is no longer qualitative agreement to the MS-P WFs.

On the other hand the AL WFs agree almost perfectly with the MS-P ones. The maximum error error relative to the MS-P value at the tangent point is 0.88% in the forward scatter case, and 3.5% in the backscatter case, in contrast with corresponding values of 24.8% and 127% for the SS-P WFs. The lack of observed differences suggests that the $\partial I_{\mathrm{dif}}/\partial k_{i,j}$ term, which is neglected in the AL calculation, has minimal effect on aerosol WFs under these conditions. Since the AL WFs can be written in terms of the SS-P WFs with additional terms, we conclude that the inclusion of the positive term in Eq. (4.20) greatly improves the WF calculation in backscatter conditions for aerosol.

To examine the agreement between the MS-P and AL WFs systematically as a function of solar condition, results are shown in a scatter plot similar to Fig. 4.6. Once again, the AL and SS-P relative weighting functions are taken for a set of line of sights with tangent altitudes ranging from 0.5 km to 30.5 km in steps of 1 km are scattered against the corresponding value calculated by the MS-P method. The procedure is done at 750 nm and the results are shown in Fig. 4.9.

In the close to forward scatter cases ($\phi = 0°$) the SS-P method agrees well in both magnitude and shape with the MS-P method. In the side scatter case ($\phi = 90°$) the SS-P weighting functions still agree well in shape, but are systematically low compared to the MS-P ones. Lastly, in the backscatter cases ($\phi = 180°$) the SS-P method does not agree well in magnitude or shape with the MS-P values.

The single scatter calculation is biased due to the relative contributions of the single scatter and multiple scatter source terms. High solar zenith angles allow for more extreme backscatter conditions, reducing the single scatter source function. On the other hand,

low solar zenith angles increase the amount of upwelling radiation, increasing the multiple scatter source function. Therefore it is expected that the single scatter weighting functions will perform worst at mid solar zenith angles, which can be observed in Fig. 4.9. For all solar azimuth angles the worst conditions for the SS-P method in both magnitude and shape are at $\theta = 40^\circ$ or $\theta = 60^\circ$.

In all cases the AL weighting functions agree very well with the MS-P weighting functions. The worst slope is 0.994 and the worst R^2 value is 0.999 in contrast with the SS-P values which have a worst slope of 0.376 and R^2 value of 0.891. The agreement for the AL WFs is consistent across all solar conditions. The AL WFs appear to perform excellently for species dominated by scattering effects, and are of higher quality than those calculated with a single scatter approximation.

Since the agreement between the AL and MS-P WFs is in general better for scattering aerosols compared to absorbing species we also expect that the AL WFs will be suitable for two-dimensional retrieval applications. The observed disagreement between the SS-P and MS-P WFs in backscatter cases provides evidence that SS-P WFs may not be suitable for limb retrievals in backscatter cases.

4.5.2 Timing

Here we present timing estimates for the analytical weighting functions relative to perturbation methods. We consider of a calculation at a single wavelength with N lines of sight (or equivalently, measurements) and M grid cells. Both perturbation methods scale almost perfectly linearly with M as each additional grid cell requires an additional radiative transfer calculation with the atmospheric state perturbed at that location. However in actuality, the cost of performing a full radiative transfer calculation also increases with M, causing the scaling to be slightly worse than linear. Let $\mathcal{T}_0(N, M)$ denote the cost of performing the baseline radiative transfer calculation, then by definition the cost of calculating the weighting function for the multiple scatter perturbation method will be,

$$\mathcal{T}_{MS}(N, M) = (M + 1)\mathcal{T}_0(N, M), \tag{4.24}$$

where the +1 term is for the required baseline radiative transfer calculation. The quantity $\mathcal{T}_{MS}(N,M)/\mathcal{T}_0(N,M)$ will be perfectly $\mathcal{O}(M)$ and can be interpreted as the time required to calculate WFs relative to the radiance calculation. All timing comparisons will be done using this relative quantity rather than the absolute computational time.

Figure 4.10 shows the scaling of the weighting function calculation for four different methods relative to the baseline radiative transfer calculation. The four methods shown are the two perturbation methods: SS-P and MS-P, and also two variations of the AL method: AL with scattering and AL without scattering. The primary difference between the AL method with and without scattering is the inclusion of the last term in Eq. (4.18), which involves integrating the diffuse radiance over the unit sphere at every grid point along the line of sight. For purely absorbing species we do not have to calculate this term, offering a factor of 2–5 speed increase depending on the conditions. As previously mentioned in Section 4.3.2, for absorbing species the AL calculation is equivalent to the single scatter calculation with the single scatter source function replaced with the multiple scatter source function. Since both of these quantities are simply cached and looked up, the AL without scattering calculation takes approximately the same time as a single scatter analytic calculation would.

The left panel of Fig. 4.10 shows the relative timing for a calculation involving 100 lines of sight as a function of M, and the right panel shows the relative timing for 2000 grid cells as a function of the number of lines of sight N. Both MS-P and SS-P scale approximately linear with the number of grid cells, however the AL methods appear to have better than linear scaling. Through the implementation we expect $\mathcal{T}_{AL}$ to be $\mathcal{O}(M)$, however since $\mathcal{T}_0$ also increases with M we obtain better than linear scaling. Even at small numbers of grid cells, the analytical calculation is more than an order of magnitude faster than the single scatter perturbation calculation, and more than two orders of magnitude faster than the multiple scatter method.

The analytical methods have relatively worse scaling with respect to the number of lines of sight. As expected from the algorithm implementation, we obtain perfect linear scaling for large numbers of lines of sight for the AL method. The MS method scaling is, by definition, flat. The SS method is flat for low numbers of lines of sight but begins to increase slowly for N greater than 100. For very large N (~ 1000) the AL method is still more than an order

of magnitude faster than the SS-P method.

The observed speed difference between the AL and SS-P methods may seem odd considering the AL method essentially calculates the single scatter WF with some additional terms. There are two reasons for this difference, the first is due to the configuration stage in SASKTRAN-HR. Every time the atmosphere is changed (e.g. a perturbation for the forward difference method) the model must be reconfigured which has a significant overhead. In theory, a special mode could be created to minimize the configuration overhead for weighting function calculations, however no effort has been made to implement this in SASKTRAN-HR. The second reason for the timing discrepancy is a fundamental advantage by calculating the derivative directly rather than with a perturbation method. Take for example, the calculation of a single weighting function with respect to $k_{i,j}$. The AL calculation will inevitably involve integrals $\partial\tau/\partial k_{i,j} = \int R_j$. In the SS-P calculation, analogous terms will be $\tau = \int k + \Delta k_{i,j}$. Since R_j is 0 everywhere except for the region of interest, the integral in the AL calculation is faster to perform than the analogous one of the SS-P calculation. In general, perturbation methods involve many unnecessary calculations which are not done by the AL method.

One of the goals of this work was to implement a two-dimensional weighting function calculation which is computationally efficient enough to use in a two-dimensional retrieval. Currently the operational instrument with the best along track (horizontal) resolution is OMPS-LP, reporting a vertical image of the atmosphere with approximately 1 km vertical resolution every 19 s ($\sim 1^\circ$ along track) (Flynn et al., 2004). If the retrieval grid was set up to match this, a hypothetical two-dimensional retrieval grid could have 100 grid points in the vertical, and 20 grid points in the horizontal resulting in 2000 total grid points. From Fig. 4.10 we see that a calculation with 100 lines of sight and 2000 grid points takes approximately the same time as the baseline radiative transfer calculation. Thus in this hypothetical retrieval, the same amount of time would be spent calculating weighting functions as calculating the radiance. We conclude that the implemented AL weighting function calculation is suitable for two-dimensional retrievals for instruments with similar resolutions to OMPS-LP.

4.6 Conclusion

The ability to analytically calculate approximate weighting functions where the atmosphere varies in both altitude and angle along the line of sight has been implemented into the SASKTRAN-HR radiative transfer model. The method is based upon direct calculation of the derivative of the radiative transfer equation in integral form while neglecting terms high order with respect to the scattering extinction. The analytical weighting functions were compared against weighting functions calculated with both multiple scatter and single scatter perturbation methods. For absorbing species the analytical weighting functions are as accurate, but not significantly better, than those calculated with a single scatter approximation. In all tested cases the analytical weighting functions for stratospheric aerosol agree with those from multiple scatter perturbation better than the single scatter perturbation weighting functions. The analytical method was found to be orders of magnitude faster than the perturbation methods for a variety of numbers of lines of sight and atmospheric grid cells.

Acknowledgements

We would like to thank the Canadian Space Agency and the Natural Sciences and Engineering Research Council of Canada for providing funding for this project. We are also grateful for the helpful comments of three anonymous referees that helped improve the manuscript.

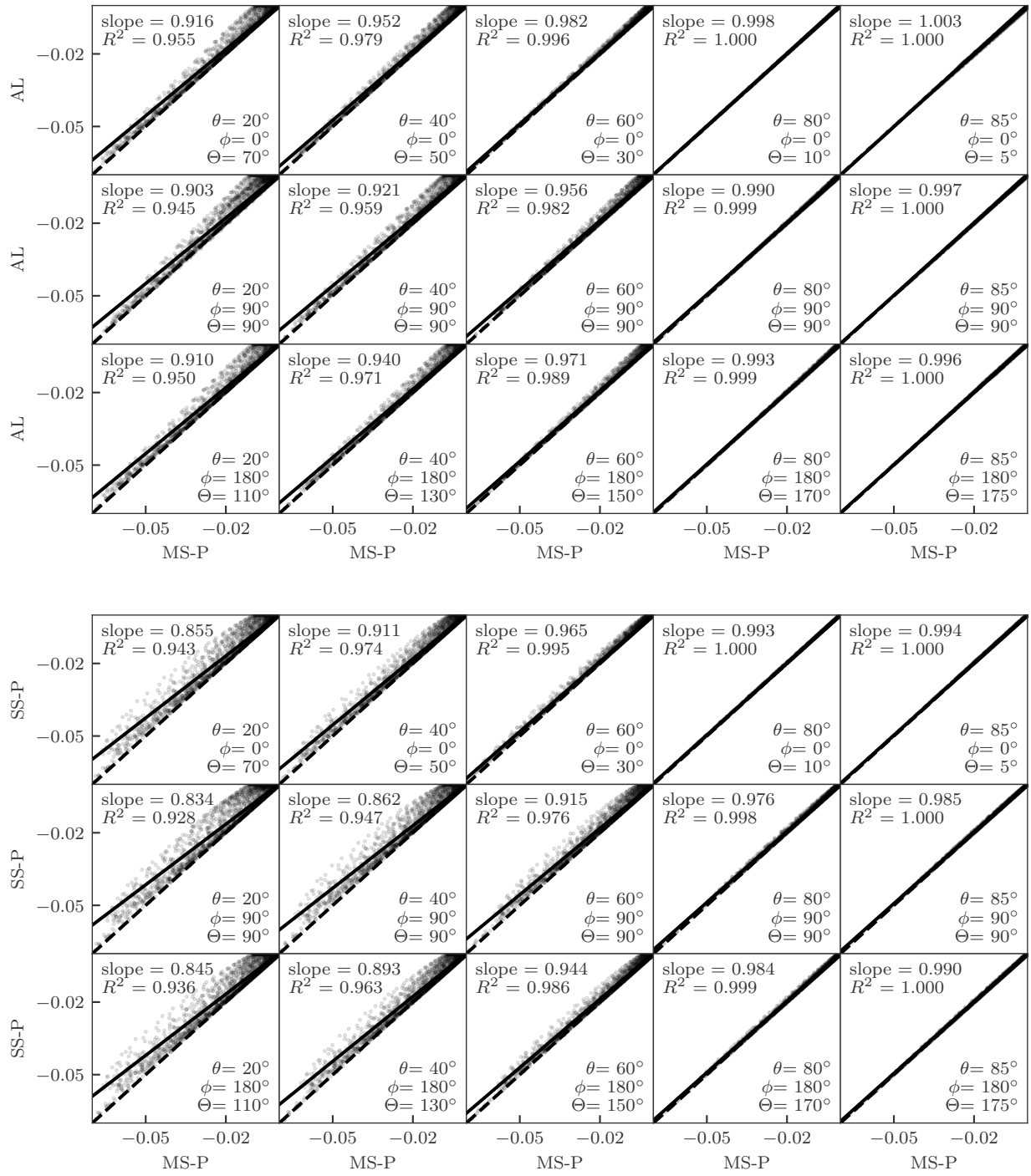

Figure 4.6: Comparison of the three methods for a large variety of solar conditions at 310 nm. For the top panel, each frame is a scatter plot at a specific solar condition (θ, ϕ, Θ) of the WFs for tangent altitudes ranging from 0.5 to 30.5 km in steps of 1 km for the AL method against the MS-P method. The slope and R^2 value of the resulting best fit line are provided on each frame for reference. The bottom panel is the same except for the SS-P method instead of the AL method.

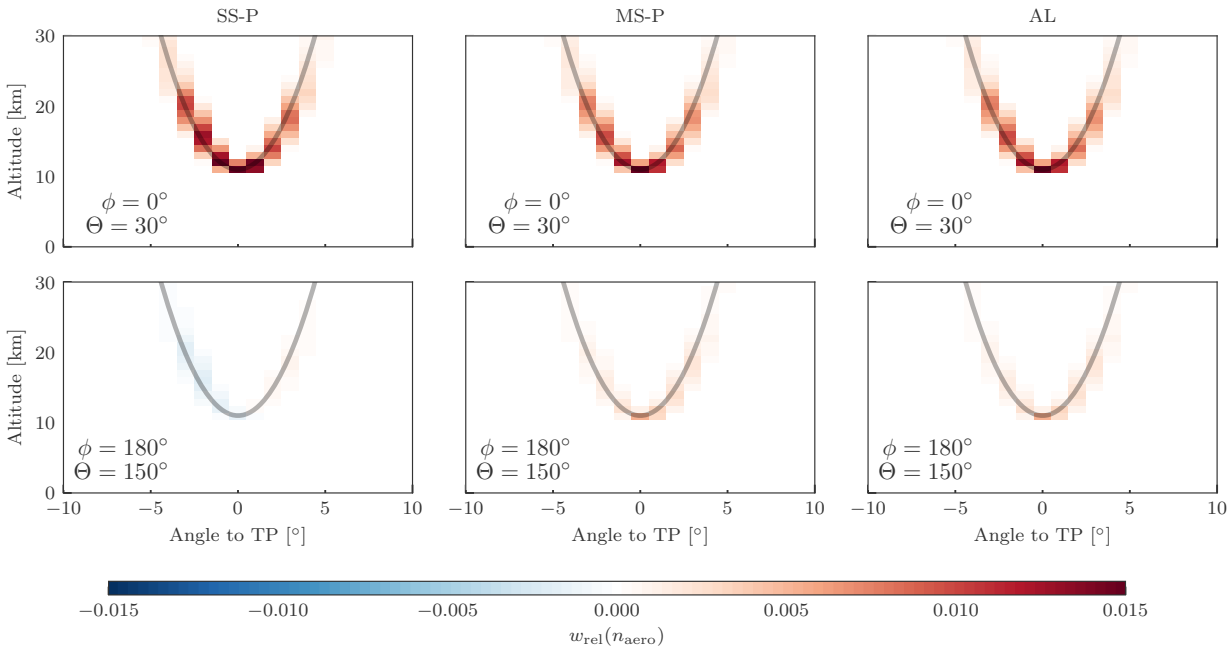

Figure 4.7: Two dimensional weighting function for a 10.5 km line of sight (gray line) with respect to aerosol number density calculated with the SS-P method (first column), the MS-P method (second column), and the AL method (third column). The first row is for a forward scattering geometry ($\phi = 0°$, $\Theta = 30°$) while the second row is for a backscatter geometry ($\phi = 180°$, $\Theta = 150°$).

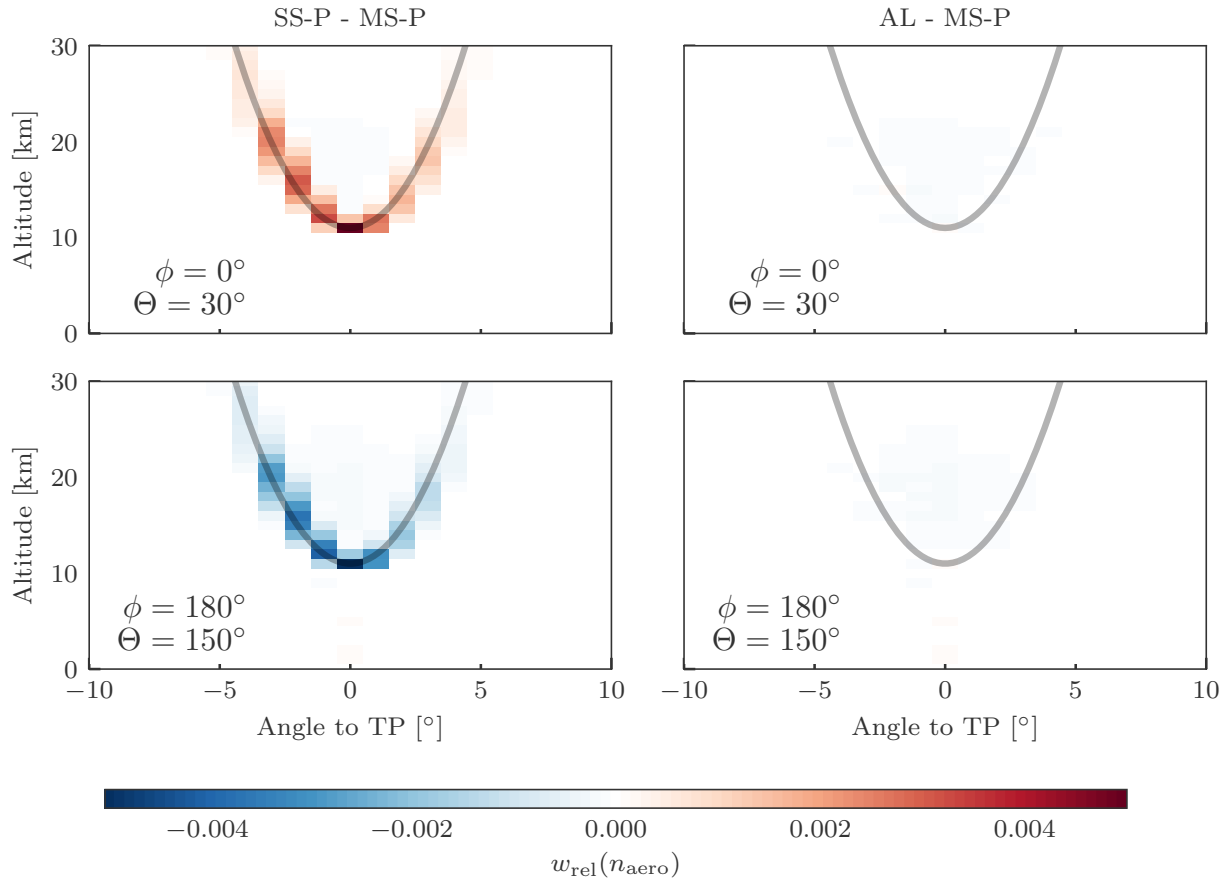

Figure 4.8: Absolute differences in the relative weighting functions shown in Fig. 4.7 for the AL (first column) and SS-P (second column) methods compared to the MS-P method. The first row is for a forward scattering geometry ($\phi = 0°$, $\Theta = 30°$) while the second row is for a backscatter geometry ($\phi = 180°$, $\Theta = 150°$).

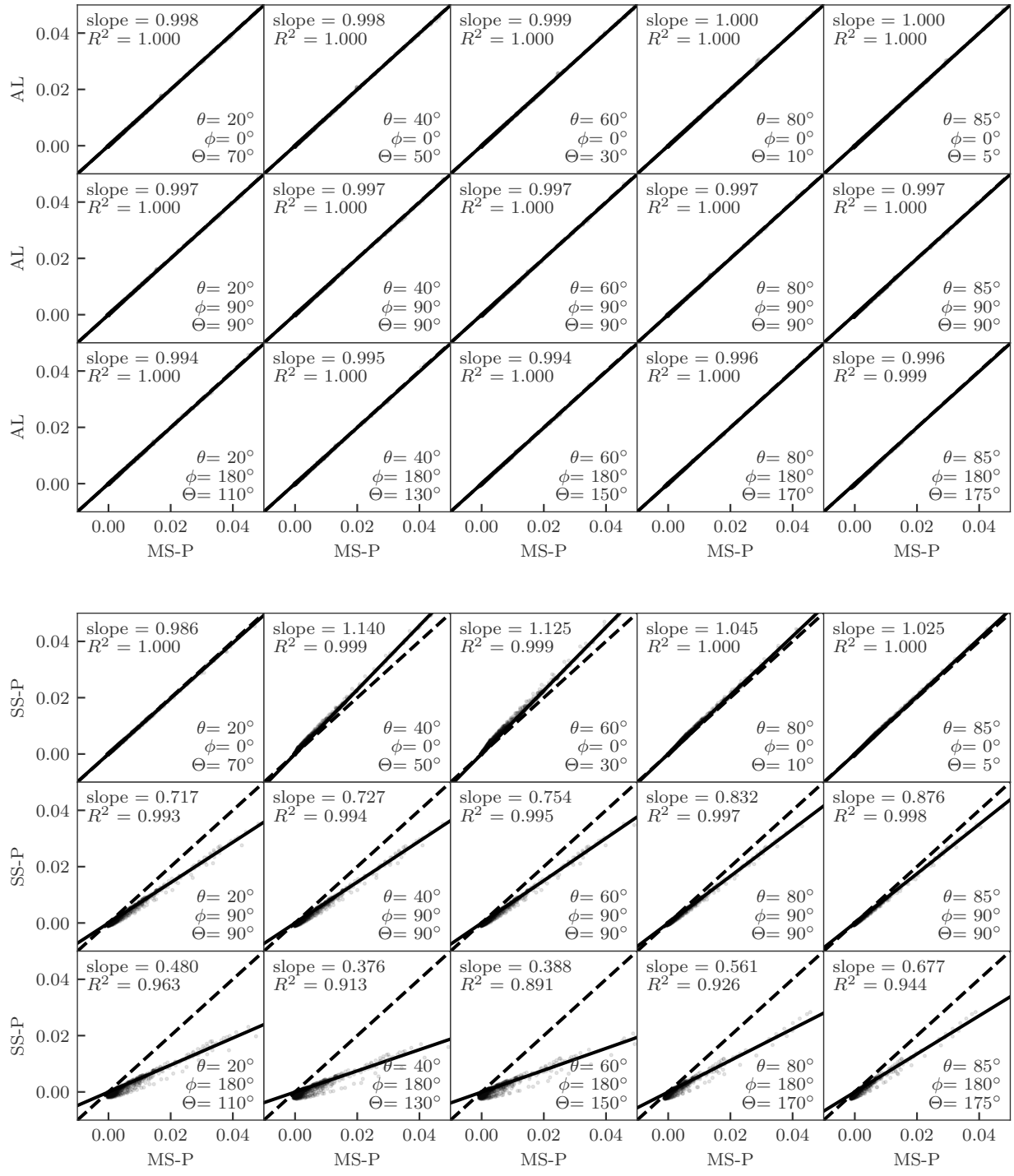

Figure 4.9: Same as Fig. 4.6 except for stratospheric aerosols at 750 nm.

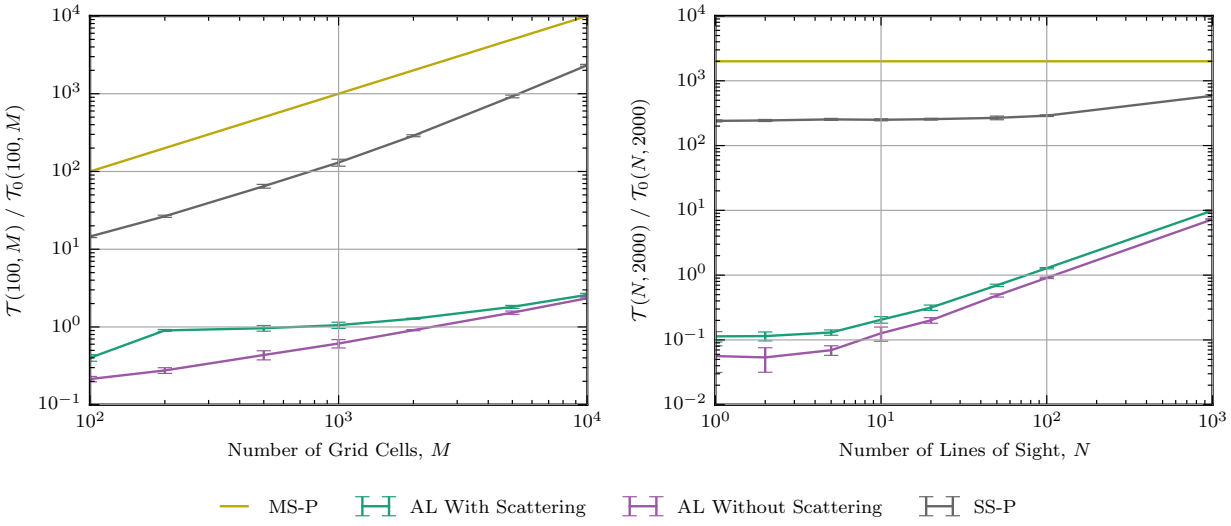

Figure 4.10: Time spent calculating the weighting function for N lines of sight and M grid cells relative to a baseline full multiple scatter radiance calculation. A value of 1 indicates that the full weighting function calculation took the same amount of time as the radiance calculation. The left panel shows the scaling of four different methods as a function of the number of grid cells, and the right panel shows the scaling as a function of number of lines of sight. The vertical error bars represent 2σ of the timing measurements.

Chapter 5

Tomographic Retrievals of Ozone with OMPS-LP: Algorithm Description and Preliminary Results

D. J. Zawada, L. A. Rieger, A. E. Bourassa, D. A. Degenstein

Having the two-dimensional radiative transfer model of Chapter 3 and the efficient Jacobian calculation of Chapter 4, it is now possible perform the main objective of the thesis, the tomographic retrieval. This manuscript details the development of a tomographic retrieval algorithm for ozone from limb scatter measurements from OMPS-LP. Included is a description of the algorithm, simulation results showing improvement over a conventional one-dimensional retrieval, and preliminary validation results.

A byproduct of the manuscript is a publicly available, full mission dataset, of ozone values retrieved by OMPS-LP. The dataset has been used in the creation of both the SAGE-CCI-OMPS (Sofieva et al., 2017) merged time series, and the SAGE-OSIRIS-OMPS time series based on a modification of the SAGE-OSIRIS time series of Bourassa et al. (2014). These datasets have been used in several studies (Ball et al., 2018; Steinbrecht et al., 2017) and are a part of the Stratosphere-troposphere Processes And their Role in Climate Long-term Ozone Trends and Uncertainties in the Stratosphere (LOTUS) activity. Stratospheric ozone trend results from LOTUS are intended to be used in the 2018 World Meteorogical Association ozone assessment.

The development of the two-dimensional retrieval, performing the analysis, and authoring the manuscript was performed by myself. The one-dimensional retrieval that was used as a comparison was performed with the assistance of L. A. Rieger.

This manuscript has been published in Atmospheric Measurement Techniques, and unless otherwise stated the version presented here is unchanged. The layout of figures and equations and the format of cross references has been modified to match that of the overall document.

Zawada, D. J., Rieger, L. A., Bourassa, A. E., & Degenstein, D. A. (2018). Tomographic retrievals of ozone with the OMPS Limb Profiler: algorithm description and preliminary results. *Atmospheric Measurement Techniques*, *11*(4), 2375–2393. doi:10.5194/amt-11-2375-2018

5.1 Abstract

Measurements of limb-scattered sunlight from the Ozone Mapping and Profiler Suite Limb Profiler (OMPS-LP) can be used to obtain vertical profiles of ozone in the stratosphere. In this paper we describe a two-dimensional, or tomographic, retrieval algorithm for OMPS-LP where variations are retrieved simultaneously in altitude and the along-orbital-track dimension. The algorithm has been applied to measurements from the center slit for the full OMPS-LP mission to create the publicly available University of Saskatchewan (USask) OMPS-LP 2D v1.0.2 dataset. Tropical ozone anomalies are compared with measurements from the Microwave Limb Sounder (MLS), where differences are less than 5 % of the mean ozone value for the majority of the stratosphere. Examples of near-coincident measurements with MLS are also shown, and agreement at the 5 % level is observed for the majority of the stratosphere. Both simulated retrievals and coincident comparisons with MLS are shown at the edge of the polar vortex, comparing the results to a traditional one-dimensional retrieval. The one-dimensional retrieval is shown to consistently overestimate the amount of ozone in areas of large horizontal gradients relative to both MLS and the two-dimensional retrieval.

5.2 Introduction

The Ozone Mapping and Profiler Suite Limb Profiler (OMPS-LP) on board the Suomi National Polar-orbiting Partnership (Suomi-NPP) spacecraft began taking routine measurements of limb-scattered sunlight in early April 2012 (Flynn et al., 2006). The limb profiler images the atmospheric limb every 19 s ($\sim$ 125 km along track) from the ground to approximately 100 km using three vertical slits that are separated horizontally by 4.25°. A prism disperser is used to obtain a spectrally resolved signal in the range 290–1000 nm. These spectrally resolved measurements can be inverted with a forward model accounting for multiple scattering to obtain vertically resolved profiles of ozone concentration in the atmosphere.

The standard OMPS-LP ozone product is produced by NASA, and version 1.0 of the retrieval is described in detail by Rault and Loughman (2013b). The NASA retrieval employs the assumption of horizontal homogeneity, treating each vertical image separately to retrieve a one-dimensional vertical profile. However, it is possible to take advantage of the long limb path length and fast sampling capabilities of OMPS-LP to combine multiple images together and retrieve in the orbit track and altitude dimensions simultaneously. These two-dimensional, or tomographic, retrievals have been used successfully in many retrievals from limb emission instruments (e.g., Carlotti et al., 2006; Degenstein et al., 2004; Degenstein et al., 2003; Livesey et al., 2006). A two-dimensional retrieval of NO_2 and OCLO was done for limb scatter measurements from the SCanning Imaging Absorption SpectroMeter for Atmospheric CHartographY (SCIAMACHY; Bovensmann et al., 1999) by Puķīte et al. (2008), and a preliminary two-dimensional retrieval study for ozone using a single-scatter radiative transfer model was also performed by Rault and Spurr (2010) using simulated OMPS-LP measurements. Measurements from OMPS-LP are a natural candidate to attempt a two-dimensional retrieval due to the relatively finely resolved orbital-track sampling ($\sim$ 125 km) compared to other limb scatter instruments; for example, the Optical Spectrograph and InfraRed Imaging System (OSIRIS) (Llewellyn et al., 2004) has $\sim$ 600 km along-track sampling.

In this paper we describe a retrieval algorithm for the central slit of OMPS-LP which accounts for inhomogeneity in the along-orbit direction and present preliminary results. To

the authors' knowledge this is the first two-dimensional limb scatter ozone retrieval applied to real measurements. The algorithm is described in detail in Sect. 5.3. We have applied the algorithm to the entire mission of OMPS-LP, creating a dataset of vertical profiles of stratospheric ozone from early 2012 to present with near-global coverage (University of Saskatchewan (USask) OMPS-LP 2D v1.0.2 dataset). Section 5.6 presents some preliminary results and validation efforts with the dataset. The dataset is compared against the likewise two-dimensional ozone retrievals (Livesey et al., 2006) from the Microwave Limb Sounder (MLS; Waters et al., 2006). Tropical ozone anomalies are compared against those from MLS for the full mission dataset. Lastly, nearly perfectly coincident measurements with MLS are investigated.

5.3 The Retrieval Algorithm

5.3.1 Overview

Here we follow the optimal estimation framework outlined in Rodgers (2000) and use similar notation. The general goal of the atmospheric inverse problem is to find the optimal set of state parameters, $\vec{x}$, given with a set of measurements, $\vec{y}$, and other a priori information or constraints. The vector $\vec{x}$ of length n is often called the state vector, while the vector $\vec{y}$ of length m is called the measurement vector. In our OMPS-LP ozone retrieval case, $\vec{x}$ consists of the logarithm of ozone number density on a two-dimensional grid (altitude and along the orbital track), and $\vec{y}$ contains the logarithm of the spectrum for multiple OMPS-LP images at selected ozone-sensitive wavelengths. A common approach to the inverse problem (Rodgers, 2000) is to minimize the cost function,

$$\chi^2 = [F(\vec{x}) - \vec{y}]^T \mathbf{S}_\epsilon^{-1} [\mathbf{F}(\vec{x}) - \vec{y})] + [\vec{x}_\mathrm{a} - \vec{x}]^T \mathbf{R}^T \mathbf{R} [\vec{x}_\mathrm{a} - \vec{x}], \tag{5.1}$$

where $\mathbf{S}_\epsilon$ is the covariance of the measurement vector, $\mathbf{F}$ is the forward model, $\mathbf{R}$ is a regularization matrix, and $\vec{x}_\mathrm{a}$ is the a priori state vector. A priori information is included through the two quantities R and x_a. Applying a standard Guass–Newton minimization approach to

the cost function results in the iterative step

$$\vec{x}_{i+1} = \vec{x}_i + \left(\mathbf{K}_i^T \mathbf{S}_\epsilon^{-1} \mathbf{K}_i + \mathbf{R}^T\mathbf{R} + \gamma_i \mathbf{I}\right)^{-1} \left[\mathbf{K}_i^T \mathbf{S}_\epsilon^{-1}(\vec{y} - \mathbf{F}(\vec{x}_i)) - \mathbf{R}^T\mathbf{R}(\vec{x}_i - \vec{x}_\mathrm{a})\right], \qquad (5.2)$$

where $\mathbf{K}$ is the Jacobian matrix of the forward model, i is the iteration number, and γ_i is a Levenberg–Marquardt damping parameter. A relatively small Levenberg–Marquardt type term, $\gamma_i = 0.1$ multiplied by the mean value of the diagonal of $\mathbf{K}_i^T \mathbf{S}_\epsilon^{-1} \mathbf{K}_i$, is included to move the solution step closer to that of a gradient descent method, aiding performance when the Gauss–Newton step is outside the linear regime.

Equation (5.2) forms the basis of the retrieval method used in this work. The tomographic, or two-dimensional, nature of the retrieval is encoded in the details of the definitions of the state vector and the measurement vector. The state vector contains information about the atmospheric state for an entire orbit of OMPS-LP and is described in detail in Sect. 5.3.2. A brief description of the forward model, which must account for atmospheric variations along the line of sight, is given in Sect. 5.3.3 and Sect. 5.3.5. The exact form of the measurement vector for ozone and minor retrieved species (stratospheric aerosol and surface albedo) is presented in Sects. 5.3.7 and 5.3.8, respectively. Lastly, the form of regularization and a priori used is given in Sect. 5.3.9.

For this work v2.0–2.4 of the OMPS-LP L1G product (https://ozoneaq.gsfc.nasa.gov/data/omps/, last access: April 2017) is used.

5.3.2 The State Vector

The state vector consists of the logarithm of ozone number density on a discrete grid, referred to as the retrieval grid. The retrieval grid is two-dimensional in altitude and angle along the orbital plane of OMPS-LP, and is shown in Fig. 5.1. The altitude component of the grid is discretized in 1 km steps with lower and upper bounds at the tropopause altitude and 59 km, respectively.

The horizontal spacing of the retrieval grid are chosen to match the horizontal sampling of OMPS-LP, which is approximately 125 km. A consequence of the OMPS-LP viewing geometry is that measurements with a higher tangent point are closer to the instrument than measurements with a lower tangent point. For convenience the absolute locations of the hor-

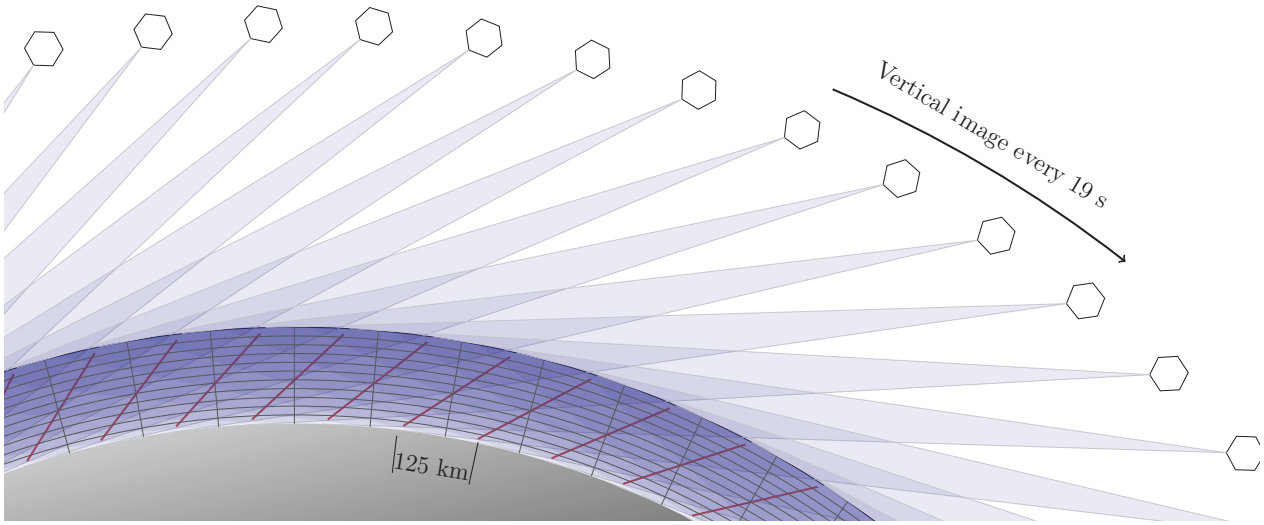

Figure 5.1: Conceptual image (not to scale) of the OMPS-LP viewing geometry and retrieval grid. The retrieval grid locations (gray lines) are chosen to match the average tangent point of the OMPS-LP measurements (red lines).

izontal retrieval grid locations (gray lines in Fig. 5.1) is chosen to match the average tangent point of each measurement image. As OMPS-LP measures scattered sunlight, each orbit has a natural start and stop point characterized by high solar zenith angles. In constructing the retrieval grid we use images with solar zenith angles at the tangent point of less than 88°.

A consequence of performing a tomographic retrieval is that there is less information at the edges of the retrieval grid, simply because there are fewer measurements which sample near the edges. As previously mentioned, our retrieval grid has hard cutoffs at solar zenith angle 88°. However, when constructing the measurement vector, we use all images with solar zenith angle less than 90°. Under this approach for typical conditions we have not noticed unphysical effects at the edges of the retrieval, but this is still under investigation. However there is still less information present at the retrieval boundaries, which is reflected in the resolution and precision estimates described in Sect. 5.5. The latitudinal coverage of OMPS-LP, and thus the retrieval grid, varies throughout the course of the year as the illuminated portion of the Earth changes. The latitude region 60° S–60° N is sampled nearly continuously throughout the year, while coverage extends to 82° in each hemisphere's summer.

Due to the Earth's rotation, there is a slight mismatch between the line-of-sight plane and the retrieval grid as is shown in Fig. 5.2. At the Equator the approximate mismatch is 5°, resulting in a $\sim$10 km horizontal distance between the next image's average tangent

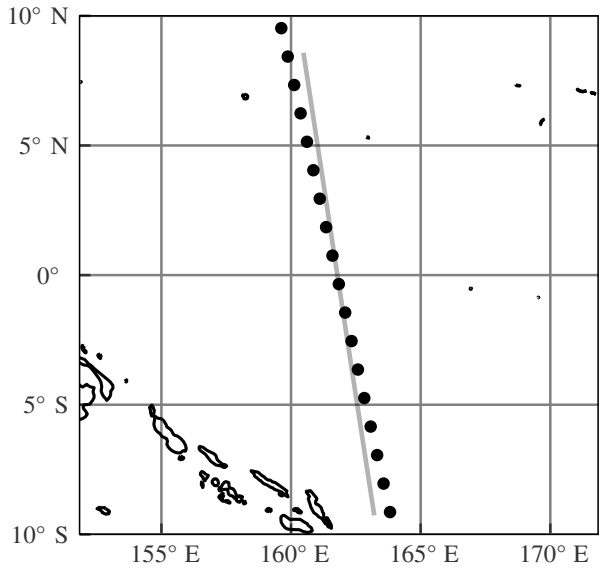

Figure 5.2: Example of mismatch between the line-of-sight plane and the tangent point ground track. Black dots show the tangent points (at 25 km) for OMPS-LP orbit 14940. The gray line represents the line-of-sight plane for the tangent point intersecting the line.

point and the previous image's line-of-sight plane. The effect is largest at the Equator, with the mismatch almost completely disappearing at the northern- and southernmost parts of the orbit (82° N and 82° S). To perform the retrieval, the horizontal component of the line-of-sight plane for every image is projected onto the horizontal component of the retrieval grid (orbital-track dimension).

5.3.3 The Forward Model

The forward model used in this study is SASKTRAN-HR (Bourassa et al., 2008; Zawada et al., 2015). SASKTRAN-HR solves the radiative transfer equation in integral form using the method of successive orders initialized with the incoming solar irradiance. The model is capable of handling inhomogeneities in the atmospheric state in the line-of-sight direction. Internally the forward model performs bi-linear interpolation between grid points to create a continuous representation of the atmosphere. In addition to radiance, the model also outputs the Jacobian matrix with respect to the underlying two-dimensional atmosphere. Jacobians are calculated analytically taking into account all first-order scatter terms, with

approximations made for higher-order terms. The forward model and the Jacobian calculation are described in depth in Zawada et al. (2015) and Zawada et al. (2017), respectively.

5.3.4 Computational Considerations

In a tomographic retrieval, the length of the state vector, n, and the length of the measurement vector, m, are significantly larger than those of a one-dimensional retrieval. For example, if the retrieval grid was set up to match the inherent resolution of the OMPS-LP measurements of a single orbit, for each species n would be on the order of 10 000, and for each wavelength m would also be on the order of 10 000. Storing these vectors does not pose any computational challenge; however, it quickly becomes necessary to store the $m \times n$ Jacobian matrix using sparse storage techniques. The Jacobian matrix is naturally sparse in the horizontal direction as sensitivity is largest at the tangent point and decreases away from it. Elements of the Jacobian matrix for the limb multiple-scattering problem are never truly zero; every point in the atmosphere should in theory contribute to every measurement. However, owing to the approximations made in the Jacobian calculation outlined in the section prior, contributions are only calculated along the line-of-sight and solar planes, resulting in a sparsity factor of ~ 0.05. The sparsity of the Jacobian matrix can be improved by artificially allowing only profiles less than some specified distance to the tangent point to contribute, as is done in Livesey et al. (2006). For our retrieval we limit each measurement to contribute to profiles within 10° of the tangent point.

While every matrix in Eq. (5.2) is sparse, it is often desirable from a computational-speed point of view to store some combinations of matrices densely. In particular, solving the linear system requires computing the $n \times n(\mathbf{K}_i^T \mathbf{S}_\epsilon^{-1} \mathbf{K}_i + \mathbf{R}^T \mathbf{R} + \gamma_i \mathbf{I})$ matrix. While it is still somewhat sparse, we have observed significant speed increases by solving the linear system densely. For a full OMPS-LP orbit this matrix would be $10\,000 \times 10\,000$, taking less than 1 GB of memory.

5.3.5 Accounting for the Time Dependence

Due to an inadequate amount of measurements, we do not account for the time variation of the ozone field in the retrieval. The reported time for each retrieved profile is calculated by interpolating the measurement times on the tangent points to the retrieval grid. While it is not perfect, we expect this is a good estimate as the majority of information for a single retrieved profile originates from the images that have tangent points near it. Nevertheless, there are several other time-dependent effects which play a role in how the retrieval is performed.

The radiative transfer equation is explicitly time dependent owing to the changing solar conditions. For an imaging instrument such as OMPS-LP, the natural and most accurate solution to this problem is to re-run the forward model for every image. That being said, there is potential for large computational-speed improvements by combining multiple images into the same forward-model calculation. Since SASKTRAN-HR solves the source function of the radiative transfer equation in a region of interest (nominally a 10° cone with the vertex at the Earth's center, but this can be configured) around the tangent point, there is considerable overlap between the field of interest of one image to the next. However, there are issues in performing this combination:

1. Each image happens at a different instant in time; thus the solar conditions have changed.

2. SASKTRAN-HR's internal atmosphere is specified as a plane in the line-of-sight direction. The lines of sight from one image do not necessarily lie in the same plane as the lines of sight for the next image. Furthermore, the more images that are combined together, the larger this plane will diverge from the retrieval grid.

3. The Earth is represented internally as a sphere with curvature matching a reference ellipsoid at the average tangent point, which changes from image to image.

The first and the third conditions are not unique to tomographic retrievals; limb-scanning instruments face similar challenges in one-dimensional retrievals. For example, a single OSIRIS limb scan sequence takes approximately 90 s and is modeled with a single forward-model calculation in operational retrieval algorithms (Degenstein et al., 2009). Internal tests

have been performed to quantify the three conditions by comparing results that modeled every image separately with retrievals that combined five subsequent images together (95 s variation from the first image to the last image), which resulted in mostly random differences in retrieved ozone on the order of 0.5 %.

5.3.6 Retrieval Ordering

The retrieval is performed for three major parameters: ozone number density, stratospheric aerosol number density, and surface reflectance assuming a Lambertian surface. While considerable effort has been put into both the aerosol and surface reflectance retrievals, they are performed primarily as a second-order correction for the ozone retrieval. Each species is retrieved independently, i.e., holding the other parameters fixed, but the overall retrieval operates in stages, feeding the results of previous parameter retrievals into the current one. The general retrieval order follows that of Degenstein et al. (2009) and is first surface reflectance, then aerosol number density, and then lastly ozone number density. Two passes of this overall procedure are performed, allowing results from the ozone retrieval to couple back into the other retrievals. The first pass of the procedure can be thought of as obtaining a good first guess for state vectors, while the second pass finalizes the retrieval.

A fixed number of iterations is performed in each of the passes. The first round of the retrieval procedure performs five iterations for each of the targeted quantities, while the second round performs two iterations. To verify that convergence has been reached, at every iteration both the current χ^2 value and the expected χ^2 value at the next step, assuming the problem is linear, are calculated. The expected χ^2 value at the next step, assuming the problem is linear, is calculated by performing a step with the Levenberg–Marquardt parameter set to 0, which helps to guard against situations where premature convergence is detected due to a large damping parameter. A similar technique is used in Livesey et al. (2006). At the end of the fixed number of iterations it was found that the final χ^2 value almost always matches the expected χ^2 value calculated at the previous iteration to within 1 %, indicating that the solution has likely converged. Orbits where convergence has not been seen at a 2 % level are flagged as suspicious. It is planned for a future version of the retrieval software to stop early if convergence is detected; however this is not expected to improve the

Table 5.1: Wavelength triplet/doublets used in the ozone retrieval.

Ozone-sensitive wavelength [nm]	Reference wavelength(s) [nm]	Valid altitudes [km]	Normalization altitude [km]
292.43	350.31	22–59	60
302.17	350.31	22–55	56
306.06	350.31	22–51	52
310.70	350.31	22–48	49
315.82	350.31	22–46	47
322.0	350.31	22–42	43
331.09	350.31	22–39	40
602.39	543.84, 678.85	0–30	31

solution, only the computational efficiency.

5.3.7 Ozone Measurement Vector

The ozone retrieval uses a common technique first suggested by Flittner et al. (2000) where ozone-sensitive wavelengths in the Hartley–Huggins and Chappuis bands are normalized by both ozone-insensitive wavelengths and high-altitude measurements. This technique, sometimes referred to as the triplet or doublet method, has been used successfully in a variety of limb scatter ozone retrievals (e.g., Degenstein et al., 2009; Loughman et al., 2005; Rault, 2005; Rault and Loughman, 2013b; von Savigny et al., 2003). The ozone cross section used in the retrieval is compiled from Daumont et al. (1992), Brion et al. (1993), and Malicet et al. (1995). While the triplet/doublet method has previously only been implemented for one-dimensional retrievals, many of the ideas are still applicable to two-dimensional retrievals with some modifications.

Our ozone measurement vector consist of seven doublets in the Hartley–Huggins absorption bands and one triplet in the Chappuis absorption band shown in Table 5.1. In one-dimensional retrievals the UV doublets are often forced to only contribute when the atmosphere is optically thin, i.e., when the area of maximal sensitivity is at the tangent point. This can be done either through analyzing the diagonal elements of the Jacobian matrix di-

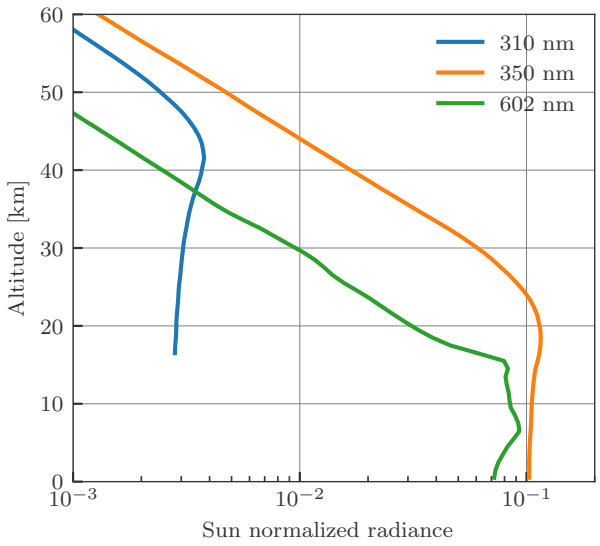

Figure 5.3: Sun-normalized radiances observed by OMPS-LP event number 90 of orbit 19490.

rectly (Loughman et al., 2005) or by only using altitudes above the "knee" of the atmosphere as is done in Degenstein et al. (2009). The primary reason to do this forcing is so that the retrieval is most sensitive to the tangent point, to minimize the effect of the implicit horizontal homogeneity assumption. Since the assumption of horizontal homogeneity is broken for the tomographic retrieval, we allow all UV doublets to contribute down to some minimum altitude, chosen to be 22 km. This altitude is approximately the knee of the 350 nm radiance profile; as seen in Fig. 5.3, radiances below this altitude are heavily sensitive to upwelling radiation and in particular absorbing aerosols.

The unnormalized measurement vector, $\vec{\tilde{y}}$, is given by

$$\vec{\tilde{y}}_{jkl} = \frac{1}{n_{\mathrm{ref}_l}} \sum_{\lambda \in \ \mathrm{ref}_l} \log[I_j(h_k, \lambda)] - \log[I_j(h_k,\ \mathrm{sens}_l)], \tag{5.3}$$

where j indexes image along an orbit, k indexes tangent altitude, l indexes the triplet, ref_l is the set of reference wavelengths for triplet l from Table 5.1 with corresponding length n_{ref_l}, and sens_l is the sensitive wavelength for triplet l from the same table. Each triplet/doublet is normalized by its value at a high altitude where the effect of ozone absorption on the observed radiance is minimal. The high-altitude normalization helps to minimize errors in the absolute calibration of the instrument and reduces the sensitivity to upwelling radiation. The normalization altitude varies for each doublet/triplet (shown in Table 5.1) and is pushed

low to minimize stray-light errors.

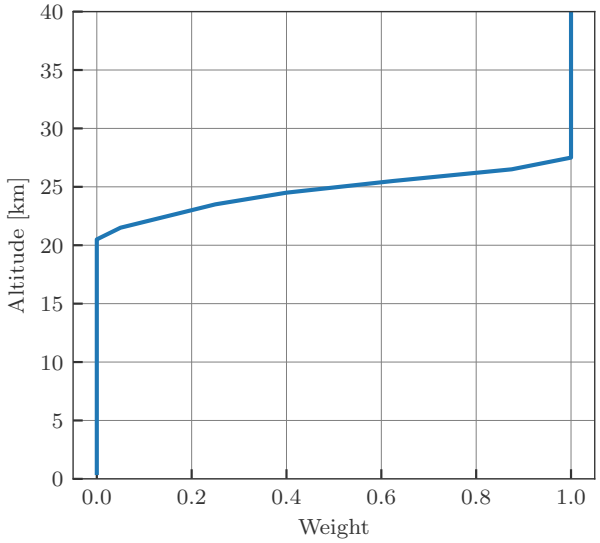

Figure 5.4: Scaling factors as a function of altitude applied to the UV doublet measurement error covariances.

To avoid discontinuities caused by suddenly introducing UV triplets near 22 km, the diagonal of the measurement error covariance matrix is artificially scaled during the retrieval:

$$\mathbf{S}_{\epsilon,ii} = \frac{\mathbf{S}_{\epsilon,ii}}{w^2}, \tag{5.4}$$

where the weights, w, are only applied to the UV triplets and only depend on altitude. The applied scale factors are shown in Fig. 5.4.

The initial guess for the ozone profile is taken from McPeters et al. (1997); we have observed negligible dependence on the choice of initial state (typically less than 1 % on the retrieved ozone values).

Figure 5.5 shows the retrieved ozone number density for OMPS-LP orbit 27695 (2 March 2017, 10:30 UTC at Equator crossing). Several low ozone filaments above the ozone layer are visible in both the Southern Hemisphere and Northern Hemisphere tropics and midlatitudes. In the Northern Hemisphere a low pocket of ozone can be seen below and intruding into the ozone layer.

Processing of this orbit took approximately 124 min using eight threads on an i7-4770k cpu. There were 159 vertical images of radiance data input to the retrieval, giving

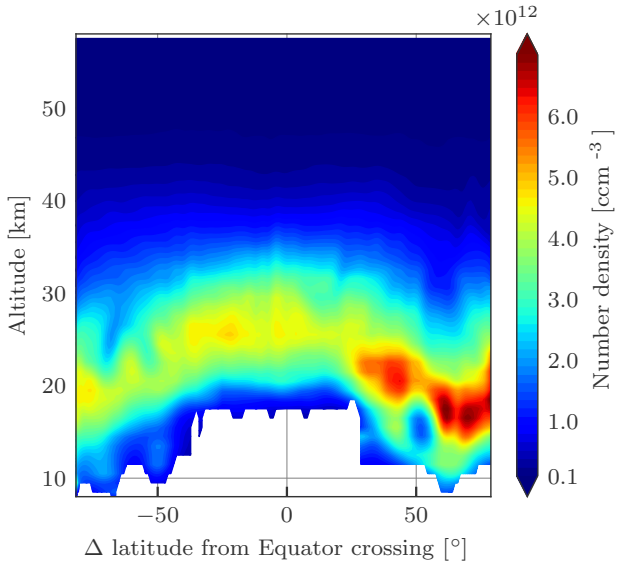

Figure 5.5: Retrieved ozone number density for OMPS-LP orbit 27695 (2 March 2017, 10:30 UTC at Equator crossing).

an approximate processing time of 47 s (vertical image)$^{-1}$. Thus performing the 2D retrieval is not onerous from a computational point of view; two machines of similar computational power are sufficient to keep up to date with routine processing.

5.3.8 Minor Retrieved Species

Stratospheric Aerosol

The stratospheric aerosol measurement vector definition follows closely the one outlined in Bourassa et al. (2012) and applied to OSIRIS measurements, with a few minor modifications. The unnormalized measurement vector is given by

$$\vec{y}_{jk} = \log[I_j(h_k, 745.67\,nm)]. \tag{5.5}$$

The altitude of normalization is chosen following the technique described by Bourassa et al. (2012).

The measurement vector described here differs from that of Bourassa et al. (2012) in that there is no normalization relative to a shorter wavelength (470 nm for the OSIRIS retrieval). The short-wavelength normalization was included to reduce the dependence of knowledge of the background Rayleigh atmosphere. However issues were encountered in that the short

wavelength would often be measured on a different gain setting than the longer wavelength, introducing artifacts in the retrieval (see Jaross et al., 2014, for more information on the gain settings of OMPS-LP). Since there exist many limb scatter aerosol retrieval algorithms that operate without a short-wavelength normalization (e.g., Rault and Spurr, 2010), for simplicity we have opted to remove it. Stratospheric aerosols in the retrieval are assumed to consist of liquid H_2SO_4 spherical droplets following a lognormal particle size distribution with a median radius of 80 nm and a mode width of 1.6. The phase function and cross sections are calculated using a standard Mie scattering code (Wiscombe, 1980), using the index of refraction from Palmer and Williams (1975).

Albedo

The forward model assumes a Lambertian reflecting surface parameterized by the albedo, the ratio of outgoing to incoming radiance. Typically this quantity does not physically represent actual reflectance from the surface of the Earth but is used as an approximation for all upwelling radiation from the troposphere. It is important to retrieve the albedo as many wavelengths used in the ozone retrieval are affected by upwelling radiation.

While albedo in the forward model is allowed to vary in the horizontal direction, several assumptions are made which make the albedo retrieval similar to a set of independent one-dimensional retrievals. Furthermore the albedo retrieval is not done under the Rodgers approach described earlier but instead follows the approach of Bourassa et al. (2007). We define the albedo state vector $\vec{x}_{\text{alb}}$ as the albedo on the surface of the Earth assuming a Lambertian surface at a set of latitudes and longitudes defined by the 40 km tangent point of each image. Therefore the state vector is the same length as the number of images used in the retrieval.

The albedo is iteratively updated with the equation

$$\vec{x}^{i+1}_{\text{alb},j} = \vec{x}^{i}_{\text{alb},j} \frac{I_{j,\text{meas}}(40\,km, 745.67\,nm)}{I_{j,\text{mod}}(40\,km, 745.67\,nm)}. \tag{5.6}$$

The measurement vector uses the same wavelength as the aerosol retrieval since their effects tend to be coupled together. The retrieval is one-dimensional in the sense that, at least for one specific iteration, each image is allowed to only affect one element of the albedo

state vector. However the forward-modeled radiance is calculated using the two-dimensional albedo field, which allows images to couple to other elements of the state vector over the course of multiple iterations.

The spectral dependence of the albedo is neglected in the present retrieval. Loughman et al. (2005) estimates that neglecting realistic surface types (such as desert or savannah type surfaces) can cause systematic biases of up to 4 % at 10 km for typical ozone retrievals. However these results are likely worst-case estimates, as realistic tropospheric upwelling radiation is expected to be more spectrally diffuse than a clear surface.

5.3.9 Regularization

The retrieval uses an ad hoc Tikhonov style (Tikhonov, 1943) second derivative constraint applied only in the horizontal direction of the retrieval grid. The regularization matrix takes the form

$$\mathbf{R} = \alpha \begin{pmatrix} -\frac{1}{4} & \vec{0} & \frac{1}{2} & \vec{0} & -\frac{1}{4} & 0 & 0 & \dots \\ 0 & -\frac{1}{4} & \vec{0} & \frac{1}{2} & \vec{0} & -\frac{1}{4} & 0 & \dots \\ 0 & 0 & -\frac{1}{4} & \vec{0} & \frac{1}{2} & \vec{0} & -\frac{1}{4} & \dots \\ \vdots & \vdots & \vdots & \vdots & \vdots & \vdots & \vdots & \ddots \end{pmatrix}, \tag{5.7}$$

where α is a constant scaling factor used to control the amount of regularization and $\vec{0}$ indicates a number of zeros equal to the number of altitude grid points minus 1. The value of α is chosen to control the horizontal resolution of the retrieved species; for example, the value for ozone is 40, resulting in a 300–400 km horizontal resolution (see Sect. 5.5). The a priori state vector of Eq. (5.2) is chosen to be 0. As the regularization matrix used only applies in the horizontal direction, the horizontally integrated vertical resolution of the retrieved profiles matches the vertical resolution of the retrieval grid.

It should be noted that, even though we apply no constraints in the vertical direction, the retrieval software is capable of doing so. While the above discussion treats the horizontal and vertical dimensions of the grid as separate entities, the retrieval vertical and horizontal resolutions are inherently coupled together. A lower-resolution horizontal grid allows for a higher-resolution vertical grid, keeping the total information content relatively constant,

and vice-versa. We make no claims on what is the optimal relationship between these two resolutions, and it is something that we are actively investigating. It is important to mention that a one-dimensional retrieval makes the trade-off decision for you, allowing control of only the vertical constraint. The effects of a one-dimensional retrieval on horizontal resolution have been studied for the Michelson Interferometer for Passive Atmospheric Sounding by von Clarmann et al. (2008).

5.4 Pointing Correction

Accurate and stable pointing knowledge is of particular importance for limb scatter measurements as it is typically not possible to simultaneously measure pressure. Moy et al. (2017) provide a detailed characterization of the OMPS-LP pointing errors; however many of these corrections have only been applied to the v2.5 L1G product, and not the v2.0–2.4 L1G product used in this study. Therefore for the current version of the retrieval a separate pointing analysis has been performed.

We apply the Rayleigh Scattering Attitude Sensor (RSAS) (Janz et al., 1996) to the OMPS-LP measurements. The ratio of the measured radiance at 40 and 20 km near 350 nm is compared to the calculated radiance. At 40 km the radiance is sensitive to tangent altitude changes, while at 20 km the radiance is not very sensitive since the line-of-sight path has become optically thick. Based on the difference between the measured and modeled ratios, it is possible to calculate an effective tangent altitude offset. The RSAS technique is sensitive to both upwelling radiation and stratospheric aerosol loading, which makes it difficult to apply at low solar zenith angles and in forward-scatter conditions, respectively.

To minimize the effects of both upwelling radiation and stratospheric aerosols, we only use measurements with solar zenith angle between 70 and 50° with solar scattering angles greater than 90°. Measurements satisfying similar criteria have recently been successfully used to apply an RSAS pointing correction to OSIRIS retrievals by Bourassa et al. (2018). While measurements with a solar zenith angle greater than 70° would have even less upwelling radiation, it is more challenging to accurately model the multiple scatter component of the radiance. Cutoffs greater than 50° were not found to affect the results; 50° was chosen to

maximize the number of measurements. The altitude offsets were daily averaged and are shown in Fig. 5.6. Offsets range from approximately 400 to 0 m with a clear seasonal cycle; in April 2013 there is noticeable $\sim$100 m drop due to a known star tracker adjustment. Being able to clearly observe the star tracker adjustment provides confidence that at least on a relative scale we are able to detect pointing shifts with the RSAS method.

It is currently unknown whether or not the seasonal structure represents a true pointing shift or if it is an artifact of the RSAS method – perhaps due to the average latitude of the measurements also varying seasonally and changing cloud cover. We do not detect any significant pointing drift greater than $\pm$100 m; however later years are affected by stratospheric aerosols from Kelud and Calbuco, which may skew the RSAS technique. Preliminary validation efforts have revealed that, on average, there is likely an absolute pointing error present in the OMPS-LP measurements. To calculate the applied pointing correction (solid line in Fig. 5.6), we take an average value both before and after the star tracker adjustment. All ozone profiles are shifted downwards by this amount after the retrieval has been performed. It should be noted that this applied pointing correction is by intention simple. A future version of the data product will examine the pointing in more depth and apply the correction to the instrument lines of sight rather than post-shifting the retrieved profile.

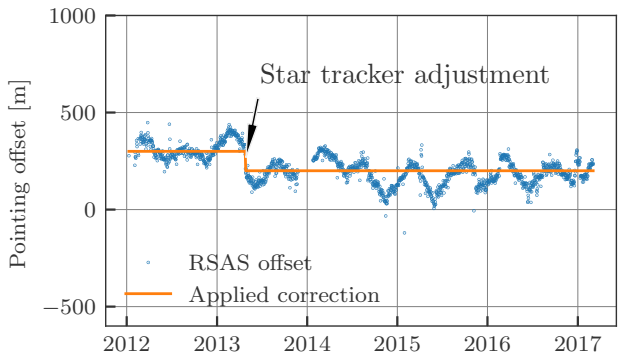

Figure 5.6: Daily averaged pointing offsets calculated with the RSAS technique. The orange line shows the applied pointing correction for v1.0.2 of the retrieved data product.

5.5 Error Analysis and Resolution

Both the random and systematic error components of a limb scatter ozone retrieval algorithm for a similar, but one-dimensional, retrieval have been studied in Loughman et al. (2005). Applying the conclusions of Loughman et al. (2005) to our retrieval algorithm suggests that the dominant sources of random error are pointing knowledge and the error due to measurement noise. Rault and Loughman (2013b) have also presented similar findings for a one-dimensional retrieval algorithm applied to OMPS-LP and in particular showed that the error due to measurement noise is representative of the total random-error budget. We will not repeat these analyses here; rather we will simply present the technique used to calculate the reported error estimate for each orbit.

Under the Rodgers framework the gain matrix, $\hat{\mathbf{G}}$, is given by

$$\hat{\mathbf{G}} = (\hat{\mathbf{K}}^T \mathbf{S}_\epsilon^{-1} \hat{\mathbf{K}} + \mathbf{R}^T \mathbf{R})^{-1} \hat{\mathbf{K}}^T \mathbf{S}_\epsilon^{-1}, \tag{5.8}$$

and the averaging kernel by

$$\mathbf{A} = \hat{\mathbf{G}} \hat{\mathbf{K}}, \tag{5.9}$$

where the hats indicate that the solution has converged. The solution covariance due to measurement noise only can also be estimated as

$$\hat{\mathbf{S}}_{\text{noise}} = \hat{\mathbf{G}} \mathbf{S}_\epsilon \hat{\mathbf{G}}^T. \tag{5.10}$$

In the current version of the retrieval only the solution covariance due to measurement noise is reported. For the purposes of the precision estimate we assume that the measurement covariance is diagonal, with the radiance measurements having a signal-to-noise ratio of 100, an upper bound on the error estimate taken from Jaross et al. (2014). Only the diagonal elements of the solution covariance are used for the error estimate. Since the state vector is the logarithm of number density, the precision estimate in logarithmic space is propagated to linear space for the reported precision estimate.

Figure 5.7 shows an example precision estimate for OMPS-LP orbit 27695 (2 March 2017, 10:30 UTC at Equator crossing). Precision estimates are in the range 2–5 % for the

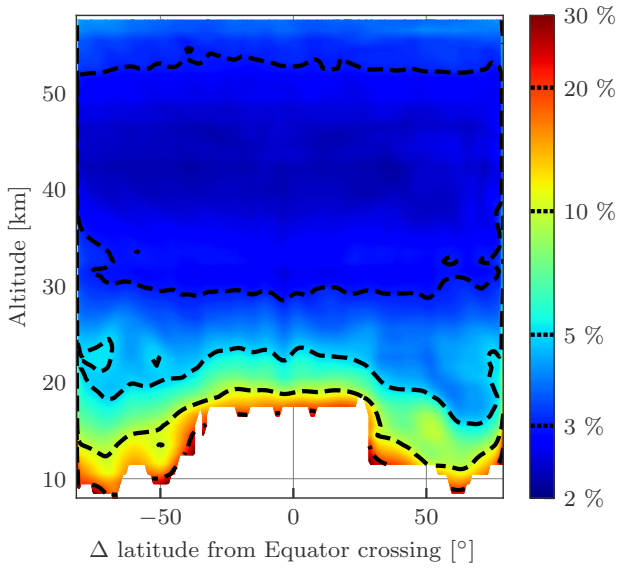

Figure 5.7: Precision estimate for ozone in percent for OMPS-LP orbit 27695 (2 March 2017, 10:30 UTC at Equator crossing). Contour levels are indicated by dashed lines on the color bar. The corresponding retrieved ozone profiles are shown in Fig. 5.5.

majority of the middle and upper stratosphere. In the lower stratosphere precision is $\sim 10\,\%$, increasing to $30\,\%$ near the tropopause. Various edge effects of the retrieval are also visible, most noticeably the increase in error at the beginning and end of the orbit and near where the lower bound of the retrieval changes (due to the lowering tropopause) at midlatitudes. These are expected effects; edges of the retrieval grid inherently have fewer measurements contributing to them, increasing the expected noise. The estimate precision varies only slightly between orbits, and the values stated above are generally valid for the entire dataset.

The resolution of the retrieval is found by analyzing the retrieval averaging kernels. As the retrieval is two-dimensional, each row of the averaging kernel contains both vertical and horizontal components. Since the regularization term (Eq. 5.7) contains no vertical information, it can be shown that the horizontally summed averaging kernel (i.e., the vertical averaging kernel) is the identity matrix. This has also been verified by calculating the vertical averaging kernel for a set of OMPS-LP orbits, which were all found to be identically unity.

While Eq. (5.8) is valid for well-posed, converged retrievals, recent work by Ceccherini and Ridolfi (2010) has suggested a modification for cases when a Levenberg–Marquardt term is used to damp the iterative step. Their formulation involves a recursive definition for the gain matrix, taking into account each iterative step, and converges to Eq. (5.8) in cases

where the state vector has reached adequate convergence. It is not straightforward to apply this technique to a full OMPS-LP orbit due to the memory requirements of storing multiple gain matrices. However, as a sanity check we have applied the technique of Ceccherini and Ridolfi (2010) to a 60-image subset of OMPS-LP orbit 20657 (23 October 2015, 08:50 UTC at Equator crossing).

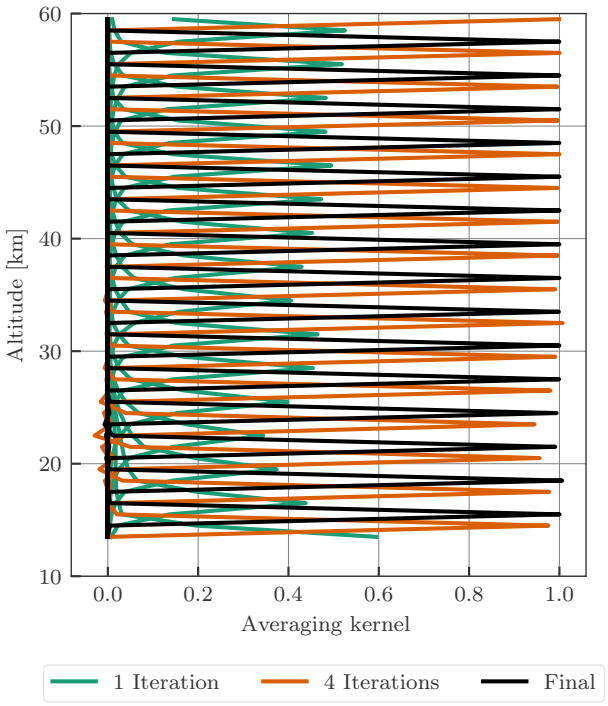

Figure 5.8: Vertical averaging kernels at 40° S for OMPS-LP orbit 20657 (23 October 2015, 08:50 UTC at Equator crossing) calculated using the methodology of Ceccherini and Ridolfi (2010) after one, four, and seven iterations of the retrieval procedure. For clarity only every third row of the vertical averaging kernel is shown for each case.

Vertical averaging kernels from this test are shown in Fig. 5.8. As expected, due to the inclusion of the Levenberg–Marquardt damping term, after one iteration rows of the averaging kernel are far from unity, with peak values on the order of ~ 0.4. After four iterations the rows are close to unity with peak values of ~ 0.95. At the end of the retrieval the averaging kernel rows are nearly identical to unity with peak values of ~ 0.99 in the worst case. Therefore, we can say that the retrieval is sufficiently converged for Eq. (5.8) to be valid. Considering the vertical averaging kernel contain little information, we will focus on the vertically integrated, or horizontal, averaging kernel.

Figure 5.9 shows the rows of the horizontal averaging kernel for two orbits in different

seasons at 0 and 55° N. In both cases the horizontal full width at half maximum (FWHM) is smallest near 40 km with values of ∼250 km. For the majority of the altitude range the FWHM is less than 400 km, with the exception of the region near the tropopause where it can increase to 500 km. Only minor differences in the FWHM are seen between the tropical and midlatitude averaging kernel rows, with the majority of the differences occurring near the lower bound of the retrieval. Averaging kernels are not stored for every orbit due to size constraints; however it was found that deviations from orbit to orbit are small enough that the above resolution estimates are representative for the entire dataset.

As previously stated, the vertical averaging kernels are identity, suggesting that the vertical resolution of the retrieval is 1 km, the same as the retrieval grid. However, the instrumental vertical field of view (∼1.5 km; see Jaross et al., 2014) is neglected in the retrieval process, treating each measurement with a single line of sight. Therefore we estimate the vertical resolution of the retrieved profiles to be 1–2 km. Including the vertical field of view in the retrieval process to obtain a better estimate of the vertical resolution is currently under investigation. It is not currently possible to fully account for the vertical field of view as the OMPS-LP L1G product is a gridded data product that does not provide an estimate of the vertical field of view. Preliminary simulation studies including an instrumental vertical field of view of 1.5 km have indicated that neglecting the vertical field of view leads to biases less than 2 %, with the majority of differences seen in the 20–25 km region.

5.6 Preliminary Results

5.6.1 Simulations on the Edge of the Polar Vortex

To test the retrieval method, a one-dimensional retrieval method that assumes horizontal homogeneity has also been developed to compare against. The one-dimensional retrieval has been designed to be as similar to the two-dimensional retrieval as possible. The measurement vectors for ozone, albedo, and stratospheric aerosol are the same as those for the two-dimensional retrieval, with the only difference being that the number of images used is one instead of an entire orbit. The state vector is modified to be one-dimensional in alti-

tude, representing a horizontal homegenous atmosphere with 1 km vertical spacing. As the Tikhonov regularization is only applied in the horizontal direction for the two-dimensional retrieval, no regularization is used in the one-dimensional retrieval. The same iterative procedure is also used for the one-dimensional retrieval.

To test the ability of the two-dimensional retrieval to resolve horizontal gradients in the ozone field, simulated retrievals have been performed. For the simulations, measurements from a full OMPS-LP orbit are simulated using a two-dimensional ozone field. The resulting radiances are then used in both the one- and two-dimensional retrievals. To isolate the effects of horizonal ozone gradients, the input aerosol and albedo fields are assumed to be known and horizontally homogenous.

Figure 5.10 shows the results of the simulated retrieval for OMPS-LP orbit 20567. Qualitatively there is good agreement between the one- and two-dimensional retrievals and the true ozone field, providing confidence in both methods. The two-dimensional retrieval agrees to better than 5 % with the true ozone profile almost everywhere, with a few exceptions below 20 km. Looking at the 15.5 km slice of the retrieval (top right panel of Fig. 5.10), it can be seen near 50° S that the two-dimensional retrieval smooths out some of the fine oscillatory structure of the true profile, which is expected from the form of the averaging kernel. That being said, the two-dimensional retrieval captures the large ozone gradient in the 60°–75° S region very well.

Overestimation by the one-dimensional retrieval can be seen in the 60°–75° S, 10–20 km region. The 15.5 km slice reveals that the one-dimensional retrieval assigns the horizontal gradient to the wrong location, leading the true profile by $\sim 2°$. Consistent overestimation by the one-dimensional retrieval is what would be expected by the measurement geometry and input ozone field. As OMPS-LP looks backward in the orbital plane, measurements near the edge of the polar vortex consistently look through high ozone values into lower ozone values. For limb scatter measurements ozone sensitivity is larger on the instrument side of the line of sight (for an indepth discussion of this effect see Zawada et al., 2017); the high ozone values near OMPS-LP are incorrectly assigned to tangent points inside or near the vortex.

To assess the impact of viewing geometry on the retrieval, a second simulation has been performed with a large horizontal ozone gradient present in the Northern Hemisphere. For

this simulation the geometry from OMPS-LP orbit 12300 (14 March 2014) was used. The simulated ozone field was taken from 14 March 2011 to obtain a realistic scenario with large polar ozone depletion. The results of the simulation are shown in Fig. 5.11.

The one-dimensional retrieval consistently underestimates the true ozone profile in the 60–70° N region. In this gradient region the instrument's line of sight is looking through low ozone values into high ozone values, opposite of the prior simulation; thus underestimation is expected. As before, the one-dimensional retrieval leads the true profile, which can be seen in the 17.5 km slice (top right panel of Fig. 5.11). The magnitude of the underestimation (10–20 %) is less than the overestimation of the prior simulation (50 %), primarily because the gradient is weaker and does not extend into the lower altitudes. The two-dimensional retrieval captures the structure of the gradient quite well; as before, some horizontal smoothing errors on the order of 5–10 % can be seen at altitudes below 20 km.

5.6.2 Monthly Zonal Mean Anomalies

As a zeroth-order validation effort, monthly zonal mean relative ozone anomalies have been performed against the MLS v4.2 ozone measurements. The MLS retrievals' (Livesey et al., 2006) native product is volume mixing ratio on pressure surfaces; for these comparisons we have converted MLS v4.2 measurements to number density on altitude levels using ERA-Interim reanalysis (Dee et al., 2011). The MLS data have been screened according to the recommendations of Livesey et al. (2017). Figure 5.12 shows the result of these comparisons in the tropical 5° S–5° N latitude bin. Qualitatively there is excellent agreement; the anomalous change in the Quasi-Biennial Oscillation beginning at the end of 2015 can clearly be seen in both datasets. Quantitatively, above 25 km observed differences in relative anomaly are less than 0.05 ($\sim$ 5 % change in ozone) for all time periods. Below 25 km differences on the order of 0.1 are seen, which could be related to larger variability in the tropical upper thermosphere and lower stratosphere. Anomalies from the dataset in other latitude bands have been studied in detail by Sofieva et al. (2017).

As a second check, the raw monthly zonal mean values are compared to those from MLS for the same latitude band in Fig. 5.13. In the 25–45 km range, differences are generally less than 5 %. Below 25 km differences on the order of 10 % can be seen in the 2014–2015 and

early 2016 time periods. It is thought that these differences could be retrieval artifacts caused by the large stratospheric aerosol loading following the Kelud and Calbuco eruptions in 2014 and 2015, respectively. Large high biases can be seen at the lowest altitudes (16–18 km), which could be explained by the retrieval lower bound being set to the tropopause, causing a sampling bias. Values used to calculate the monthly zonal mean for MLS could consist of both tropospheric and stratospheric air, while monthly zonal means from OMPS-LP are purely stratospheric, leading to higher observed values. Above 45 km OMPS-LP is low relative to MLS; however these results are not representative as both day and nighttime measurements are used to calculate the MLS monthly zonal means, which causes differences when the diurnal variation of ozone is significant.

5.6.3 Nearly Perfect Coincidences with MLS

MLS on board Aura and OMPS-LP on board Suomi-NPP are both in sun-synchronous orbit with similar inclination and local crossing times; however Suomi-NPP orbits near ~ 800 km, while Aura is at ~ 700 km. The slight difference in orbital periods causes the measurement ground tracks to drift relative to each other, with near-perfect overlap, in both space and time, every 2–3 days. Figure 5.14 shows the measurement track of OMPS-LP orbit 11915 (14 February 2014, 04:35 UTC at Equator crossing); also shown are the available measurements from MLS which are nearly perfectly coincident to the OMPS-LP measurements. At the crossing point there is a time difference of 16 min, and the differences in longitude are less than 1° for the entire orbit track. It should be mentioned that sampling differences in latitude do not play a large factor as both the MLS and OMPS-LP retrievals are two-dimensional, with the horizontal along-track resolution being poorer than the sampling frequency. For example, at 20 km, the OMPS-LP retrieval has a horizontal sampling of ~ 125 km with an estimated horizontal resolution of 350 km, while MLS v4.2 samples every ~ 150 km with a horizontal resolution of 300 km (Livesey et al., 2017).

The MLS retrieval is also two-dimensional and has similar along-track resolution to the two-dimensional OMPS-LP retrieval; thus we have not applied horizontal averaging kernels for these tests. To account for differences in vertical resolution, the procedure recommended by Livesey et al. (2017) has been used. The OMPS-LP data are degraded to the MLS pres-

sure grid with a least squares fit and then converted back to the altitude grid in a consistent fashion; however internal tests have shown that this makes negligible differences. A full validation of the dataset is intended for a forthcoming publication; however an initial validation check has been performed by examining near-coincident orbits between Aura (MLS) and Suomi-NPP (OMPS-LP).

Figure 5.15 shows the retrieved ozone for OMPS-LP orbit 11915 (14 February 2014, 04:35 UTC at Equator crossing) and coincident MLS measurements. Qualitatively there is excellent agreement between the two retrievals. A triple ozone peak at low altitudes is seen in both retrievals in the Northern Hemisphere, and both retrievals resolve a break in the ozone peak near 40° S. Some slight horizontal oscillations are observed ($\sim \pm 5\,\%$) in the USask OMPS-LP retrieval near the Equator. The exact cause of the oscillations is currently unknown, but initial investigation suggests that it could be caused by the combination of cloud cover affecting the large amount of upwelling radiation observed due to low solar zenith angles ($\sim 20°$) seen in the tropics.

Quantitatively agreement between the two retrievals (bottom panel of Fig. 5.15) is better than 5 % for the majority of the stratosphere. Differences greater than 10 % are seen at the lowest altitudes of the retrieval grid; it is possible that these are caused by the nonlinearity involved in applying the pointing correction to the retrieved profile rather than the measurement tangent altitudes themselves. At the northern edge of the retrieval grid there are also differences on the order of 5–10 %, which could be indicative of an edge effect in the two-dimensional retrieval. Above 45 km there is a large amount of variance observed; however this is reflected in the MLS precision estimate ($\sim 20\,\%$ at 0.5 hPa).

Next, 251 coincident orbits were identified that are uniformly distributed from the 2012–2013 time period, where the time difference at Equator crossing was less than 20 min and the average longitude difference for the full orbit was less than 1°. Figure 5.16 shows the results of these comparisons in various latitude bins. Generally agreement is within 5 %, with the exception of altitudes below 18 km in the tropics, where OMPS-LP is biased low at the 10–20 % level. Low biases are also observed near 50 km in most latitude bins; however the effect is most noticeable at 60°–90° S, where differences reach 8 %. Also shown in Fig. 5.16 is the observed standard deviation (SD) and the predicted SD using the supplied precision

values for both data products. While the observed SD does also include natural variability since the two measurements are not perfectly temporally/spatially co-located, we do not expect this to be a noticeable effect due to the tight coincidence criteria. The generally good agreement seen between the observed and predicted SD provides confidence in the supplied precision values for the dataset.

Lastly, results are shown for OMPS-LP orbit 20657 (23 October 2015, 08:50 UTC at Equator crossing), which are also nearly perfectly coincident to measurements from MLS. For this orbit we also apply the one-dimensional retrieval described in Sect. 5.6.1, and the retrieval results are shown in Fig. 5.17. Similar to the previous orbit, agreement in the middle stratosphere is typically better than 5 % between MLS and the two-dimensional retrieval. The one-dimensional retrieval also agrees favorably with MLS in the middle stratosphere. Inside the vortex there is larger disagreement; however this is expected due to the low absolute ozone values and the inherent variance of the retrievals.

Highlighted in Fig. 5.17 (dashed lines) is the 60°–75° S, 10–20 km region, which is the region where the one-dimensional retrieval performed poorly in the simulations of Sect. 5.6.1. In this region the two-dimensional retrieval agrees better with MLS than the one-dimensional retrieval, with the one-dimensional retrieval consistently overestimating the ozone values. The 15.5 km slice (top right panel of Fig. 5.17) shows the one-dimensional retrieval leading both MLS and the two-dimensional retrieval, which is consistent with the prior simulation results. If we interpret the difference between the profiles at 15.5 km entirely as a latitudinal offset, then the difference between the two-dimensional retrieval and MLS is $\sim 0.5°$, while the difference between the one-dimensional retrieval and MLS is $\sim 2°$ at 65° S.

5.7 Conclusions

A two-dimensional retrieval algorithm which directly accounts for atmospheric variations in the along-orbital-track dimension has been developed for use with limb scatter measurements from OMPS-LP. The retrieval algorithm combines all measurements from the sunlit portion of the orbit and simultaneously fits the full ozone profile for the portion of the orbit with solar zenith angle less than 88°. The vertical resolution of the retrieved profiles is estimated to be

1–2 km, while the along-track resolution is controlled with a Tikhonov type second squared difference constraint and is typically 300–400 km for retrievals from OMPS-LP. The estimated precision of the retrieved ozone product is 2–5 % for the middle and upper stratosphere, with values increasing to 30 % just above the tropopause. Simulated retrievals were shown indicating that the retrieval is working as expected and offers improvement over traditional one-dimensional retrievals in areas of large horizontal gradients.

The retrieval algorithm has been applied to all measurements from the center slit of OMPS-LP from early 2012 to present to create a multi-year near-global ozone time series. Tropical ozone anomalies from the dataset agree well with those from MLS v4.2, with differences greater than 5 % of the ozone mean value only observed below 25 km.

A preliminary validation effort is presented comparing coincident measurements from MLS. These measurements are nearly perfectly coincident with time differences of less than 20 min and longitude differences of less than 1°. For the majority of the stratosphere differences are less than 5 %; larger differences are seen at the edges of the retrieval grid. Qualitatively the precision estimate matches the observed scatter seen in the differences. Coincident comparisons during the 2015 ozone hole indicate that the two-dimensional retrieval and MLS agree qualitatively well at the edge of the polar vortex, whereas a traditional one-dimensional retrieval is shown to systematically overestimate in this area.

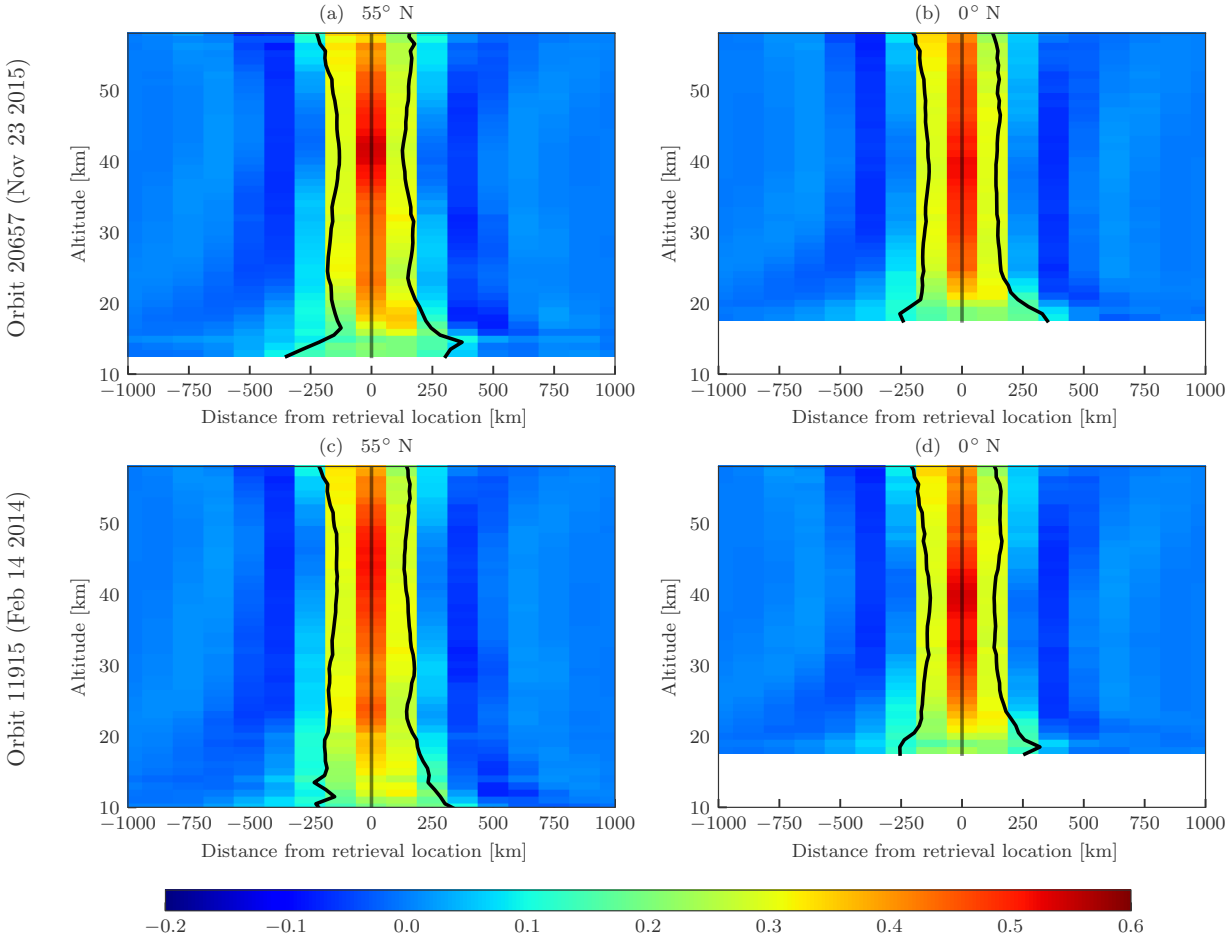

Figure 5.9: Horizontal averaging kernels from OMPS-LP orbit 20657 (23 October 2015, 08:50 UTC at Equator crossing) and OMPS-LP orbit 11915 (14 February 2014, 04:35 UTC at Equator crossing) for 55° N **(a, c)** and 0° N **(b, d)**. Data are masked below the lowest retrieval altitude. Vertical black lines show the FWHM boundaries, while the vertical gray line indicates the location of the retrieval. Distance from the retrieval location is defined as negative towards the start of the orbit in the Southern Hemisphere and positive towards the end of the orbit in the Northern Hemisphere.

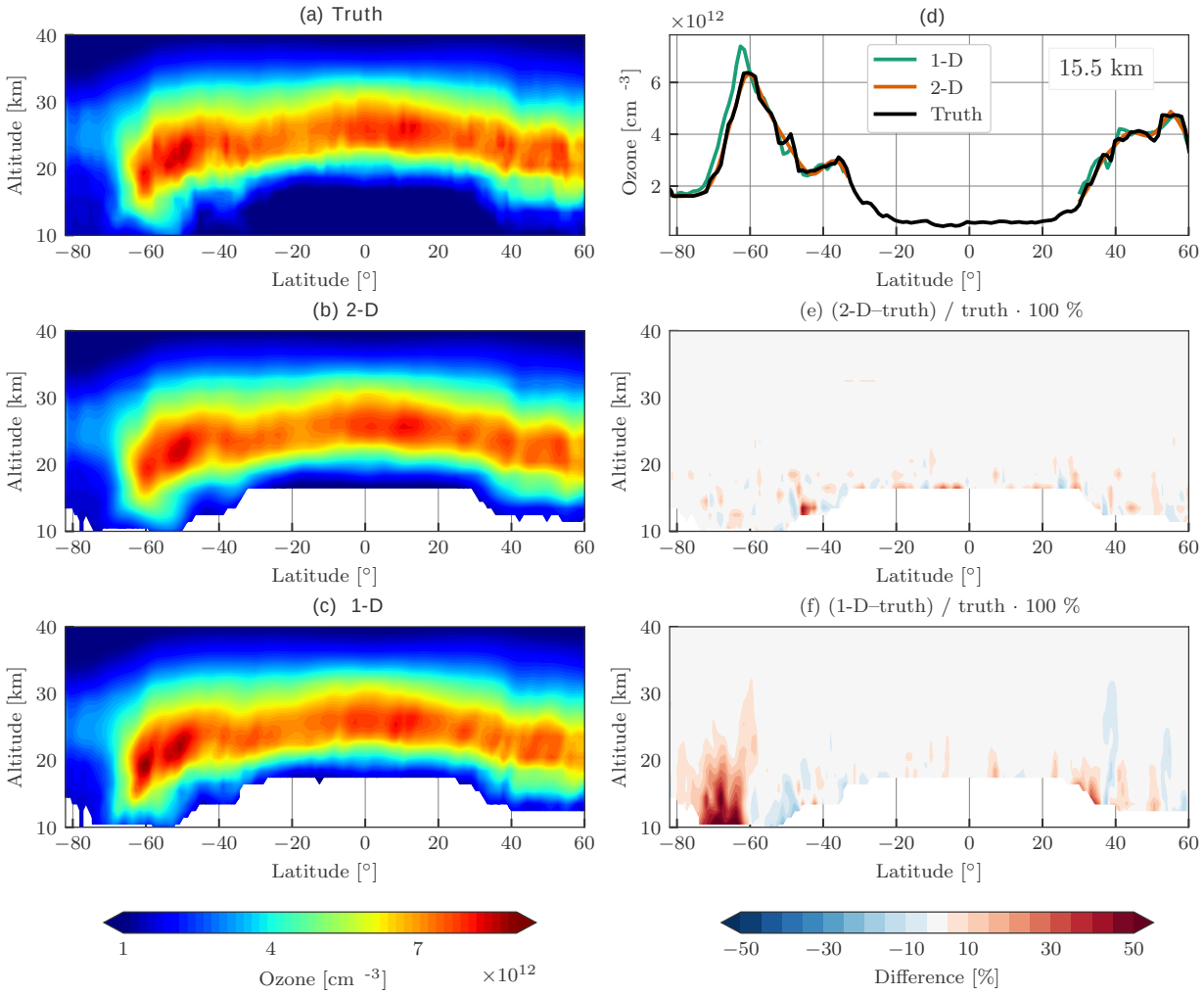

Figure 5.10: Simulated retrieval results for OMPS-LP orbit 20657 (23 October 2015, 08:50 UTC at Equator crossing). The left column shows the true ozone field **(a)**, tomographically retrieved ozone **(b)**, and one-dimensionally retrieved ozone **(c)**. The right column contains a horizontal slice of the retrieved ozone at 15.5 km **(d)**, the percent difference between the tomographic retrieval and the truth **(e)**, and the percent difference between the one-dimensionally retrieved ozone and the truth **(f)**. For the percent-difference panels contours are shown every ±5 %.

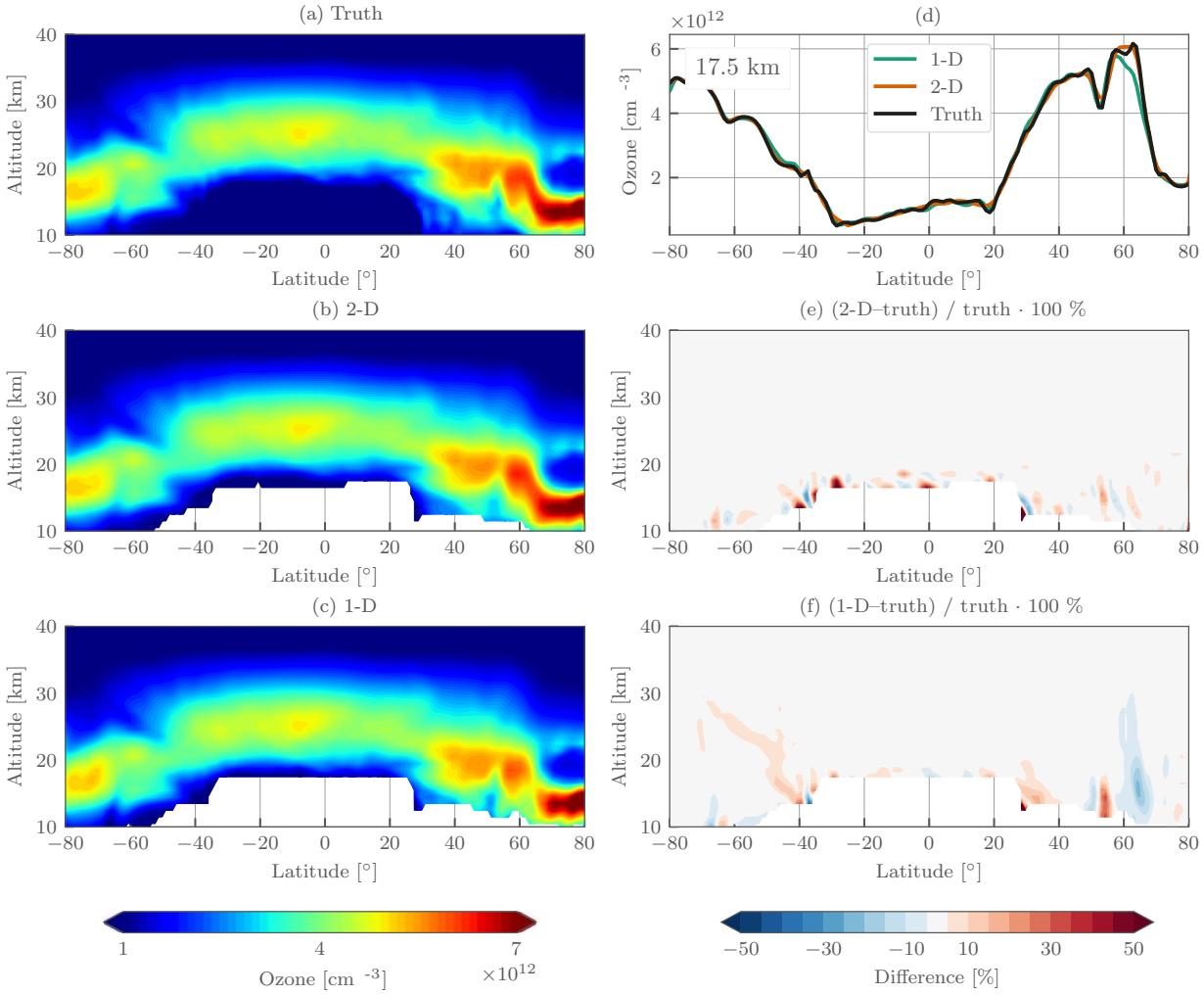

Figure 5.11: Same as Fig. 5.10 but for OMPS-LP orbit 12300.

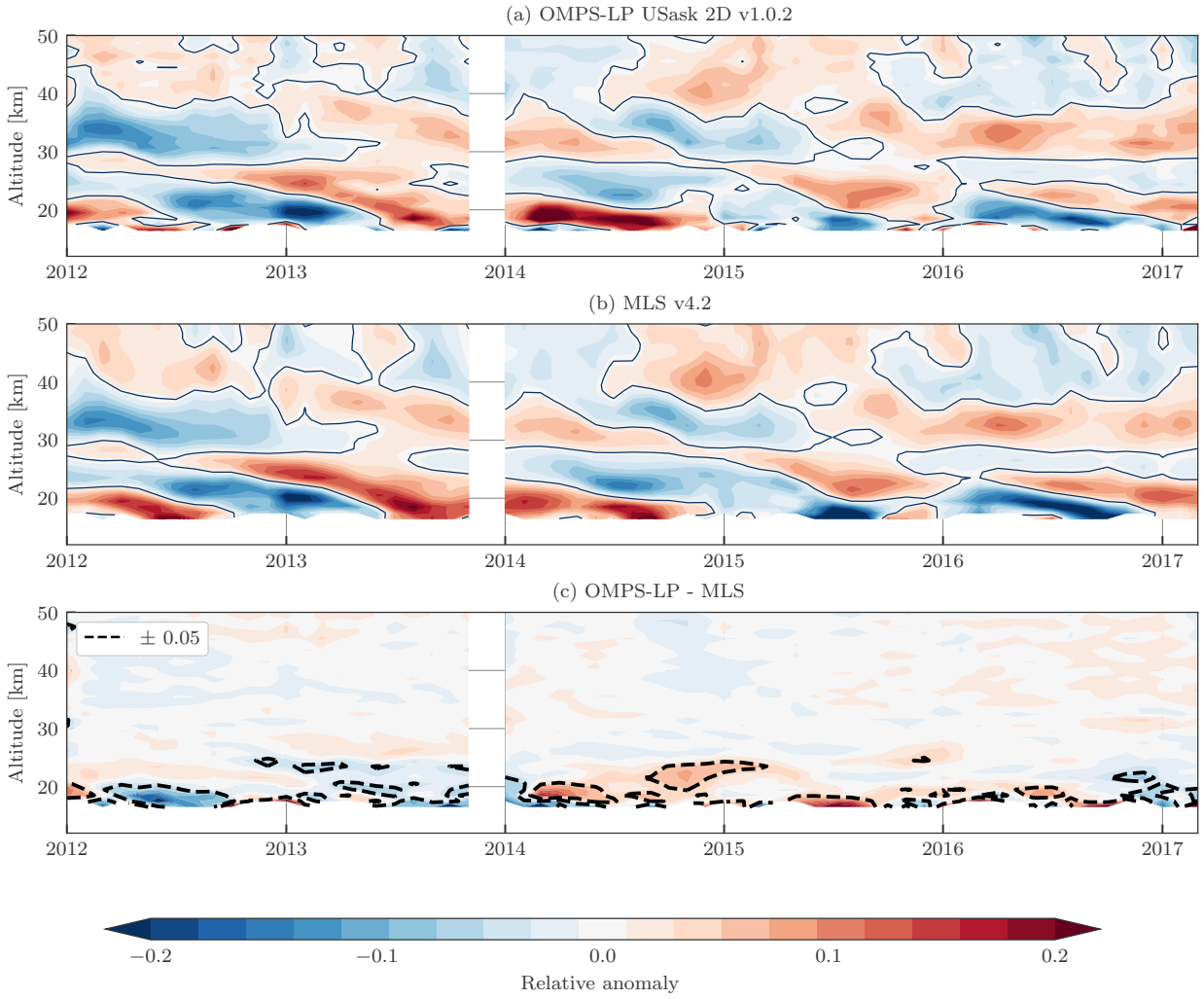

Figure 5.12: Monthly zonal mean ozone anomalies in the 5° S–5° N bin for OMPS-LP **(a)**, MLS v4.2 **(b)**, and their absolute difference **(c)**. Anomalies are calculated relative to the common overlap period, and data are masked outside the common overlap period.

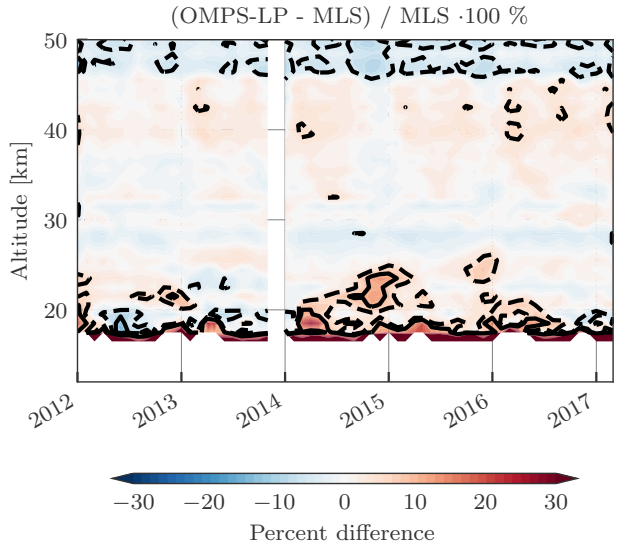

Figure 5.13: Percent difference comparing monthly zonal mean values from OMPS-LP and MLS v4.2. Dashed black contour lines are the ±5 % levels, while solid black contour lines are the ±10 % levels.

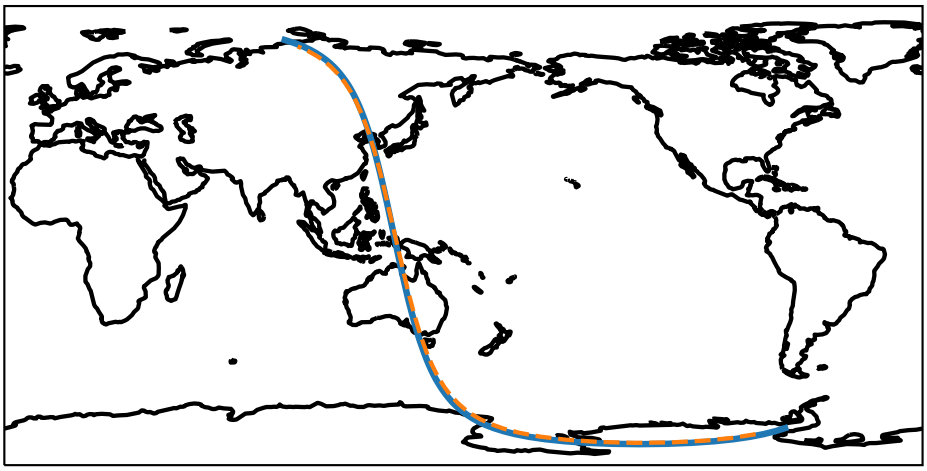

Figure 5.14: An example of nearly perfectly coincident measurements from OMPS-LP and MLS. The dashed orange line shows the retrieval grid points for OMPS-LP orbit 11915 (14 February 2014, 04:35 UTC at Equator crossing), while the blue line shows the retrieval locations for the near-coincident MLS measurements. The time difference at the crossing point is ∼ 16 min.

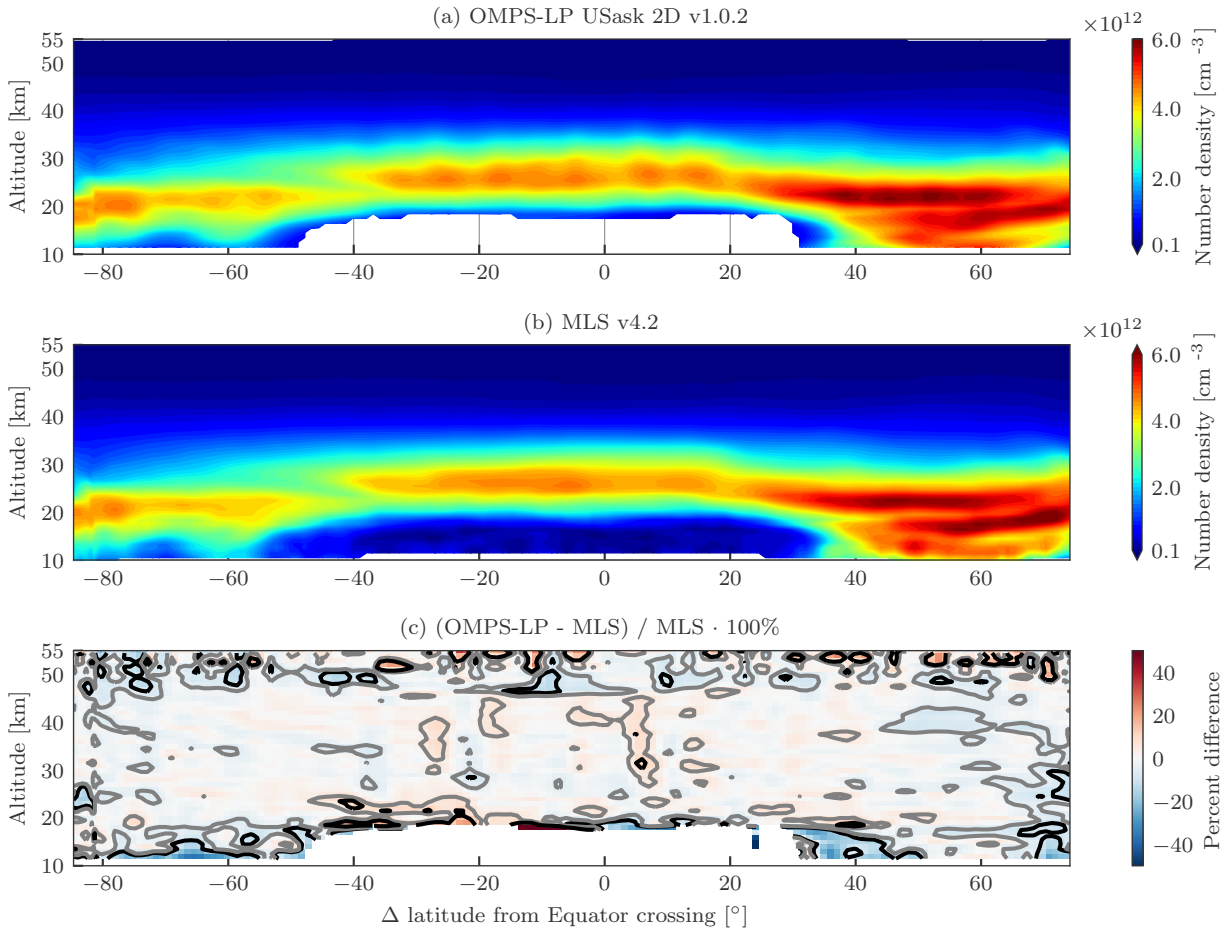

Figure 5.15: **(a)** shows the retrieved ozone field for OMPS-LP orbit 11915 (14 February 2014, 04:35 UTC at Equator crossing) from the USask 2D v1.0.2 retrieval; **(b)** shows the corresponding coincident MLS v4.2 retrieved values for the coincident measurements shown in Fig. 5.14; and **(c)** shows the percent difference between the two, with gray and black contours indicating the ±5 and ±10 % levels, respectively.

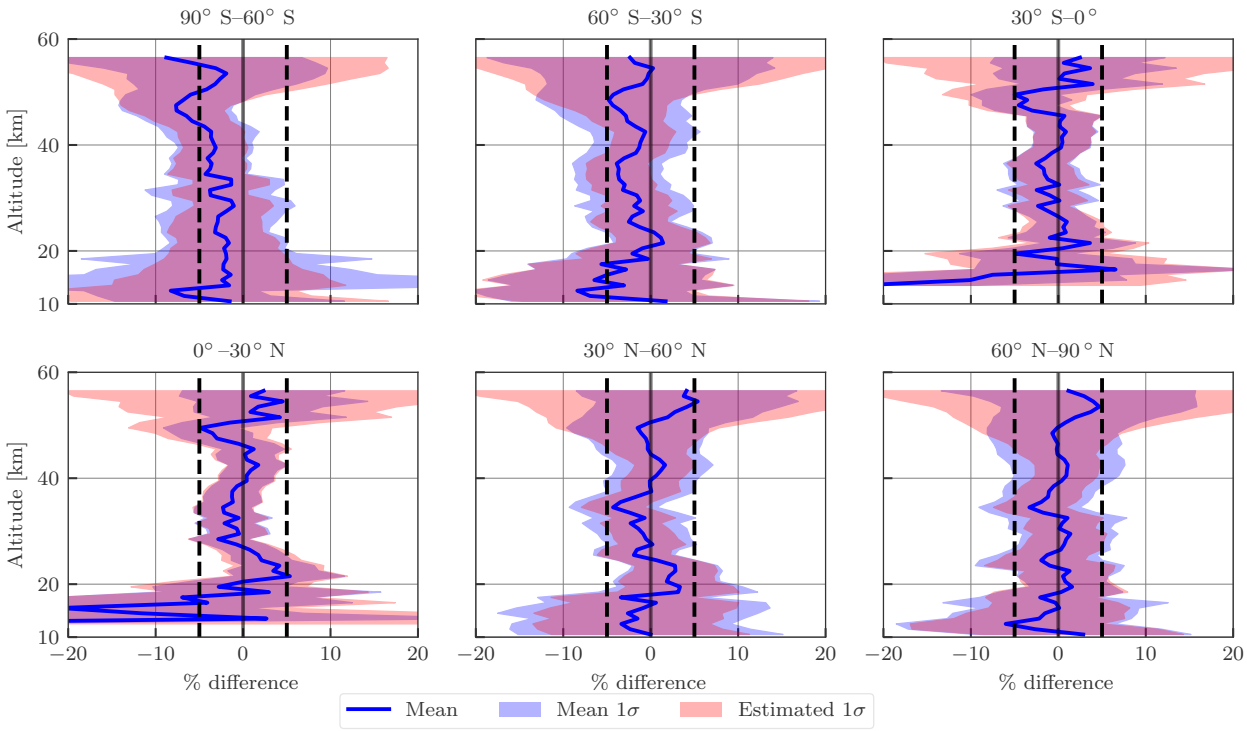

Figure 5.16: Mean differences ((OMPS-LP − MLS) / MLS · 100 %) in latitude bins for all coincident orbits between 2012 and 2013 (see text for coincidence criteria). The shaded blue region shows the SD of the differences, while the shaded red region is the predicted SD using the precision estimate from both retrievals. Dashed vertical lines indicate the ±5 % levels.

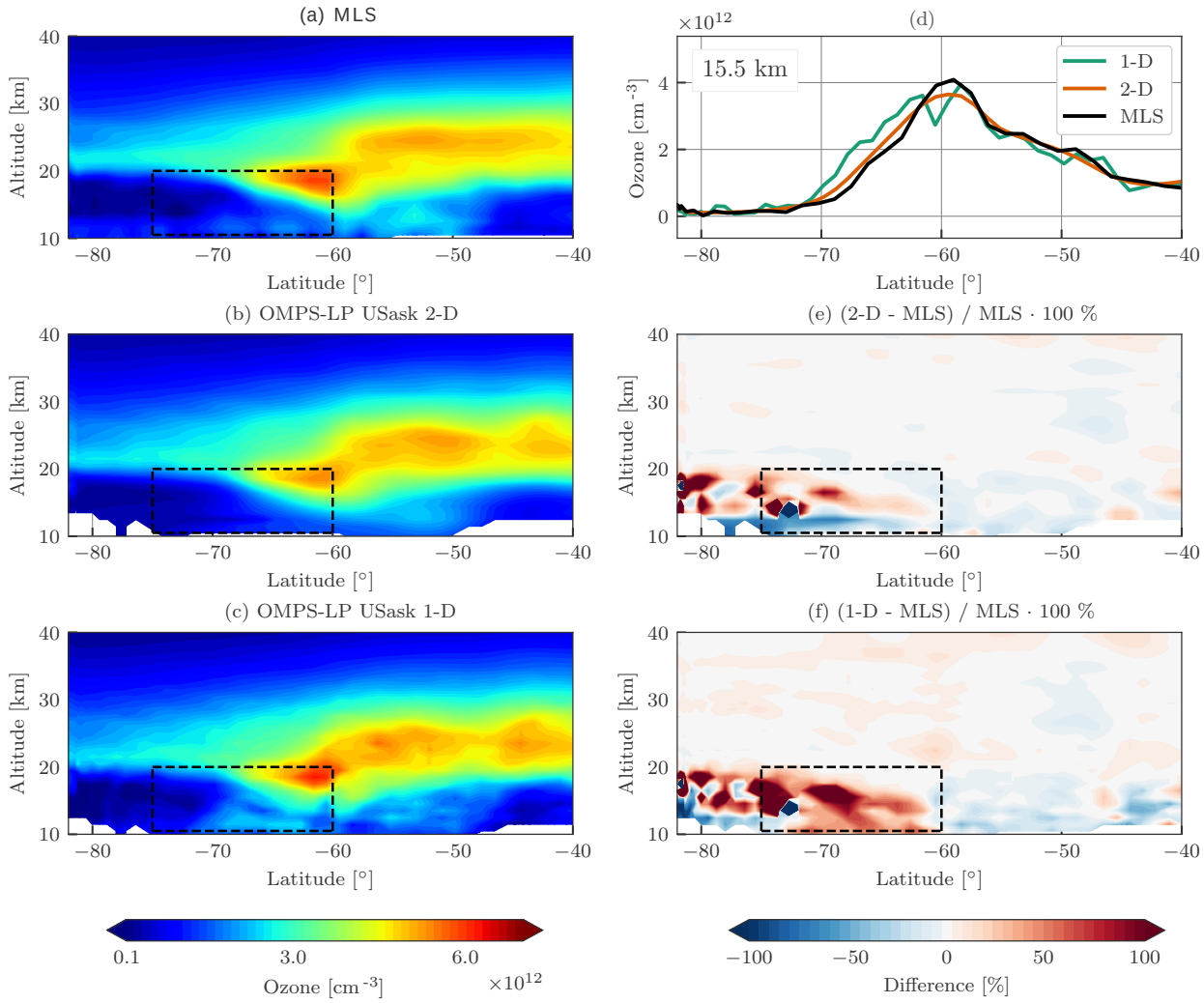

Figure 5.17: Retrieval results for OMPS-LP orbit 20657 (23 October 2015, 08:50 UTC at Equator crossing) near the polar vortex. The left column shows the coincident MLS v4.2 ozone **(a)**, tomographically retrieved ozone **(b)**, and one-dimensionally retrieved ozone **(c)**. The right column contains a horizontal slice of the retrieved ozone at 15.5 km **(d)**, the percent difference between the tomographic retrieval and MLS **(e)**, and the percent difference between the one-dimensionally retrieved ozone and MLS **(f)**. For the percent-difference panels, contours are shown every ±5 %. The dashed black box indicates the area in which the two-dimensional retrieval is expected to show improvement based upon the simulations of Sect. 5.6.1.

Chapter 6

Summary and Outlook

Satellite based limb scatter measurements have been successively used to obtain vertical profiles of trace species in the atmosphere for decades. Most limb retrievals assume horizontal homogeneity, the assumption that the atmosphere varies only in the vertical dimension. Horizontal homogeneity breaks down in regions of large horizontal gradients such as the polar vortex region. Some limb emission retrievals have broken horizontal homogeneity by performing tomographic retrievals, where multiple images are combined together to simultaneously retrieve in the vertical and along orbital track dimension. Until now, only proof of concept studies have been performed for tomographic retrievals from limb scatter instruments due to the complication of multiple scattering within the Earth's atmosphere.

This work has demonstrated the first fully tomographic retrieval of ozone using limb scatter measurements. The work naturally splits into three parts. The first is the development of an efficient radiative transfer model, SASKTRAN-HR, that is capable of handling gradient in the along line of sight direction. Second is the implementation of an efficient Jacobian calculation within SASKTRAN-HR that is suitable for atmospheric tomography. Lastly, the tomographic retrieval algorithm and the application to measurements from OMPS-LP is presented.

SASKTRAN-HR is the first non Monte Carlo radiative transfer model that can handle two- or three-dimensional atmospheres. The model includes numerous accuracy improvements over standard successive orders models, including an adaptive integration procedure to handle areas of large extinction. Extensive comparisons have been done between SASKTRAN-HR and a reference Monte Carlo model which indicate that it is accurate to within 0.2% for almost all solar and atmospheric conditions. SASKTRAN-HR was used to identify a bias in the OSIRIS ozone product that depended on whether or not the instrument

was scanning up or down, and has also been used in a wide variety of projects unrelated to the present work.

The ability to analytically calculate approximate weighting functions was also implemented within SASKTRAN-HR. This was performed by directly evaluating the derivative of the radiative transfer equation with respect to atmospheric parameters, neglecting terms that are high order with respect to scattering extinction. The weighting functions were validated by comparing to perturbation methods, and were found to be significantly better than those calculated with a single scatter approximation. The analytic approximation was also found to be orders of magnitude faster than perturbation methods.

The core of the thesis is the development of a tomographic retrieval algorithm and its application to retrieve ozone from OMPS-LP limb scatter measurements. Both SASKTRAN-HR and the fast Jacobian calculations described are key components of the algorithm. The algorithm combines spectral measurements from an entire orbit of OMPS-LP to simultaneously retrieve a two-dimensional ozone field in altitude and angle along the orbital track. The estimated resolution of the retrieval is 1–2 km in the vertical dimension, and 300–400 km in the along track dimension. Simulated retrievals were performed that indicate the traditional one-dimensional retrievals have a bias in the polar vortex region that is eliminated with a two-dimensional retrieval.

The tomographic retrieval was applied to all measurements available from OMPS-LP to create a publicly available six year dataset of stratospheric ozone. Preliminary comparisons indicate that the retrieval agrees with MLS at the approximate 5% level for most atmospheric conditions. In the polar vortex region it was also observed that the one-dimensional retrieval exhibits similar biases compared to MLS that were expected from the simulated retrievals. Similar biases were not seen between MLS and the two-dimensional retrieval suggesting that the tomographic retrieval is correctly handling gradients in the along line of sight direction.

A natural continuation of the present work would be a full validation study of the produced OMPS-LP dataset. Preliminary comparisons have been performed against MLS which demonstrated the applicability of the two-dimensional technique; however, long term stability of the data has yet to be assessed. Estimates of the long term stability and potential to correct any identified drifts in the data product would prove useful for future studies

attempting to quantify long term ozone changes in the stratosphere.

A useful future research direction would be to demonstrate that a tomographic retrieval can in fact obtain better horizontal resolution than a one-dimensional retrieval. It was shown that a two-dimensional retrieval is capable of reducing biases in areas of large horizontal gradients such as the polar vortex. However, the obtained horizontal resolution was 300–400 km, which is comparable to similar one-dimensional retrievals. Measurements from future instruments that sample the along-track dimension significantly faster than OMPS-LP could be used to attempt to retrieve structure at the sub 100 km level. These studies will be of particular importance for future limb instruments whose goals are to study small scale transport/dynamical processes in the UTLS region.

While the focus of this work was to perform a tomographic retrieval of ozone from limb scatter measurements, the general techniques are applicable to the retrieval of any species that can be seen in limb scatter spectra. The most natural species to investigate further would be stratospheric aerosol from OMPS-LP, of which a preliminary retrieval was already developed to constrain the ozone field. Directly retrieving along line of sight structure may prove to be very important for stratospheric aerosol since large horizontal gradients can be observed in the plume post volcanic eruption. A tomographic retrieval of NO_2 would also be of particular interest as large horizontal gradients present from the strong diurnal cycle. Two-dimensional retrievals will also be a necessity for future instruments such as SHOW which targets sub 100 km horizontal resolution for UTLS water vapour.

References

Ball, W. T., Alsing, J., Mortlock, D. J., Staehelin, J., Haigh, J. D., Peter, T., Tummon, F., Stübi, R., Stenke, A., Anderson, J., Bourassa, A., Davis, S. M., Degenstein, D., Frith, S., Froidevaux, L., Roth, C., Sofieva, V., Wang, R., Wild, J., Yu, P., Ziemke, J. R., & Rozanov, E. V. (2018). Evidence for a continuous decline in lower stratospheric ozone offsetting ozone layer recovery. *Atmospheric Chemistry and Physics*, *18*(2), 1379–1394. doi:10.5194/acp-18-1379-2018

Bates, D. (1984). Rayleigh scattering by air. *Planetary and Space Science*, *32*(6), 785–790. doi:10.1016/0032-0633(84)90102-8

Bernath, P. F., McElroy, C. T., Abrams, M. C., Boone, C. D., Butler, M., Camy-Peyret, C., Carleer, M., Clerbaux, C., Coheur, P. F., Colin, R., DeCola, P., DeMazière, M., Drummond, J. R., Dufour, D., Evans, W. F., Fast, H., Fussen, D., Gilbert, K., Jennings, D. E., Llewellyn, E. J., Lowe, R. P., Mahieu, E., McConnell, J. C., McHugh, M., McLeod, S. D., Michaud, R., Midwinter, C., Nassar, R., Nichitiu, F., Nowlan, C., Rinsland, C. P., Rochon, Y. J., Rowlands, N., Semeniuk, K., Simon, P., Skelton, R., Sloan, J. J., Soucy, M. A., Strong, K., Tremblay, P., Turnbull, D., Walker, K. A., Walkty, I., Wardle, D. A., Wehrle, V., Zander, R., & Zou, J. (2005). Atmospheric chemistry experiment (ACE): Mission overview. Wiley-Blackwell. doi:10.1029/2005GL022386

Bhartia, P. K., McPeters, R. D., Flynn, L. E., Taylor, S., Kramarova, N. A., Frith, S., Fisher, B., & DeLand, M. (2013). Solar Backscatter UV (SBUV) total ozone and profile algorithm. *Atmospheric Measurement Techniques*, *6*(10), 2533–2548. doi:10.5194/amt-6-2533-2013

Bourassa, A. E., Degenstein, D. A., Gattinger, R. L., & Llewellyn, E. J. (2007). Stratospheric aerosol retrieval with optical spectrograph and infrared imaging system limb

scatter measurements. *Journal of Geophysical Research*, *112*(D10), D10217. doi:10.1029/2006JD008079

Bourassa, A. E., Degenstein, D. A., Randel, W. J., Zawodny, J. M., Kyrölä, E., McLinden, C. A., Sioris, C. E., & Roth, C. Z. (2014). Trends in stratospheric ozone derived from merged SAGE II and Odin-OSIRIS satellite observations. *Atmospheric Chemistry and Physics*, *14*(13), 6983–6994. doi:10.5194/acp-14-6983-2014

Bourassa, A. E., McLinden, C. A., Sioris, C. E., Brohede, S., Bathgate, A. F., Llewellyn, E. J., & Degenstein, D. A. (2011). Fast NO_2 retrievals from Odin-OSIRIS limb scatter measurements. *Atmospheric Measurement Techniques*, *4*(5), 965–972. doi:10.5194/amt-4-965-2011

Bourassa, A. E., Rieger, L. A., Lloyd, N. D., & Degenstein, D. A. (2012). Odin-osiris stratospheric aerosol data product and sage iii intercomparison. *Atmospheric Chemistry and Physics*, *12*(1), 605–614. doi:10.5194/acp-12-605-2012

Bourassa, A., Degenstein, D., & Llewellyn, E. (2008). SASKTRAN: A spherical geometry radiative transfer code for efficient estimation of limb scattered sunlight. *Journal of Quantitative Spectroscopy and Radiative Transfer*, *109*(1), 52–73. doi:10.1016/j.jqsrt.2007.07.007

Bourassa, A. E., Roth, C. Z., Zawada, D. J., Rieger, L. A., McLinden, C. A., & Degenstein, D. A. (2018). Drift-corrected Odin-OSIRIS ozone product: algorithm and updated stratospheric ozone trends. *Atmospheric Measurement Techniques*, *11*(1), 489–498. doi:10.5194/amt-11-489-2018

Bovensmann, H., Burrows, J. P., Buchwitz, M., Frerick, J., Noël, S., Rozanov, V. V., Chance, K. V., & Goede, A. P. H. (1999). SCIAMACHY: Mission Objectives and Measurement Modes. *J. Atmos. Sci*, *56*, 127–150. doi:10.1175/1520-0469(1999)056<0127:SMOAMM>2.0.CO;2

Brewer, A. W. (1949). Evidence for a world circulation provided by the measurements of helium and water vapour distribution in the stratosphere. *Quarterly Journal of the Royal Meteorological Society*, *75*(326), 351–363. doi:10.1002/qj.49707532603

Brion, J., Chakir, A., Daumont, D., Malicet, J., & Parisse, C. (1993). High-resolution laboratory absorption cross section of O3. Temperature effect. *Chemical physics letters*, *213*(5-6), 610–612.

Butchart, N. (2014). The Brewer-Dobson circulation. *Reviews of Geophysics*, *52*(2), 157–184. doi:10.1002/2013RG000448

Carlotti, M., Brizzi, G., Papandrea, E., Prevedelli, M., Ridolfi, M., Dinelli, B. M., & Magnani, L. (2006). GMTR : Two-dimensional geo-fit multitarget retrieval model for Michelson Interferometer for Passive Atmospheric Sounding / Environmental Satellite observations. *Appl. Opt. 45*(4), 716–727. doi:10.1364/AO.45.000716

Ceccherini, S., & Ridolfi, M. (2010). Variance-covariance matrix and averaging kernels for the levenberg-marquardt solution of the retrieval of atmospheric vertical profiles. *Atmospheric Chemistry and Physics*, *10*(6), 3131–3139.

Chandrasekhar, S. (1960). *Radiative transfer*. Courier Dover Publications.

Chapman, S. (1930). XXXV. On ozone and atomic oxygen in the upper atmosphere. *The London, Edinburgh, and Dublin Philosophical Magazine and Journal of Science*, *10*(64), 369–383.

Chu, W. P., & McCormick, M. P. (1979). Inversion of stratospheric aerosol and gaseous constituents from spacecraft solar extinction data in the 0.38-1.0-µm wavelength region. *Applied Optics*, *18*(9), 1404–1413. doi:10.1364/AO.18.001404

Collins, D. G., Blättner, W. G., Wells, M. B., & Horak, H. G. (1972). Backward monte carlo calculations of the polarization characteristics of the radiation emerging from spherical-shell atmospheres. *Appl. Opt. 11*(11), 2684–2696. doi:10.1364/AO.11.002684

Daumont, D., Brion, J., Charbonnier, J., & Malicet, J. (1992). Ozone UV spectroscopy I: Absorption cross-sections at room temperature. *Journal of Atmospheric Chemistry*, *15*(2), 145–155.

Dee, D. P., Uppala, S. M., Simmons, A. J., Berrisford, P., Poli, P., Kobayashi, S., Andrae, U., Balmaseda, M. A., Balsamo, G., Bauer, P., Bechtold, P., Beljaars, A. C. M., van de Berg, L., Bidlot, J., Bormann, N., Delsol, C., Dragani, R., Fuentes, M., Geer, A. J., Haimberger, L., Healy, S. B., Hersbach, H., Hólm, E. V., Isaksen, L., Kållberg, P., Köhler, M., Matricardi, M., Mcnally, A. P., Monge-Sanz, B. M., Morcrette, J. J.,

Park, B. K., Peubey, C., de Rosnay, P., Tavolato, C., Thépaut, J. N., & Vitart, F. (2011). The ERA-Interim reanalysis: Configuration and performance of the data assimilation system. *Quarterly Journal of the Royal Meteorological Society*, *137*(656), 553–597. doi:10.1002/qj.828

Degenstein, D. A., Llewellyn, E. J., & Lloyd, N. D. (2004). Tomographic retrieval of the oxygen infrared atmospheric band with the OSIRIS infrared imager. *Canadian Journal of Physics*, *82*(7), 501–515. doi:10.1139/p04-024

Degenstein, D. A., Bourassa, A. E., Roth, C. Z., & Llewellyn, E. J. (2009). Limb scatter ozone retrieval from 10 to 60 km using a multiplicative algebraic reconstruction technique. *Atmospheric Chemistry and Physics*, *9*(17), 6521–6529. doi:10.5194/acp-9-6521-2009

Degenstein, D. A., Llewellyn, E. J., & Lloyd, N. D. (2003). Volume emission rate tomography from a satellite platform. *Applied optics*, *42*(8), 1441–1450.

Delaunay, B. (1934). Sur la sphère vide. a la mémoire de georges voronoï. *Bulletin de l'Académie des Sciences de l'URSS. Classe des sciences mathématiques et na*, *7*, 793–800.

Deshler, T., Hervig, M. E., Hofmann, D. J., Rosen, J. M., & Liley, J. B. (2003). Thirty years of in situ stratospheric aerosol size distribution measurements from Laramie, Wyoming (41°N), using balloon-borne instruments. *J. Geophys. Res. 108*, 4167. doi:10.1029/2002JD002514

Deutschmann, T., Beirle, S., Frieß, U., Grzegorski, M., Kern, C., Kritten, L., Platt, U., Prados-Román, C., Puķīte, J., Wagner, T., Werner, B., & Pfeilsticker, K. (2011). The monte carlo atmospheric radiative transfer model mcartim: Introduction and validation of jacobians and 3d features. *Journal of Quantitative Spectroscopy and Radiative Transfer*, *112*(6), 1119–1137. doi:10.1016/j.jqsrt.2010.12.009

Dobson, G. M. B. (1931). A photoelectric spectrophotometer for measuring the amount of atmospheric ozone. *Proceedings of the Physical Society*, *43*(3), 324–339. doi:10.1088/0959-5309/43/3/308

Dobson, G. M. B. (1956). Origin and Distribution of the Polyatomic Molecules in the Atmosphere. *Proceedings of the Royal Society A: Mathematical, Physical and Engineering Sciences*, *236*(1205), 187–193. doi:10.1098/rspa.1956.0127

Dowson, D., & Wragg, A. (1973). Maximum-entropy distributions having prescribed first and second moments (Corresp.) *IEEE Transactions on Information Theory*, *19*(September), 689–693. doi:10.1109/TIT.1973.1055060

Dueck, S. R., Bourassa, A. E., & Degenstein, D. A. (2017). An efficient algorithm for polarization in the SASKTRAN radiative transfer framework. *Journal of Quantitative Spectroscopy and Radiative Transfer*, *199*, 1–11. doi:10.1016/j.jqsrt.2017.05.016

Ebojie, F., Von Savigny, C., Ladstätter-Weißenmayer, A., Rozanov, A., Weber, M., Eichmann, K. U., Bötel, S., Rahpoe, N., Bovensmann, H., & Burrows, J. P. (2014). Tropospheric column amount of ozone retrieved from SCIAMACHY limb-nadir-matching observations. *Atmospheric Measurement Techniques*, *7*(7), 2073–2096. doi:10.5194/amt-7-2073-2014

Elash, B. J., Bourassa, A. E., Loewen, P. R., Lloyd, N. D., & Degenstein, D. A. (2016). The Aerosol Limb Imager: acousto-optic imaging of limb-scattered sunlight for stratospheric aerosol profiling. *Atmos. Meas. Tech. 9*(3), 1261–1277. doi:10.5194/amt-9-1261-2016

Elash, B., Bourassa, A., Rieger, L., Dueck, S., Zawada, D., & Degenstein, D. (2017). The sensitivity to polarization in stratospheric aerosol retrievals from limb scattered sunlight measurements. *Journal of Quantitative Spectroscopy and Radiative Transfer*, *189*, 75–85. doi:10.1016/j.jqsrt.2016.11.014

Farman, J. C., Gardiner, B. G., & Shanklin, J. D. (1985). Large losses of total ozone in Antarctica reveal seasonal ClO x /NO x interaction. *Nature*, *315*(6016), 207–210. doi:10.1038/315207a0

Fischer, H., Birk, M., Blom, C., Carli, B., Carlotti, M., von Clarmann, T., Delbouille, L., Dudhia, A., Ehhalt, D., Endemann, M., Flaud, J. M., Gessner, R., Kleinert, A., Koopman, R., Langen, J., López-Puertas, M., Mosner, P., Nett, H., Oelhaf, H., Perron, G., Remedios, J., Ridolfi, M., Stiller, G., & Zander, R. (2008). MIPAS: an instrument for atmospheric and climate research. *Atmospheric Chemistry and Physics*, *8*(8), 2151–2188. doi:10.5194/acp-8-2151-2008

Flittner, D. E., Bhartia, P. K., & Herman, B. M. (2000). O3 profiles retrieved from limb scatter measurements: Theory. *Geophysical Research Letters*, *27*(17), 2601–2604. doi:10.1029/1999GL011343

Flynn, L. E., Seftor, C. J., Larsen, J. C., & Xu, P. (2006). The ozone mapping and profiler suite. In *Earth science satellite remote sensing* (pp. 279–296). Springer.

Flynn, L., Hornstein, J., & Hilsenrath, E. (2004). The ozone mapping and profiler suite (OMPS). The next generation of US ozone monitoring instruments. *Geoscience and Remote Sensing Symposium, 2004. IGARSS '04. Proceedings. 2004 IEEE International*, *1*(100), 152–155. doi:10.1109/IGARSS.2004.1368968

Frith, S. M., Kramarova, N. A., Stolarski, R. S., McPeters, R. D., Bhartia, P. K., & Labow, G. J. (2014). Recent changes in total column ozone based on the SBUV Version 8.6 Merged Ozone Data Set. *Journal of Geophysical Research: Atmospheres*, *119*(16), 9735–9751. doi:10.1002/2014JD021889

Griffioen, E., & Oikarinen, L. (2000). LIMBTRAN: A pseudo three-dimensional radiative transfer model for the limb-viewing imager OSIRIS on the Odin satellite. *Journal of Geophysical Research: Atmospheres (1984–2012)*, *105*(D24), 29717–29730. doi:10.1029/2000JD900566

Haley, C., von Savigny, C., Brohede, S., Sioris, C., McDade, I., Llewellyn, E., & Murtagh, D. (2004). A comparison of methods for retrieving stratospheric ozone profiles from OSIRIS limb-scatter measurements. *Advances in Space Research*, *34*(4), 769–774. doi:10.1016/j.asr.2003.08.058

Harris, N. R. P., Hassler, B., Tummon, F., Bodeker, G. E., Hubert, D., Petropavlovskikh, I., Steinbrecht, W., Anderson, J., Bhartia, P. K., Boone, C. D., Bourassa, A., Davis, S. M., Degenstein, D., Delcloo, A., Frith, S. M., Froidevaux, L., Godin-Beekmann, S., Jones, N., Kurylo, M. J., Kyrölä, E., Laine, M., Leblanc, S. T., Lambert, J.-C., Liley, B., Mahieu, E., Maycock, A., de Mazière, M., Parrish, A., Querel, R., Rosenlof, K. H., Roth, C., Sioris, C., Staehelin, J., Stolarski, R. S., Stübi, R., Tamminen, J., Vigouroux, C., Walker, K. A., Wang, H. J., Wild, J., & Zawodny, J. M. (2015). Past changes in the vertical distribution of ozone – Part 3: Analysis and interpretation of trends. *Atmospheric Chemistry and Physics*, *15*(17), 9965–9982. doi:10.5194/acp-15-9965-2015

Janz, S. J., Hilsenrath, E., Flittner, D. E., & Heath, D. F. (1996). Rayleigh scattering attitude sensor. In R. E. Huffman & C. G. Stergis (Eds.), *Proc. spie* (Vol. 2831, pp. 146–153). International Society for Optics and Photonics. doi:10.1117/12.257207

Jaross, G., Bhartia, P. K., Chen, G., Kowitt, M., Haken, M., Chen, Z., Xu, P., Warner, J., & Kelly, T. (2014). OMPS Limb Profiler instrument performance assessment. *Journal of Geophysical Research: Atmospheres*, *119*(7), 4399–4412. doi:10.1002/2013JD020482

Junge, C. E., Chagnon, C. W., & Manson, J. E. (1961). Stratospheric aerosols. *Journal of Meteorology*, *18*(1), 81–108.

Kaiser, J. W., & Burrows, J. P. (2003). Fast weighting functions for retrievals from limb scattering measurements. *Journal of Quantitative Spectroscopy and Radiative Transfer*, *77*(3), 273–283. doi:10.1016/S0022-4073(02)00125-5

Kiefer, M., Arnone, E., Dudhia, A., Carlotti, M., Castelli, E., von Clarmann, T., Dinelli, B. M., Kleinert, A., Linden, A., Milz, M., Papandrea, E., & Stiller, G. (2010). Impact of temperature field inhomogeneities on the retrieval of atmospheric species from MIPAS IR limb emission spectra. *Atmospheric Measurement Techniques*, *3*(5), 1487–1507. doi:10.5194/amt-3-1487-2010

King, L. V. (1923). On the Complex Anisotropic Molecule in Relation to the Dispersion and Scattering of Light. *Proceedings of the Royal Society A: Mathematical, Physical and Engineering Sciences*, *104*(726), 333–357. doi:10.1098/rspa.1923.0113

Kyrölä, E., Tamminen, J., Leppelmeier, G. W., Sofieva, V., Hassinen, S., Bertaux, J. L., Hauchecorne, A., Dalaudier, F., Cot, C., Korablev, O., Fanton d'Andon, O., Barrot, G., Mangin, A., Théodore, B., Guirlet, M., Etanchaud, F., Snoeij, P., Koopman, R., Saavedra, L., Fraisse, R., Fussen, D., & Vanhellemont, F. (2004). GOMOS on Envisat: An overview. *Advances in Space Research*, *33*(7), 1020–1028. doi:10.1016/S0273-1177(03)00590-8

Langille, J., Letros, D., Zawada, D., Bourassa, A., Degenstein, D., & Solheim, B. (2018). Spatial Heterodyne Observations of Water (SHOW) vapour in the upper troposphere and lower stratosphere from a high altitude aircraft: Modelling and sensitivity analysis. *Journal of Quantitative Spectroscopy and Radiative Transfer*, *209*, 137–149. doi:10.1016/J.JQSRT.2018.01.026

Levenberg, K. (1944). A method for the solution of certain non-linear problems in least squares. *Quarterly of Applied Mathematics*, *2*(2), 164–168.

Livesey, N. J., & Read, W. G. (2000). Direct retrieval of line-of-sight atmospheric structure from limb sounding observations. *Geophysical Research Letters*, *27*(6), 891–894. doi:10.1029/1999GL010964

Livesey, N. J., Read, W. G., Wagner, P. A., Froidevaux, L., Lambert, A., Manney, G. L., Millan-Valle, L. F., Pumphrey, H. C., Santee, M. L., Schwartz, M. J., Wang, S., Fuller, R. A., Jarnot, R. F., Knosp, B. W., & Martinez, E. (2017). *Version 4.2x level 2 data quality and description document.* (tech. rep. No. JPL D-33509). NASA Jet Propulsion Laboratory. Version 4.2x–3.0.

Livesey, N. J., Van Snyder, W., Read, W. G., & Wagner, P. A. (2006). Retrieval algorithms for the EOS Microwave Limb Sounder (MLS). *IEEE Transactions on Geoscience and Remote Sensing*, *44*(5), 1144–1155. doi:10.1109/TGRS.2006.872327

Llewellyn, E. J., Lloyd, N. D., Degenstein, D. A., Gattinger, R. L., Petalina, S. V., Bourassa, A. E., Wiensz, J. T., Ivanov, E. V., McDade, I. C., Solheim, B. H., McConnell, J. C., Haley, C. S., von Savigny, C., Sioris, C. E., McLinden, C. A., Griffioen, E., Kaminski, J., Evans, W. F. J., Puckrin, E., Strong, K., Wehrle, V., Hum, R. H., Kendall, D. J. W., Matsushita, J., Murtagh, D. P., Brohede, S., Stegman, J., Witt, G., Barnes, G., Payne, W. F., Piche, L., Smith, K., Warshaw, G., Deslauniers, D. .-.-L., Marchand, P., Richardson, E. H., King, R. A., Wevers, I., McCreath, W., Kyrölä, E., Oikarinen, L., Leppelmeier, G. W., Auvinen, H., Megle, G., Hauchecorne, A., Lefevre, F., de La Noe, J., Ricaud, P., Frisk, U., Sjoberg, F., von Scheele, F., & Nordh, L. (2004). The OSIRIS instrument on the Odin spacecraft. *Canadian Journal of Physics*, *82:6, s. 4*, 411–422.

Loughman, R. P., Flittner, D. E., Herman, B. M., Bhartia, P. K., Hilsenrath, E., & McPeters, R. D. (2005). Description and sensitivity analysis of a limb scattering ozone retrieval algorithm. *Journal of Geophysical Research*, *110*(D19), D19301. doi:10.1029/2004JD005429

Loughman, R. P., Griffioen, E., Oikarinen, L., Postylyakov, O. V., Rozanov, A., Flittner, D. E., & Rault, D. F. (2004). Comparison of radiative transfer models for limb-viewing scattered sunlight measurements. *Journal of Geophysical Research: Atmospheres*, *109*(D6). doi:10.1029/2003JD003854

Loughman, R., Flittner, D., Nyaku, E., & Bhartia, P. (2015). Gauss–seidel limb scattering (gsls) radiative transfer model development in support of the ozone mapping and profiler suite (omps) limb profiler mission. *Atmospheric Chemistry and Physics*, *15*(6), 3007–3020.

Malicet, J., Daumont, D., Charbonnier, J., Parisse, C., Chakir, A., & Brion, J. (1995). Ozone UV spectroscopy. II. Absorption cross-sections and temperature dependence. *Journal of atmospheric chemistry*, *21*(3), 263–273.

Marquardt, D. W. (1963). An algorithm for least-squares estimation of nonlinear parameters. *Journal of the society for Industrial and Applied Mathematics*, *11*(2), 431–441.

Mauldin III, L. E., Zaun, N. H., McCormick, M. P., Jr., Guy, J. H., & Vaughn, W. R. (1985). Stratospheric aerosol and gas experiment ii instrument: A functional description. *Optical Engineering*, *24*(2), 242307-242307-. doi:10.1117/12.7973473

Mauldin, L. E., Salikhov, R., Habib, S., Vladimirov, A. G., Carraway, D., Petrenko, G., & Comella, J. (1998). Meteor-3M(1)/Stratospheric Aerosol and Gas Experiment III (SAGE III) jointly sponsored by the National Aeronautics and Space Administration and the Russian Space Agency. (p. 355). International Society for Optics and Photonics. doi:10.1117/12.317767

McCormick, M. P., Hamill, P., Chu, W. P., Swissler, T. J., McMaster, L. R., Pepin, T. J., McCormick, M. P., Hamill, P., Pepin, T. J., Chu, W. P., Swissler, T. J., & McMaster, L. R. (1979). Satellite Studies of the Stratospheric Aerosol. *Bulletin of the American Meteorological Society*, *60*(9), 1038–1046. doi:10.1175/1520-0477(1979)060<1038:SSOTSA>2.0.CO;2

McLinden, C. A., Haley, C. S., & Sioris, C. E. (2006). Diurnal effects in limb scatter observations. *Journal of Geophysical Research*, *111*(D14), D14302. doi:10.1029/2005JD006628

McLinden, C. A., & Bourassa, A. E. (2010). A Systematic Error in Plane-Parallel Radiative Transfer Calculations. *Journal of the Atmospheric Sciences*, *67*(5), 1695–1699. doi:10.1175/2009JAS3322.1

McPeters, R., Labow, G., & Johnson, B. (1997). A satellite-derived ozone climatology for balloonsonde estimation of total column ozone. *Journal of Geophysical Research: Atmospheres*, *102*(D7), 8875–8885.

Mie, G. (1908). Beiträge zur Optik trüber Medien, speziell kolloidaler Metallösungen. *Annalen der physik*, *330*(3), 377–445.

Mishchenko, M. I. (2008). Multiple scattering, radiative transfer, and weak localization in discrete random media: Unified microphysical approach. *Reviews of Geophysics*, *46*(2), RG2003. doi:10.1029/2007RG000230

Mishchenko, M. I., Hovenier, J. W., & Travis, L. D. (1999). *Light scattering by nonspherical particles: theory, measurements, and applications*. Academic press.

Molina, M. J., & Rowland, F. S. (1974). Stratospheric sink for chlorofluoromethanes: chlorine atom-catalysed destruction of ozone. *Nature*, *249*(5460), 810–812. doi:10.1038/249810a0

Moy, L., Bhartia, P. K., Jaross, G., Loughman, R., Kramarova, N., Chen, Z., Taha, G., Chen, G., & Xu, P. (2017). Altitude registration of limb-scattered radiation. *Atmospheric Measurement Techniques*, *10*(1), 167–178. doi:10.5194/AMT-10-167-2017

Murtagh, D., Frisk, U., Merino, F., Ridal, M., Jonsson, A., Stegman, J., Witt, G., Jiménez, C., Megie, G., Noë, J. D., Ricaud, P., Baron, P., Pardo, J. R., Llewellyn, E. J., Degenstein, D. A., Gattinger, R. L., Lloyd, N. D., Evans, W. F. J., McDade, I. C., Haley, C. S., Sioris, C. E., Savigny, V., Solheim, B. H., McConnell, J. C., Richardson, E. H., Leppelmeier, G. W., Auvinen, H., & Oikarinen, L. (2002). An overview of the Odin atmospheric mission. *Canadian Journal of Physics*, *80*, 309–318. doi:10.1139/P01-157

Oikarinen, L., Sihvola, E., & Kyrölä, E. (1999). Multiple scattering radiance in limb-viewing geometry. *Journal of Geophysical Research: Atmospheres*, *104*(D24), 31261–31274. doi:10.1029/1999JD900969

Olsen, M. A., Douglass, A. R., Newman, P. A., Gille, J. C., Nardi, B., Yudin, V. A., Kinnison, D. E., & Khosravi, R. (2008). HIRDLS observations and simulation of a lower stratospheric intrusion of tropical air to high latitudes. *Geophysical Research Letters*, *35*(21), L21813. doi:10.1029/2008GL035514

Olson, G. L., & Kunasz, P. (1987). Short characteristic solution of the non-LTE line transfer problem by operator perturbation-I. The one-dimensional planar slab. *Journal of Quantitative Spectroscopy and Radiative Transfer*, *38*(5), 325–336. doi:10.1016/0022-4073(87)90027-6

Palmer, K. F., & Williams, D. (1975). Optical constants of sulfuric acid; application to the clouds of venus? *Applied Optics*, *14*(1), 208–219.

Papandrea, E., Arnone, E., Brizzi, G., Carlotti, M., Castelli, E., Dinelli, B. M., & Ridolfi, M. (2010). Two-dimensional tomographic retrieval of MIPAS/ENVISAT measurements of ozone and related species. *International Journal of Remote Sensing*, *31*(July 2016), 477–483. doi:10.1080/01431160902893501

Postylyakov, O. (2004). Radiative transfer model mcc++ with evaluation of weighting functions in spherical atmosphere for use in retrieval algorithms. *Advances in Space Research*, *34*(4), 721–726. Trace Constituents in the Troposphere and Lower Stratosphere. doi:10.1016/j.asr.2003.07.070

Puķıte, J., Kühl, S., Deutschmann, T., Platt, U., & Wagner, T. (2008). Accounting for the effect of horizontal gradients in limb measurements of scattered sunlight. *Atmos. Chem. Phys. 8*(12), 3045–3060. doi:10.5194/acp-8-3045-2008

Randel, W. J., Wu, F., Vömel, H., Nedoluha, G. E., & Forster, P. (2006). Decreases in stratospheric water vapor after 2001: Links to changes in the tropical tropopause and the Brewer-Dobson circulation. *Journal of Geophysical Research*, *111*(D12), D12312. doi:10.1029/2005JD006744

Rault, D., & Loughman, R. (2013a). The OMPS Limb Profiler Environmental Data Record Algorithm Theoretical Basis Document and Expected Performance. *Geoscience and Remote Sensing, IEEE Transactions on*, *51*(5), 2505–2527. doi:10.1109/TGRS.2012.2213093

Rault, D. F. (2005). Ozone profile retrieval from Stratospheric Aerosol and Gas Experiment (SAGE III) limb scatter measurements. *Journal of Geophysical Research D: Atmospheres*, *110*(9), 1–14. doi:10.1029/2004JD004970

Rault, D. F., & Loughman, R. P. (2013b). The OMPS Limb Profiler Environmental Data Record Algorithm Theoretical Basis Document and Expected Performance. *IEEE Transactions on Geoscience and Remote Sensing*, *51*(5), 2505–2527. doi:10.1109/TGRS.2012.2213093

Rault, D. F., & Spurr, R. (2010). The OMPS Limb Profiler instrument: two-dimensional retrieval algorithm. In *Remote sensing* (78270P–78270P). International Society for Optics and Photonics.

Rodgers, C. D. (2000). *Inverse methods for atmospheric sounding: theory and practice*. World scientific.

Rozanov, A., Bovensmann, H., Bracher, A., Hrechanyy, S., Rozanov, V., Sinnhuber, M., & Stroh, F. (2005). NO2 and BrO vertical profile retrieval from SCIAMACHY limb measurements: Sensitivity studies. *Advances in Space Research*, *36*(5), 846–854. doi:10.1016/j.asr.2005.03.013

Rozanov, A., Eichmann, K.-U., von Savigny, C., Bovensmann, H., Burrows, J. P., von Bargen, A., Doicu, A., Hilgers, S., Godin-Beekmann, S., Leblanc, T., & McDermid, I. S. (2007). Comparison of the inversion algorithms applied to the ozone vertical profile retrieval from SCIAMACHY limb measurements. *Atmospheric Chemistry and Physics*, *7*(18), 4763–4779. doi:10.5194/acp-7-4763-2007

Rozanov, A., Kühl, S., Doicu, A., McLinden, C., Puķīte, J., Bovensmann, H., Burrows, J. P., Deutschmann, T., Dorf, M., Goutail, F., Grunow, K., Hendrick, F., von Hobe, M., Hrechanyy, S., Lichtenberg, G., Pfeilsticker, K., Pommereau, J. P., Van Roozendael, M., Stroh, F., & Wagner, T. (2011a). BrO vertical distributions from SCIAMACHY limb measurements: comparison of algorithms and retrieval results. *Atmospheric Measurement Techniques*, *4*(7), 1319–1359. doi:10.5194/amt-4-1319-2011

Rozanov, A., Weigel, K., Bovensmann, H., Dhomse, S., Eichmann, K. U., Kivi, R., Rozanov, V., Vömel, H., Weber, M., & Burrows, J. P. (2011b). Retrieval of water vapor vertical distributions in the upper troposphere and the lower stratosphere from SCIAMACHY limb measurements. *Atmos. Meas. Tech.* *4*(5), 933–954. doi:10.5194/amt-4-933-2011

Rozanov, A., Weigel, K., Bovensmann, H., Dhomse, S., Eichmann, K.-U., Kivi, R., Rozanov, V., Vömel, H., Weber, M., & Burrows, J. P. (2011c). Retrieval of water vapor vertical distributions in the upper troposphere and the lower stratosphere from SCIAMACHY limb measurements. *Atmospheric Measurement Techniques*, *4*(5), 933–954. doi:10.5194/amt-4-933-2011

Rozanov, V. V., Rozanov, A. V., Kokhanovsky, A. A., & Burrows, J. P. (2014). Radiative transfer through terrestrial atmosphere and ocean: software package SCIATRAN. *Journal of Quantitative Spectroscopy and Radiative Transfer*, *133*, 13–71.

Rozanov, V. V., & Rozanov, A. V. (2007). Relationship between different approaches to derive weighting functions related to atmospheric remote sensing problems. *Journal of Quantitative Spectroscopy and Radiative Transfer*, *105*(2), 217–242. doi:10.1016/j.jqsrt.2006.12.006

Russell, J. M., Gordley, L. L., Park, J. H., Drayson, S. R., Hesketh, W. D., Cicerone, R. J., Tuck, A. F., Frederick, J. E., Harries, J. E., & Crutzen, P. J. (1993). The Halogen Occultation Experiment. *Journal of Geophysical Research*, *98*(D6), 10777–10797. doi:10.1029/93JD00799. arXiv: arXiv:1011.1669v3

Sheese, P. E., Llewellyn, E. J., Gattinger, R. L., Bourassa, A. E., Degenstein, D. A., Lloyd, N. D., & McDade, I. C. (2010). Temperatures in the upper mesosphere and lower thermosphere from OSIRIS observations of O 2 A-band emission spectra. *Canadian Journal of Physics*, *88*(12), 919–925. doi:10.1139/p10-093

Sioris, C. E., Rieger, L. A., Lloyd, N. D., Bourassa, A. E., Roth, C. Z., Degenstein, D. A., Camy-Peyret, C., Pfeilsticker, K., Berthet, G., Catoire, V., Goutail, F., Pommereau, J. P., & McLinden, C. A. (2017). Improved OSIRIS NO2 retrieval algorithm: Description and validation. *Atmospheric Measurement Techniques*, *10*(3), 1155–1168. doi:10.5194/amt-10-1155-2017

Sofieva, V. F., Kyrölä, E., Laine, M., Tamminen, J., Degenstein, D., Bourassa, A., Roth, C., Zawada, D., Weber, M., Rozanov, A. et al. (2017). Merged sage ii, ozone_cci and omps ozone profile dataset and evaluation of ozone trends in the stratosphere. *Atmospheric Chemistry and Physics*, *17*(20), 12533–12552.

Solomon, S. (1999). Stratospheric ozone depletion: A review of concepts and history. *Reviews of Geophysics*, *37*(3), 275–316. doi:10.1029/1999RG900008

Sonkaew, T., Rozanov, V. V., von Savigny, C., Rozanov, A., Bovensmann, H., & Burrows, J. P. (2009). Cloud sensitivity studies for stratospheric and lower mesospheric ozone profile retrievals from measurements of limb-scattered solar radiation. *Atmospheric Measurement Techniques*, *2*(2), 653–678. doi:10.5194/amt-2-653-2009

Spurr, R. (2002). Simultaneous derivation of intensities and weighting functions in a general pseudo-spherical discrete ordinate radiative transfer treatment. *Journal of Quantitative Spectroscopy and Radiative Transfer*, *75*(2), 129–175. doi:10.1016/S0022-4073(01)00245-X

Spurr, R. J. (2006). Vlidort: A linearized pseudo-spherical vector discrete ordinate radiative transfer code for forward model and retrieval studies in multilayer multiple scattering media. *Journal of Quantitative Spectroscopy and Radiative Transfer*, *102*(2), 316–342. doi:https://doi.org/10.1016/j.jqsrt.2006.05.005

Stamnes, K., Tsay, S.-C., Wiscombe, W., & Laszlo, I. (2000). DISORT, a general-purpose Fortran program for discrete-ordinate-method radiative transfer in scattering and emitting layered media: documentation of methodology. *Goddard Space Flight Center, NASA*.

Steck, T., Höpfner, M., von Clarmann, T., & Grabowski, U. (2005). Tomographic Retrieval of Atmospheric Parameters From Infrared Limb Emission Observations. *Applied Optics*, *44*(16), 3291–3301.

Steinbrecht, W., Froidevaux, L., Fuller, R., Wang, R., Anderson, J., Roth, C., Bourassa, A., Degenstein, D., Damadeo, R., Zawodny, J., Frith, S., McPeters, R., Bhartia, P., Wild, J., Long, C., Davis, S., Rosenlof, K., Sofieva, V., Walker, K., Rahpoe, N., Rozanov, A., Weber, M., Laeng, A., Von Clarmann, T., Stiller, G., Kramarova, N., Godin-Beekmann, S., Leblanc, T., Querel, R., Swart, D., Boyd, I., Hocke, K., Kämpfer, N., Maillard Barras, E., Moreira, L., Nedoluha, G., Vigouroux, C., Blumenstock, T., Schneider, M., García, O., Jones, N., Mahieu, E., Smale, D., Kotkamp, M., Robinson, J., Petropavlovskikh, I., Harris, N., Hassler, B., Hubert, D., & Tummon, F. (2017). An update on ozone profile trends for the period 2000 to 2016. *Atmospheric Chemistry and Physics*, *17*(17), 10675–10690. doi:10.5194/acp-17-10675-2017

Taha, G., Rault, D. F., Loughman, R. P., Bourassa, A. E., & Von Savigny, C. (2011). SCIAMACHY stratospheric aerosol extinction profile retrieval using the OMPS/LP algorithm. *Atmospheric Measurement Techniques*, *4*(3), 547–556. doi:10.5194/amt-4-547-2011

Tamminen, J., & Kyrölä, E. (2001). Bayesian solution for nonlinear and non-Gaussian inverse problems by Markov chain Monte Carlo method. *Journal of Geophysical Research: Atmospheres*, *106*(D13), 14377–14390. doi:10.1029/2001JD900007

Tikhonov, A. N. (1943). On the stability of inverse problems. In *Dokl. akad. nauk sssr* (Vol. 39, *5*, pp. 195–198).

Veach, E., & Guibas, L. J. (1995). Optimally combining sampling techniques for monte carlo rendering. SIGGRAPH '95, 419–428. doi:10.1145/218380.218498

Von Clarmann, T. (2014). Smoothing error pitfalls. *Atmospheric Measurement Techniques*, *7*(9), 3023–3034. doi:10.5194/amt-7-3023-2014

von Clarmann, T., De Clercq, C., Ridolfi, M., Höpfner, M., & Lambert, J.-C. (2008). The horizontal resolution of MIPAS. *Atmos. Meas. Tech. Discuss. 1*(1), 103–125. doi:10.5194/amtd-1-103-2008

von Clarmann, T., Glatthor, N., Grabowski, U., Höpfner, M., Kellmann, S., Kiefer, M., Linden, A., Tsidu, G. M., Milz, M., Steck, T., Stiller, G. P., Wang, D. Y., Fischer, H., Funke, B., Gil-López, S., & López-Puertas, M. (2003). Retrieval of temperature and tangent altitude pointing from limb emission spectra recorded from space by the Michelson Interferometer for Passive Atmospheric Sounding (MIPAS). *Journal of Geophysical Research*, *108*(D23), 4736. doi:10.1029/2003JD003602

von Savigny, C., Haley, C. S., Sioris, C. E., McDade, I. C., Llewellyn, E. J., Degenstein, D., Evans, W. F. J., Gattinger, R. L., Griffioen, E., Kyrölä, E., Lloyd, N. D., McConnell, J. C., McLinden, C. A., Mégie, G., Murtagh, D. P., Solheim, B., & Strong, K. (2003). Stratospheric ozone profiles retrieved from limb scattered sunlight radiance spectra measured by the OSIRIS instrument on the Odin satellite. *Geophysical Research Letters*, *30*(14), 1755. doi:10.1029/2002GL016401

von Savigny, C., Rozanov, A., Bovensmann, H., Eichmann, K.-U., Noël, S., Rozanov, V., Sinnhuber, B.-M., Weber, M., Burrows, J. P., & Kaiser, J. W. (2005). The ozone hole breakup in september 2002 as seen by SCIAMACHY on ENVISAT. *J. Atmos. Sci. 62*, 721–734. doi:10.1175/JAS-3328.1

Vountas, M., Rozanov, V. V., & Burrows, J. P. (1998). Ring effect: Impact of rotational Raman scattering on radiative transfer in earth's atmosphere. *Journal of Quantitative*

Spectroscopy and Radiative Transfer, *60*(6), 943–961. doi:10.1016/S0022-4073(97)00186-6

Walter, H. H., Landgraf, J., Spada, F., & Doicu, A. (2006). Linearization of a radiative transfer model in spherical geometry. *Journal of Geophysical Research*, *111*(D24), D24304. doi:10.1029/2005JD007014

Wargan, K., Orbe, C., Pawson, S., Ziemke, J. R., Oman, L. D., Olsen, M. A., Coy, L., & Knowland, K. E. (2018). Recent decline in extratropical lower stratospheric ozone attributed to circulation changes. *Geophysical Research Letters*. doi:10.1029/2018GL077406

Wargan, K., Pawson, S., Olsen, M. A., Witte, J. C., Douglass, A. R., Ziemke, J. R., Strahan, S. E., & Nielsen, J. E. (2015). The global structure of upper troposphere-lower stratosphere ozone in GEOS-5: A multiyear assimilation of EOS Aura data. *Journal of Geophysical Research: Atmospheres*, *120*(5), 2013–2036. doi:10.1002/2014JD022493

Waters, J. W., Froidevaux, L., Harwood, R. S., Jarnot, R. F., Pickett, H. M., Read, W. G., Siegel, P. H., Cofield, R. E., Filipiak, M. J., Flower, D. A., Holden, J. R., Lau, G. K., Livesey, N. J., Manney, G. L., Pumphrey, H. C., Santee, M. L., Wu, D. L., Cuddy, D. T., Lay, R. R., Loo, M. S., Perun, V. S., Schwartz, M. J., Stek, P. C., Thurstans, R. P., Boyles, M. A., Chandra, K. M., Chavez, M. C., Chen, G. S., Chudasama, B. V., Dodge, R., Fuller, R. A., Girard, M. A., Jiang, J. H., Jiang, Y., Knosp, B. W., Labelle, R. C., Lam, J. C., Lee, K. A., Miller, D., Oswald, J. E., Patel, N. C., Pukala, D. M., Quintero, O., Scaff, D. M., Van Snyder, W., Tope, M. C., Wagner, P. A., & Walch, M. J. (2006). The Earth Observing System Microwave Limb Sounder (EOS MLS) on the aura satellite. *IEEE Transactions on Geoscience and Remote Sensing*, *44*(5), 1075–1092. doi:10.1109/TGRS.2006.873771

Weber, M., Coldewey-Egbers, M., Fioletov, V. E., Frith, S. M., Wild, J. D., Burrows, J. P., Long, C. S., & Loyola, D. (2018). Total ozone trends from 1979 to 2016 derived from five merged observational datasets – the emergence into ozone recovery. *Atmospheric Chemistry and Physics*, *18*(3), 2097–2117. doi:10.5194/acp-18-2097-2018

Wiensz, J., Degenstein, D., Lloyd, N., & Bourassa, A. (2013). Retrieval of subvisual cirrus cloud optical thickness from limb-scatter measurements. *Atmospheric Measurement Techniques*, *6*(1), 105–119.

Wiscombe, W. J. (1980). Improved Mie scattering algorithms. *Applied optics*, *19*(9), 1505–9.

WMO (World Meteorological Organization). (2014). *Scientific Assessment of Ozone Depletion: 2014, World Meteorological Organization, Global Ozone Research and Monitoring Project-Report No. 55*. Geneva, Switzerland.

Zawada, D. J., Dueck, S. R., Rieger, L. A., Bourassa, A. E., Lloyd, N. D., & Degenstein, D. A. (2015). High-resolution and Monte Carlo additions to the SASKTRAN radiative transfer model. *Atmos. Meas. Tech. 8*(6), 2609–2623. doi:10.5194/amt-8-2609-2015

Zawada, D., Bourassa, A., & Degenstein, D. (2017). Two-Dimensional Analytic Weighting Functions For Limb Scattering. *Journal of Quantitative Spectroscopy and Radiative Transfer*, *200*, 125–136. doi:10.1016/j.jqsrt.2017.06.008

Ziemke, J. R., Chandra, S., Duncan, B. N., Froidevaux, L., Bhartia, P. K., Levelt, P. F., & Waters, J. W. (2006). Tropospheric ozone determined from Aura OMI and MLS: Evaluation of measurements and comparison with the Global Modeling Initiative's Chemical Transport Model. *Journal of Geophysical Research Atmospheres*, *111*(19), D19303. doi:10.1029/2006JD007089